INTERFACE ENGINEERING IN SOLID-STATE DYE-SENSITIZED SOLAR CELLS

THÈSE N^O 2793 (2003)

PRÉSENTÉE À LA FACULTÉ SCIENCES DE BASE

Institut de chimie moléculaire et biologique

SECTION DE CHMIE ET GÉNIE CHIMIQUE

ÉCOLE POLYTECHNIQUE FÉDÉRALE DE LAUSANNE

POUR L'OBTENTION DU GRADE DE DOCTEUR ÈS SCIENCES

PAR

Jessica KRÜGER

Dipl.-Chem., Universität Heidelberg, Allemagne
et de nationalité allemande

acceptée sur proposition du jury:

Prof. M. Grätzel, directeur de thèse
Dr A. Grisel, rapporteur
Dr H. Spreitzer, rapporteur
Prof. H. Vogel, rapporteur

Lausanne, EPFL
2003

The impossible exists only until we find a way to make it possible.

Mike Horn

ACKNOWLEDGEMENTS

The present study was established in the Laboratory of Photonic and Interfaces (Department of Chemistry) at the École Polytechnique Fédérale de Lausanne (EPFL) under the direction of Prof. Michael Grätzel.

First of all I gratefully acknowledge Prof. Michael Grätzel for having given me the opportunity to perform a PhD thesis in his working group. I appreciate in particular the autonomy of decision I was provided with during my work, including the free choice of international cooperation's. In this context I also like to emphasise the advantageous working conditions at the EPFL: the technical equipment and the advanced training possibilities in various domains were outstanding.

I would like to thank all the members of the "Grätzel group" and the chemistry department who have contributed to my work. These are in particular:

• Robin Humphrey-Baker for sharing with me some of his tremendous knowledge on programming, spectroscopy, and hidden valleys and who helped me with the evaluation of my experimental results.

• Pascal Comte for providing me with different TiO_2 colloids and important information about nanocrystalline TiO_2 films.

• Jacques Moser for the introducing me into the field of laser spectroscopy and for assisting me, and my diploma students using the laser equipment.

• Le Cevey for her help to reach the milestone of 2.5 % efficiency.

• Pierre Infelta for his assistance in informatics and impedance spectroscopy

• The members of the mechanical and electronic workshop, as well as the glassblower Alfred Neuenschwander for manufacturing all the pieces and parts I needed during my thesis. Special thanks to Robert Simon who realised the Kelvin Probe setup.

• My office mates Robert Plass and Nadège Cordente for the wonderful working atmosphere and all the valuable scientific and non scientific discussions.

• Our secretary team with its financial head Nelly Gourdou for their administrative and personal support.

Many thanks also to the ex-members of the Grätzel group, especially the "german speakers" Udo Bach, Roland Hengerer, Frank Lenzmann, and Oliver Kohle as well as Josy Giordano and Carine Viornery. In particular I am grateful to

• Udo Bach who introduced me into the life at the EPFL and the science of the Grätzel cell and who was always available for fruitful discussions.

ABSTRACT

Dye-sensitised nanocrystalline solar cells are currently subject of intense research in the framework of renewable energies as a low-cost photovoltaic device. In particular dye-sensitised cells based on spiro-MeOTAD have gained attention as promising approach towards an organic solid-state solar cell. However, the efficiency in such dye-sensitised solid-state solar devices (SSD) was so far only ca. 10 % of the values reported at AM1.5 for the classical dye-sensitised solar cell with an electrolyte hole transporting medium (DSSC). The objective of the present work is to study the limitations that emerge from the exchange of the electrolyte by the solid-state system and that oppose photovoltaic photon-to-electron conversion as high as for the DSSC.

Interfacial charge recombination is an important loss mechanism in dye-sensitised solar cells. This is particularly true for SSD, as the solid hole-transporting medium is less efficient in screening of internal fields which assist recombination. A variety of strategies were tested in the SSD to minimise interfacial charge recombination. The most promising approach was the blending of the hole-transporting medium with tert.-butylpyridine (tBP) and lithium ions. Optical and electrochemical techniques, such as nanosecond laser spectroscopy, impedance spectroscopy and photovoltaic characterisation measurements, were used to study the impact of the additives on the SSD. Both lithium ions as well as tBP were found to increase the open circuit potential of the SSD. At the same time tBP was found to considerably lower the current output. The interaction of the additives was studied and their concentration in the spiro-MeOTAD medium optimised. The doping of the spiro-MeOTAD film, which was intended to support the hole transport, was found to enhance interfacial recombination significantly.

The morphological properties of the TiO_2, in particular layer thickness, particle size and film porosity, play a more important role in the SSD than in the DSSC. Penetration of the hole conductor into the TiO_2 pores and electron diffusion length are coupled to these properties. As a result the light harvesting cannot be controlled at will via the TiO_2 film thickness and the active surface area for dye adsorption. An enhanced light harvesting for thin TiO_2 layers offers advantages for the charge transport and the formation of the interpenetrating network. The dye uptake in presence of silver ions was found to increase the dye loading and to significantly improve the device performance of thin TiO_2 layer devices. The mechanism of this simple dye modification technique was studied by a variety of spectroscopic techniques. From spectroscopic evidence it is inferred that the silver is

binding to the sensitiser via the ambidentate thiocyanate, allowing the formation of ligand-bridged dye complexes. The beneficial influence of the silver ions on the photovoltaic performance was not limited to the application of the standard N3 dye nor to the spiro-MeOTAD.

SSDs were furthermore studied by frequency resolved techniques. Intensity modulated photocurrent spectroscopy (IMPS) and intensity modulated photovoltage spectroscopy (IMVS) were performed over a wide range of illumination intensities. The IMPS and IMVS responses provide information about charge transport and electron-hole recombination processes respectively. For the range of light intensities investigated, the dynamic photocurrent response appears to be limited by the transport of electrons in the nanocrystalline TiO_2 film rather than by the transport of holes in the spiro-MeOTAD. The diffusion length of electrons in the TiO_2 was found to be 4.4 μm. This value was almost independent of the light intensity as a consequence of the fact that the electron diffusion coefficient and the rate constant for electron-hole recombination both increase in the same way with light intensity but with opposite sign.

The results of this work provide for a substantial improvement of the overall photovoltaic performance compared to earlier results for this type of SSD. However, this study reveals also that high conversion efficiencies as are measured for DSSC are not likely to be reachable with the spiro-MeOTAD system due to the significantly slower charge transport in the spiro-MeOTAD compared to the electrolyte redox mediator.

ZUSAMMENFASSUNG

Farbstoffsensibilisierte nanokristalline Solarzellen werden derzeit als kostengünstige Variante für die photovoltaische Energiegewinnung diskutiert. Vor allem Solarzellen basierend auf dem organischen Lochleiter spiro-MeOTAD erscheinen viel versprechend im Zusammenhang mit der Entwicklung einer organischen Festkörpersolarzelle (solid-state solar Device: SSD). Bisher betrug die Effizienz solcher farbstoffsensibilisierter Zellen nur etwa 10 % der Effizienz der klassischen elektrochemischen Zelle, in der der Lochtransport über ein Elektrolytmedium erfolgt (dye-sensitised solar cell: DSSC). Ziel der vorliegenden Arbeit ist die Untersuchung von Einschränkungen, die sich bei dem Ersatz des Elektrolyten durch ein Feststoffsystem ergeben und die eine effiziente Umwandlung von Photonen in Elektronen verhindern.

Die Ladungsträger-Rekombination an der Grenzfläche zwischen dem farbstoffsensibilisierenden TiO_2 und dem spiro-MeOTAD führt zu einer Verringerung der Effizienz von farbstoffsensibilisierten Solarzellen. Dies gilt insbesondere für die SSD, da der Feststoff-Lochleiter nicht in der Lage ist, elektrische Felder auszugleichen, die die Ladungsträger-Rekombination fördern. Für die Zurückdrängung der Ladungsträger-Rekombination am Interface in der SSD wurden verschiedene Methoden getestet. Der aussichtsreichste Ansatz war das Einbringen von tert.-butylpyridine (tBP) und Lithium-Ionen in das Lochleitermaterial. Der Einfluss der Additive auf die SSD wurde mit optischen und elektrochemischen Analysemethoden untersucht, zum Beispiel Nanosekunden-Laser-Spektroskopie, elektrische Impedance-Spektroskopie und photovoltaische Charakterisationsmethoden. Sowohl Lithium-Ionen als auch tBP erhöhen die Leerlaufspannung der Zelle. Der Kurzschlussstrom wird von den beiden Additiven in gegensätzlicher Weise beeinflusst; Lithium Ionen erhöhen den Kurzschlussstrom, während tBP diesen deutlich verringert. Die Wechselwirkung der Additive wurde untersucht und deren Konzentration in dem spiro-MeOTAD-Medium optimiert. Die Dotierung des spiro-MeOTAD, zur Verbesserung des Lochtransport verursacht eine starke Zunahme der Ladungsträger-Rekombination am Interface.

Die morphologischen Eigenschaften des TiO_2, insbesondere die Filmdicke, die Partikelgröße und die Filmporosität sind von größerer Bedeutung in der SSD als in der DSSC. Das Eindringen des Lochleiters in das TiO_2-Netzwerk und die potenzielle Diffusionslänge der Elektronen hängen direkt von diesen Eigenschaften ab. Daraus ergibt sich, dass die Größe der Lichtabsorption nicht beliebig durch die Schichtdicke des TiO_2

vergrößert werden kann. Eine größere Lichtabsorption für dünne Schichten bietet daher Vorteile für den Ladungstransport und das Eindringen des Lochleiters in das TiO_2-Netzwerk. Es konnte gezeigt werden, dass die Absorption des Standard N3-Farbstoffes auf dem TiO_2 in Gegenwart von Silber-Ionen zu einer erhöhten Farbstoffdichte führt und damit die Effizienz der Zelle signifikant verbessert wird. Der Mechanismus dieser einfachen Modifikationstechnik wurde mit einer Vielzahl spektroskopischer Analysemethoden untersucht. Die experimentellen Ergebnisse zeigen, dass über den Thiocyanat-Ligand die Silber-Ionen an die metallorganische Farbstoffmoleküle gebunden werden. Dies erlaubt die Ausbildung von Brücken zwischen Farbstoffmolekülen. Die Ausbildung einer Monoschicht dicht gepackter Farbstoffmoleküle erhöht die Lichtabsorption der Zelle und verringert gleichzeitig die Ladungsträger-Rekombination am Interface. Der positive Einfluss dieser Farbstoffmodifikation konnte auch für andere Thiocyanat-Liganden enthaltene Sensibilisatoren als den N3-Farbstoff und für andere Lochleitersysteme beobachtet werden.

Die SSD wurden weiterhin mit optischer Impedancespektroskopie untersucht. So wurde die intensitätsmodulierte Photostrom-Spektroskopie (IMPS) und die intensitätsmodulierte Photospannungs-Spektroskopie (IMVS) über einen großen Bereich verschiedener Lichtintensitäten angewendet. IMPS und IMVS liefern Informationen über Ladungstransport und Elektronen-Loch-Rekombinationsprozesse. Für die untersuchten Lichtintensitäten scheint der Photostromtransport durch den Elektronentransport im TiO_2 und nicht durch den Lochtransport im spiro-MeOTAD limitiert zu sein. Eine potenzielle Diffusionslänge von 4.4 μm für Elektronen im TiO_2 wurde bestimmt, die nahezu unabhängig von der Lichtintensität ist. Die fehlende Abhängigkeit von der Lichtintensität ergibt sich aus der Tatsache, dass der Elekronendiffusionskoeffizient und die Elektronenlebensdauer in gleichem Maße mit der Lichtintensität variieren, jedoch mit unterschiedlichem Vorzeichen.

Die Ergebnisse dieser Arbeit ermöglichen eine deutliche Verbesserung der Zelleffizienz gegenüber früheren, für diesen Zelltyp gemessenen Werten. Allerdings ergibt sich aus dieser Studie auch, dass hohe Umwandlungseffizienten, wie sie für die DSSC gemessen wurden, für die SSD in Zukunft nicht wahrscheinlich sind.

RÉSUMÉ

Les cellules solaires sensibilisées par des colorants sont considérées de nos jours comme une variante économique pour la conversion photovoltaïque. En particulier, les cellules à colorants basées sur le spiro-MeOTAD semblent prometteuses dans le développement de cellules solaires solides organiques (solid-state solar device : SSD). Pourtant les efficacités rapportées jusqu'à maintenant, atteignent uniquement 10% des rendements des cellules classiques à colorant basées sur électrolyte liquide (DSSC). L'objectif de ce présent travail est d'étudier les limitations engendrées par échange de l'électrolyte par un système solide, et qui empêchent une conversion efficace de photons en electrons aussi éléve que l'on trouve dans des cellules classiques.

La recombinaison interfaciale de charge est un mécanisme de perte important dans les cellules solaires sensibilisées par colorant. Ceci est particulièrement vrai dans le cas des SSD, le milieu solide transporteur de trous étant moins efficace dans la diminution de champs interne qui sont propice à la recombinaison de transporteurs de charges. Une variété de stratégies fut testée dans la SSD afin de minimiser la recombinaison interfaciale de charge. L'introduction dans le matériau transporteur de trous de tert.-butylpyridine (tBP) et de ions lithium semble être l'approche la plus prometteuse. Des techniques optiques et électrochimiques, comme la spectroscopie laser nanoseconde, la spectroscopie d'impédance et les mesures de caractérisation photovoltaïques, furent utilisées pour étudier l'impact de ces additifs sur la SSD. Il fut trouvé que les ions de lithium ainsi que la tBP augmentent le potentiel de circuit ouvert de la SSD. En même temps, il fut montré que la tBP diminue le courant à la sortie. Les interactions des additifs furent étudiées et leur concentration optimisée dans le spiro-MeOTAD. Le dopage du spiro-MeOTAD, supposé améliorer le transport de trous, provoque une augmentation considérable de la recombinaison interfaciale de charge.

Les propriétés morphologiques du TiO_2, en particulier l'épaisseur de la couche, la taille des particules, et la porosité des films, jouent un rôle plus important dans le cas de la SSD que dans celui de la DSSC. La pénétration du conducteur trou dans les pores du TiO_2 et la longueur de diffusion des électrons sont reliées à ces propriétés. De ceci résulte que l'absorption de lumière ne peut pas être contrôlé uniquement par l'épaisseur de la couche de TiO_2 et l'aire de la surface active pour l'absorption de colorant. Une plus grande collection de lumière pour des couches minces de TiO_2 offre des avantages pour le transport de charges et une meilleure pénétration du conducteur trou dans le réseau de

TiO$_2$. L'absorption de colorant N3 sur le TiO$_2$ a pu être améliorée par l'introduction d'ions d'argent, l'efficacité de la cellule a pu ainsi être significativement augmentée. Les mécanismes de cette simple technique de modification du colorant furent étudiés par une variété de techniques spectroscopiques. Les résultats expérimentaux montrèrent que les ions d'argent se lient à la molécule organométallique du colorant par le ligand thiocyanate. Ceci permet la formation de ponts entre les molécules de colorant. L'influence bénéfique des ions d'argent sur les performances photovoltaïques, ne fut pas limitée à l'application au colorant standard N3 ni au conducteur trou spiro-MeOTAD.

Les SSD furent également étudiées à l'aide de spectroscopie d'impédance. La spectroscopie du photocourant par modulation de l'intensité lumineuse (IMPS) ainsi que la spectroscopie du photovoltage par modulation de l'intensité lumineuse (IMVS) furent appliquées sur une large plage d'intensité d'illumination. Les mesures IMPS et IMVS apportèrent beaucoup d'informations concernant, respectivement, le transport de charge et la recombinaison électron trou. Pour la plage d'intensités de lumière utilisée, les réponses dynamiques de photocourant semblent être limités par le transport d'électrons au sein du TiO$_2$ nanocristallin, plutôt que par le transport de trous dans le spiro-MeOTAD. Une distance de diffusion de 4.4μm fut trouvée pour les électrons dans le TiO$_2$. Cette valeur fut presque indépendante de l'intensité lumineuse, du fait que le coefficient de diffusion des électrons et la constante de vitesse pour la recombinaison électron trou varient tous deux de la même manière avec l'intensité mais avec des signes opposés.

Les résultats de ce travail apportent une amélioration substantielle aux performances photovoltaïques par rapport aux résultats obtenus précédemment sur ce type de SSD. Cependant, cette étude a montré qu'il n'était pas possible d'atteindre des efficacités de conversions aussi élevées que dans le cas des DSSC avec le système spiro-MeOTAD, cela étant dû au transport de charge nettement plus lent dans le spiro-MeOTAD comparé à l'électrolyte avec médiateur redox.

Table of Contents

LIST OF ABBREVATIONS

Physical Constants

c	$[2.998 \cdot 10^8 \ \text{m}\,\text{s}^{-1}]$	speed of light
e	$[1.602 \cdot 10^{-19} \ \text{C}]$	elementary charge
F	$[9.64 \cdot 10^4 \ \text{C} \cdot \text{mol}^{-1}]$	Faraday constant
h	$[6.626 \cdot 10^{-34} \ \text{Js}]$	Planck constant
k_B	$[1.3181 \cdot 10^{-23} \ \text{J} \cdot \text{K}^{-1}]$	Boltzmann constant

Physical Variables

a	$[\text{m}^2]$	surface area
A	[-]	optical absorbance
c	$[\text{mol} \cdot \text{l}^{-1}]$	concentration
C_{SC}	[F]	capacitance of space charge layer
C_{CT}	[F]	charge transfer capacitance
C_{HC}	[F]	hole conductor trap state capacitance
CPD	[mV]	contact potential difference
C_{ss}	[F]	capacitance of surface trap states
d	$[\mu\text{m}]$	layer thickness
D_{eff}	$[\text{cm}^2 \cdot \text{s}^{-1}]$	diffusion coefficient
f	[Hz]	frequency
FF	[%]	fill factor
E_g	[eV]	band gap energy
E_c	[eV]	conduction band energy
E_f	[eV]	Fermi level
E_v	[eV]	valence band energy
IPCE	[%]	incident monochromatic photon-to-current conversion efficiency
I_{sc}	[mA]	short circuit current
J_{sc}	$[\text{mA}\cdot\text{cm}^{-2}]$	short circuit current density
k	$[\text{s}^{-1}]$	rate constant
k_{ext}	$[\text{s}^{-1}]$	potential dependent rate constant
L_n	$[\mu\text{m}]$	diffusion length
n	$[\text{cm}^{-3}]$	electron density
Q	[C]	charge
R_{CT}	$[\Omega]$	charge transfer resistance

R_{HT}	$[\Omega]$	charge transport resistance
U_{oc}	$[V]$	open circuit voltage
α	$[cm^{-1}]$	absorption coefficient
χ	$[eV]$	electron affinity
ε	$[l \cdot mmol^{-1} \cdot cm^{-1}]$	molar absorption coefficient
ϕ	$[V]$	electrochemical potential
η	$[\%]$	efficiency
τ	$[s]$	lifetime
ω	$[s^{-1}]$	$\omega = 2 \cdot \pi \cdot f$, radial frequency
μ	$[m^2 \cdot V \cdot s^{-1}]$	mobility
κ	$[S \cdot m^{-1}]$	conductivity
λ	$[nm]$	wavelength

Abbreviations

AM	air mass
bpy	bipyridine
dmbip	2,6-bis(1-methylbenzimidazol-2-yl)pyridine
dcbpy	2,2'-bipyridyl-4,4'-dicarboxylic acid
CVD	chemical vapour deposition
dopant	tris(p-bromophenyl)ammoniumyl hexachloroantimoate $[N(p-C_6H_4Br)][SbCl_6]$
ET	electron transfer
DABCO	1,4-Diazabicyclo[2.2.2]octane
DBU	1,8-Diazabicyclo[5.4.0]undec-7-ene
DMPII	1,2-dimethyl-3-propylimidazoliumiodid
ECN	Energy Research Centre of the Netherlands
DSSC	dye-sensitized solar cell, in the actual context: classical Grätzel electrolyte cell
HC	spiro-MeOTAD: 2,2`,7,7`-tetrakis-(N,N-di-p-methoxyphenylamin) 9,9`-spirobifluoren
HOMO	highest occupied molecular orbital
IMPS	intensity modulated photocurrent spectroscopy
IMVS	intensity modulated photovoltage spectroscopy
ITO	indium tin oxide
LiTFSA	Lithium bis-trifluorosulfonimid, $Li(CF_3SO_2)_2N$
LED	light emitting diode
OLED	organic light emitting diode
LH	Light harvesting
LHE	Light harvesting efficiency
LMCT	ligand-to-metall charge transfer
LUMO	lowest unoccupied molecular orbital
MLCT	metall-to-ligand charge transfer

4,4`-Me$_2$bpy	4,4`-dimethyl-2,2`-bipyridine
NREL	National Renewable Energy Laboratories (USA)
NSG	Nippon sheet glass
OPO	optical parametric oscillator
PAS	Photoaccoustic spectroscopy
proton sponge	N,N,N¢,N¢-Tetramethyl-1,8-naphthalenediamine
4`-paterH$_2$	2,2`:6`.2"-terpyridine-4`-phophonic acid
4`-ppaterH$_2$	2,2`:6`.2"-terpyridine-4`-phenylphophonic acid
rpm	rounds per minute
SPRE	Surface plasmon resonance effect
SERRS	Surface enhanced resonance Raman spectroscopy
SERS	Surface enhanced Raman scattering
SSD	solid-state solar cell, in contrast to DSSC
TAA	Titanium(IV)bis(acetylacetonato)diisopropoxide
TBA	Tetrabutylammonium, Bu$_4$N
TCO	transparent conducting oxid
tcterpy	4,4',4''-tricarboxy-2,2',6,2''-terpyridine
terpy	2,2',6,2''-terpyridine
tBP	4-tert.-butylpyridine
TPD	N,N`-Bis(3-methylphenyl)-N,N`-diphenylbenzidin
UHV	ultra-high vacuum
UV	ultra-violett

Dye Names

MC2	3-acetyl-5-12-(3-ethyl-2-benzothiazolydene)rhodanine (KF 599)
N3	[Ru(dcbpyH$_2$)$_2$(NCS)$_2$], "red dye"
N719	(Bu$_4$N)$_2$[Ru(dcbpyH)$_2$(NCS)$_2$]
N712	(Bu$_4$N)$_4$[Ru(dcbpy)$_2$(NCS)$_2$]
N749	TBA$_2$[Ru(H$_2$tcterpy)(NCS)$_3$], "Black Dye", also: N749.2 to represent the protonation degree

1 INTRODUCTION

The emergence of an electric potential between two electrodes attached to a solid or liquid system upon light irradiation has been discovered by Bequerel in 1839[1] and is ever since known as photovoltaic effect. This discovery has been the base for a variety of concepts to convert solar radiation into electricity and has opened a new domain of alternative energy generation.

Today the photovoltaic market is dominated by silicon in its multicrystalline and monocrystalline form. Further silicon research is concentrated on thin-film crystalline silicon (about 5–30 μm active layer thickness), which avoids the costly crystal growing and sawing processes. The problems arising for this material are: assuring adequate light absorption, assuring good crystal quality and purity of the films, and finding a substrate that fulfils all requirements. Genuine thin-film materials are characterised by a direct band structure, which gives them very high light absorption. Therefore, these materials have a thickness of only 1 μm or less. Other inorganic materials used for photovoltaic devices belong to the group of chalcogenides such as copper indium diselenide (CIS) and cadmium telluride. The interest has expanded from $CuInSe_2$ to $CuGaSe_2$, $CuInS_2$ and their multinary alloys $Cu(In,Ga)(S,Se)_2$. The two deposition techniques are either separate deposition of the components followed by annealing or co-evaporation. Laboratory efficiencies for small area devices are approaching 19 % and large area modules have reached 12 %. Cadmium telluride solar cells which show only slightly lower efficiency also offer great promise.

From a solid-state physics point of view silicon is not an ideal material for photovoltaic conversion for two reasons: There is a small spectral mismatch between absorption and the semiconductor and the sunlight spectrum, approximated by a black body of 5900 K. A much more serious point is that silicon is an indirect semiconductor, meaning that valence band maximum and conduction band minimum are not opposite to each other in k-space. Light absorption is much weaker in an indirect gap semiconductor than in a direct semiconductor. This has serious consequences from a materials point of view: for a 90 % light absorption it takes only 1 μm of GaAs (a direct semiconductor) versus 100 μm of Si. The photogenerated carriers have to reach the pn-junction which is near the front surface. The diffusion length of minority carriers has to be 200 μm or at least twice the silicon thickness. Thus, the material has to be of very high purity and of high crystalline perfection. In view of these physical

limitations a lot of effort has been invested into the search for new materials. Consequently requirements for the ideal solar cell material are a band gap between 1.1 and 1.7 eV and a direct band structure. Furthermore the material should be readily available, non-toxic and processible with easy, reproducible deposition techniques, that are suitable for large area production. Alternatively to the search of new inorganic semiconductor materials other device geometries have been developed for the purpose of light to electron conversion, such as various concentrating systems including III/V-tandem cells.

In the last years the search for new materials has been more and more extended into the field of organic molecules and polymers, which offer several advantages compared to inorganic materials. Organic materials are chemically tunable to adjust physical properties such as band gap, valance and conduction energies, charge transport, solubility, morphological properties. In general, their processing is fairly easy and is established using wet-processing techniques (spin coating, cast coating, ink-jet printing, roll-to-roll processing) as well as dry processing (thermal evaporation). Due to the small quantities needed for device preparation and the easy large scale production and purification, organic materials have furthermore an economic advantage compared to inorganic material. Organic photovoltaic solar cells therefore bear an important potential of development in the search for low-cost modules for the production of domestic electricity.

Organic charge transport material have either molecular or polymer structure. While charge transport in molecular systems occurs intermolecularly from molecule to molecule, polymer charge transport proceeds intramolecularly, along the polymer chain. The conductivity for molecular systems is $<10^{-8}$S/cm, for polymers similar or higher. Both technologies show some advantages and comparable device performances. To date it is not clear which technology will succeed or if both will co-exist.

Molecular and polymer organic materials found application in solar cells of different geometrical structure:[2,3] In the single layer or Schottky junction cell the light absorption semiconductor is forming a rectifying junction with one electrode, which allows the charge separation.[4] Absorption covering the entire visible range is rare using a single species of molecules. Since positive and negative photoexcited charges travel through the same material, recombination losses are high for this cell structure. In contrast double layer cells offer separate charge transport layers and therefore less recombination.[5] Light absorption and the generation of electron-hole pairs (excitons) is limited to a small interface layer. Only excitons of a thin layer, corresponding to the sum of exciton diffusion length and depletion layer thickness, become dissociated. The interface between two materials is drastically increased in the interpenetrated network of layer blend systems. A special type of layer blend device is the dye-sensitised solar cell. Classical dye-sensitised solar cells are

heterojunction devices between an inorganic large band gap semiconductor and an electrolyte rather than organic solar cells. The classification into the group of organic solar cells is due to an organic dye molecule adsorbed onto the semiconductor surface, sensitizing the semiconductor for visible light absorption. Several derivatives of this type of device, employing inorganic sensitisers, such as inorganic quantum dots are subject of recent research.

The drawback for the application in photovoltaic devices is that the mobility in organic semiconductors are usually rather small: from 10^{-2} in well ordered conjugated polymers down to 10^{-8} cm^2/sV in guest polymer systems, and for molecular systems even lower. A mobility distribution for a given material causes usually a dispersive charge transport. Mobilities are highly dependent on the electric field and the molecular packing quality, which is determined by molecular ordering. Correspondingly a drastic reduction of mobility will be caused by imperfect purification and uncontrolled crystallisation[6] as well as oxygen traps.[7] Another problem, in particular for earlier organic photovoltaic devices, is the degradation of the organic material, which might have manifold causes. Electrochemical reactions, caused by ionic impurities and/or water which may promote redox reactions at an electrode, for example, can be addressed by employing highly purified materials and encapsulation of the device. Degradation due to structural reorganisation processes, such as re-crystallisation of glasses on heating of the sample were controlled by engineering sterically demanding molecule structures. Photochemical side reactions in a charge transport material, however, are more difficult to control.

Although organic solar cells, can still not compete with conventional photovoltaic cells in terms of commercial application, the prospective to develop a long-term technology based on environmentally safer materials with almost unlimited availability justifies intensive research in this domain.

1.1 Dye-Sensitised Solar Cell (DSSC)

Apart from the economic interest to develop a low-cost alternative to the conventional solar cell, dye-sensitised solar cells have become an interdisciplinary scientific "playground". Sensitisation of wide band gap semiconductors using dyes has a long history, dating back to early days of photography of the 19th century: Moser observed that the photoelectric effect on silver plates was enhanced in the presence of erythrosine dye.[8] Systematic mechanistic studies started only in the late 1960's with the work of dye-sensitisation process on ZnO[9-11] and SnO$_2$[12-14] electrodes carried out by Gerischer and Memming. Most of these early studies were fundamental in nature, aimed to understand electron–transfer processes involving

valence and conduction bands of a semiconductor immersed in a redox electrolyte. Gerischer combined the stability of large band gap semiconductors with the photosensitivity to light in the visible domain by dye adsorption onto semiconductor surface. The breakthrough of dye-sensitised devices as solar cell was based on the exchange of the bulk semiconductor by mesoporous structures of high surface area, which allowed a drastic enhancement of the amount of adsorbed dye. Furthermore the development of stable metal organic sensitisers bearing attachment groups which allow the chemical bonding of the sensitiser to the surface of the TiO_2 lead to a drastic improvement in charge injection efficiency. Based on these innovations overall efficiencies of over 10 % were obtained for dye-sensitised mesoporous TiO_2 electrodes in contact with an electrolyte containing an iodide based redox system for dye regeneration.[15]

Figure 1.1 shows the processes taking place during the conversion of light into electrons in a dye-sensitised solar cell. Upon excitation the dye injects electrons into the conduction band of the titanium oxide with the rate K_{inj}. The photoinduced electrons diffuse through the porous TiO_2 network and are extracted at the SnO_2 substrate. The dye itself is regenerated by the electrolyte containing the redox pair I^-/I_3^- The electronic circuit is closed by the reduction of the iodide couple at the platinised SnO_2 counter electrode.
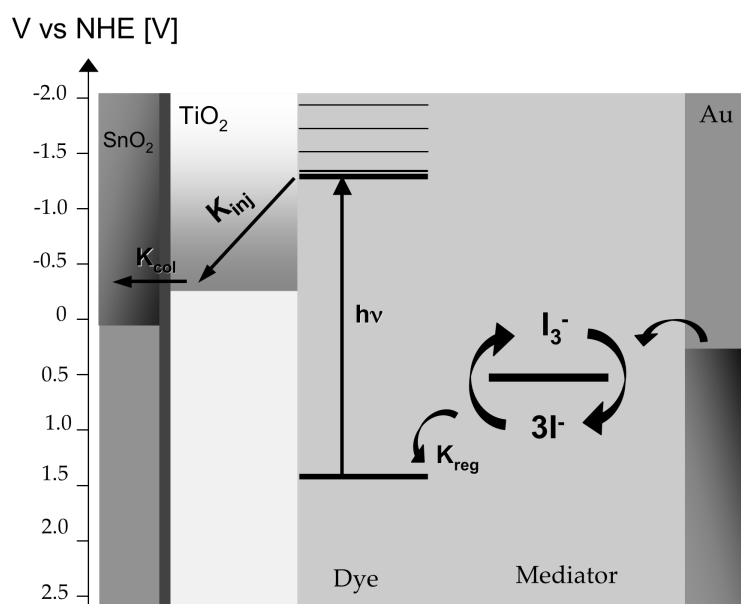
Figure 1.1: Scheme presenting the electron processes taking place in a illuminated dye-sensitised solar cell under open circuit conditions. HC stands for hole conductor.

The dye-sensitised light-to-electron conversion process differs fundamentally from the one in the **conventional** solar cells. Figure 1.2 shows the energy band diagram of a pn-junction after thermal equilibration of charge carriers. The uncompensated charge caused

by the diffusion of holes to the n region, and electrons to the p region, forms an electric field at the interface between the n and the p type semiconductor (space charge layer), which is characterised by the built in potential V_{bi}. Absorption of photons with an energy higher than the band gap results in the generation of excitons which interact via columbic forces. Exitons recombine after a certain time under emission of photons or heat, unless they are separated by an electric field. Therefore only exitons created in the space charge layer or close to it will contribute to the photocurrent.
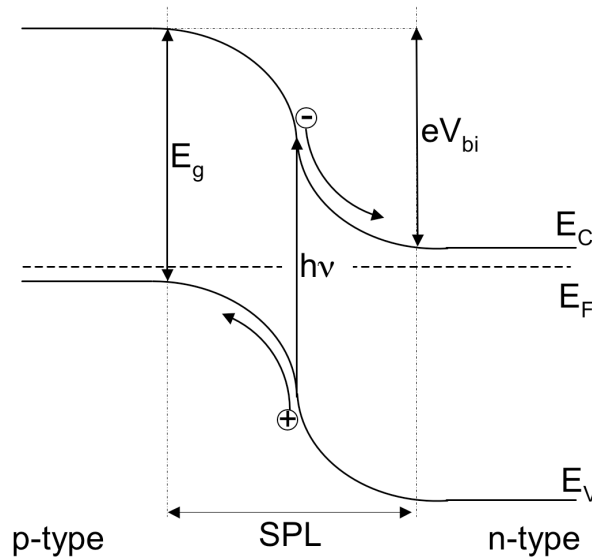
Figure 1.2: Energy band diagram of a conventional pn junction solar cell under short circuit conditions.

Comparison of Figure 1.1 and Figure 1.2 demonstrates the difference between dye-sensitised solar cells and conventional solar cells:

1. Light adsorption and charge carrier transport are separated in dye-sensitised solar cell, whereas both processes are established by the semiconductor in the conventional cell.

2. An electric field is necessary for charge separation in the pn junction cell. Nanoparticles in the dye-sensitised solar cell are too small to sustain a build-in field; accordingly charge transport occurs mainly via diffusion.

3. Inside a pn junction minority and majority charge carriers coexist in the same bulk volume. This makes conventional solar cells sensitive to bulk recombination and demands the absence of any recombination centres such as trace impurities. Dye-sensitised solar cells are majority charge carrier devices in which the electron transport occurs in the TiO_2 and the hole transport in the electrolyte. Recombination processes can therefore only occur in form of surface recombination at the interface.

Important drawbacks of the dye-sensitised solar cell are the volatility of the electrolyte and the corrosive action of the iodide redox couple. Correspondingly, long-term application of dye-sensitised solar cell is limited by the electrolyte permeability of the encapsulation and its inertness towards the iodine. A lot of effort has therefore invested in finding less volatile electrolytes while maintaining sufficient hole transport. Approaches to replace the liquid electrolyte include application of ionic conducting polymer gels,[16-18] electrolyte gellated with amino-acid derivatives[19] or room temperature molten salts.[20] Complete replacement of the liquid electrolyte system has been established using inorganic p-type semiconductors, such as CuI[21-24] or CuSCN[25,26] as well as organic hole conductors, including low molecular weight charge transport materials[27] and semiconducting polymers.[28,29]

1.2 Solid-State Dye-Sensitised Solar Cell (SSD)

The replacement of the liquid charge transporting medium with a solid one has important consequences for the electronic processes in the cell. A new cell design is required in which the device geometry is adapted to the solid system. This task has been addressed in a previous Ph.D. thesis.[30] This work showed that the organic charge transport material 2,2'7,7'-tetrakis(N,N-di-p-methoxyphenyl-amine)-9,9'-spirobifluorene (spiro-MeOTAD) can be used to replace the liquid iodine/iodide electrolyte in photoelectrochemical cells. Maximum white light conversion efficiencies of up to 1.8 % for 1/10 Sun (AM1.5;10 mW/cm^2) were obtained with this type of dye-sensitised heterojunction. Interfacial charge recombination processes have been identified as the main loss mechanism in this type of cell. For a further development of the SSD based on spiro-MeOTAD it is essential to find strategies to suppress interface charge recombination and to identify the differences in charge transport compared to the high efficiency electrolyte solar cell. A better understanding of the electronic processes in the SSD and the optimisation of the inorganic/organic interpenetrating network promises further improvement of the device performance.

The key problem related to the replacement of the liquid by solid charge transport material is the less efficient hole transport in the solid medium as a result of the relatively low hole mobilities in organic semiconductors. Low conductivities imply high resistance causing voltage losses, particularly for high current densities. Slow charge transport is expected to generate concentration gradients in the hole conductor matrix. As a consequence an accumulation of holes might build up inside the pores, accompanied by a depletion of holes in the bulk organic semiconductor. This concentration gradient of holes

will lead to a charging of the interface which will considerably increase the interfacial recombination.

Interface charging is favoured by imperfect penetration of the hole conductor into the colloidal film. In the case of the electrolyte cell the penetration is complete and a semiconductor/electrolyte junction occurs at each nanocrystal. This intimate contact and the high mobility of electroactive species guarantee efficient screening of any electric field emerging from electron injection. Assuming that the kinetics of charge transfer to the electrolyte is much faster for the holes than the recombination processes, the electrons can create a gradient in the electrochemical potential between the particle and the back contact. In this gradient, the electrons can be transported through the interconnected colloidal particles to the back contact (percolation), where they are withdrawn as a current. It has been established that electron transport in nanocrystalline TiO$_2$ films is dominated by electron trapping in intraband-gap defect states.[31-34] In a strongly screened environment such as in the electrolyte cell the multiple trapping takes place mainly via thermal activation of trapped electrons.[35,36] As a result of the less efficient screening of photoinduced electric fields in the SSD the electron transport in the TiO$_2$ may significantly differ from the one in DSSC leading to immobilisation of trapped electrons on the time scale of the experiment.

Assuming that TiO$_2$ network and hole conductor film can be treated as bulk material with respect to conductivity a decrease of layer thickness should improve the charge transport. In particularly regarding the TiO$_2$, thin layer thicknesses guarantee efficient collection also for low electron diffusion length, which is a direct measure for the charge recombination. However, thin TiO$_2$ layers imply less active surface area for dye adsorption and hence lower light harvesting. It is therefore necessary to find a way to increase the optical density of the dye-sensitised film which allows preparing devices with thinner TiO$_2$ layers. The search for stable dyes with high extinction coefficients and large absorption spectra covering most of the visible spectrum has accompanied the development of the DSSC for the last ten years. So far no dye has been found which combine these three requirements and which could seriously compete with the standard ruthenium complex. The search for strategies to enhance light-harvesting continues to be a challenging task not only in terms of the SSD.

Another aspect of importance in the context of organic charge transport material is the device stability, which is crucial particularly in view of a commercial application. The stability of SSD based on spiro-MeOTAD, was only little addressed so far. Upon storage of the device under ambient conditions the short circuit current was reported to decrease, while the open-circuit voltage and fill-factor increased with time. As these effects were found to compensate each other no change in overall efficiency was observed.[30] The observed changes in I$_{SC}$ and U$_{OC}$ indicate that side reactions are taking place which need to be

identified and if possible to be prevented. Sealing the cells towards oxygen and moisture might be a remedy in terms of degradation processes.

1.3 Objective of the Present Work

The solid solid-state dye-sensitised solar cell based on spiro-MeOTAD was originally designed to avoid electrolyte-specific problems, such as evaporation of the electrolyte and corrosion by the volatile redox mediator. However, up to date the SSD cannot compete with the DSSC in terms of performance. The objective of the present work is thus to perform a systematic study of the performance limiting factors emerging from the solid-state concept and to provide remedies to address these limitations and information about the improvement potential of the SSD. The study is mainly of experimental nature, supported by different spectroscopic and electrochemical techniques.

The present work is subdivided into four main parts: The first part (chapter 2 and 3) discusses theoretical and practical issues of experimental techniques and device preparation. Chapter 4 addresses the interfacial recombination in solid-state dye-sensitised solar cell and the approach of its inhibition by chemical modification of the heterojunction between the TiO_2 and spiro-MeOTAD. Chapter 5 focuses on a new strategy to gain in light harvesting by complexation of standard ruthenium dye molecules via silver ions. The last part (chapter 7) presents electrochemical and optical impedance studies. In particular the application of intensity modulated photocurrent and photovoltage spectroscopy, which have not been used in the context with the solid-state dye-sensitised solar cells so far, were expected to yield information about charge transport mechanism in the TiO_2 in contact with the spiro-MeOTAD.

1.4 References

[1] E. Becquerel. *C R* **1839**, *9*, 561.

[2] J. Simon and J.-J. André. Molecular Semiconductors: Photoelectrical Properties and Solar Cells Springer, 1985.

[3] D. Woehrle and D. Meissner. *Adv Mater* **1991**, *3*, 129.

[4] D. L. Morel, A. K. Kosh, T.Feng, et al. *Appl Phys Lett* **1978**, *32*, 495.

[5] C. W. Tang. *Appl Phys Lett* **1986**, *48*, 183-185.

[6] J. H. Schön, S. Berg, C. Kloc, et al. *Science* **2000**, *287*.

[7] J. H. Schön, C. Kloc, R. C. Haddon, et al. *Science* **2000**, *288*.

[8] J. Moser. *Monatsh Chem* **1887**, *8*, 373.

[9] H. Gerischer and H. Tributsch. *Berich Buns Gesell* **1968**, *72*, 437-&.

[10] H. Gerischer, H. R. Schoppel and B. Pettinge. *J Electrochem Soc* **1972**, *119*, C230-&.

[11] H. Tributsch and H. Gerischer. *Berich Buns Gesell* **1969**, *73*, 251-&.

[12] R. Memming. *Faraday Discuss* **1974**, 261-270.

[13] R. Memming and F. Schroppel. *Chem Phys Lett* **1979**, *62*, 207-210.

[14] R. Memming, F. Schroppel and U. Bringmann. *J Electroanal Chem* **1979**, *100*, 307-318.

[15] B. O'Regan and M. Grätzel. *Nature* **1991**, *353*, 737-739.

[16] F. Cao, G. Oskam and P. Searson. *J Phys Chem* **1995**, *99*, 17071.

[17] A. F. Nogueira, M. A. De Paoli, I. Montanari, et al. *J Phys Chem B* **2001**, *105*, 7517-7524.

[18] W. A. Gazotti, A. F. Nogueira, E. M. Girotto, et al. *Synth Met* **2000**, *108*, 151-157.

[19] W. Kubo, K. Muakoshi, T. Kitamura, et al. *Chem Lett* **1998**, 1241.

[20] N. Papageorgiou, Y. Athanassov, M. Armand, et al. *J Electrochem Soc* **1996**, *143*, 3099-3108.

[21] K. Tennakone, G. Kumara, I. Kottegoda, et al. *J Phys D-Appl Phys* **1998**, *31*, 1492-1496.

[22] K. Tennakone, G. R. R. A. Kumara, A. R. Kumarasinghe, et al. *Semicond Sci Technol* **1995**, *10*, 1689-1693.

[23] K. Tennakone, A. R. Kumarasinghe and P. M. Sirimanne. *Semicond Sci Technol* **1993**, *Vol 8, Iss 8*, 1557-1560.

[24] K. Tennakone, G. R. R. A. Kumara, K. G. U. Wijayantha, et al. *Semicond Sci Technol* **1998**, *13*, 134-138.

[25] B. O'Regan and D. T. S. D.T. *J Appl Phys* **1996**, *80*, 4749.

[26] B. O'Regan and D. Schwartz. *Chem Mater* **1998**, *10*, 1501-1509.

[27] J. Hagen, W. Schaffrath, P. Otschik, et al. *Synth Met* **1997**, *89*, 215-220.

[28] K. Murakoshi, G. Kano, Y. Wada, et al. *J Electronanal Chem* **1995**, *396*, 27.

[29] K. Murakoshi, R. Kogure and S. Yanagida. *Chem Lett* **1997**, *5*, 471-472.

[30] U. Bach. Ph.D. Thesis, EPFL, 2000.

[31] K. Schwarzburg and F. Willig. *Appl Phys Lett* **1991**, *58*, 2520-2523.

[32] R. Könenkamp, R. Henninger and P. Hoyer. *J Phys Chem* **1993**, *97*, 7328-7330.

[33] F. Cao, G. Oskam, G. J. Meyer, et al. *J Phys Chem* **1996**, *100*, 17021-17027.

[34] P. E. d. Jongh and D. Vanmaekelbergh. *Phys Rev Lett* **1996**, *77*, 3427.

[35] J. Nelson. *Phys Rev B* **1999**, *59*, 15374-15380.

[36] J. Nelson, S. A. Haque, D. R. Klug, et al. *Phys Rev B* **2001**, *6320*, 205321.

2 SOLID STATE DYE SENSITISED SOLAR CELL

This chapter discusses the structure of the solid-state dye-sensitised solar cell (SSD) and its key components, the photoelectrode, the sensitiser, the dye regeneration material, and the counter electrode, in more detail. The materials requirements for each component are emphasised, showing the multidisciplinary approach of this type of solar cell. Finally the kinetics of the electron transfer processes in the SSD are reviewed.

2.1 Structure of the SSD

In contrast to the sandwich design of the electrolyte solar cell between two TCOs, solid-state dye-sensitised devices (SSD) posses typically a monolithic structure. Each layer is deposited on top of the other and contacts are positioned on the same substrate. In the following the key components of the SSD will be addressed.

2.1.1   <u>Photoelectrode</u>

The dye-sensitised oxide is typically deposited on a highly doped, transparent conducting oxide (TCO), which allows light transmission while providing sufficient conductivity for current collection. Recently organic polymers of high conductivity deposited onto plastic foil find increasing application as substrate for flexible devices. Metal foils show conductivities superior to the TCOs and polymers. Because of their opacity the illumination of the cell has to be established through the counter electrode.

The surface of TCO should make a good mechanical and electrical contact with the porous TiO_2 film. From dark current measurements of TiO_2/spiro-MeOTAD it is known that the hole conductor is forming an ohmic contact with the back contact layer (SnO_2:F). To reduce dark current losses due to short circuit of electrons in the substrate with holes in the hole conductor a thin underlayer of TiO_2 is introduced between the SnO_2 layer and nanocrystalline TiO_2 layer. This thin compact layer does furthermore improve the

mechanical adhesion of the porous TiO_2 film on the substrates, especially for SnO_2 layers of low haze, i.e. less surface roughness and thus less contact area.

The TiO_2 semiconductor has three functions in the dye-sensitised solar cell: it provides the surface for the dye adsorption, it functions as electron acceptor for the excited dye and it serves as electron conductor. Colloid preparation and layer deposition have been developed to optimise the TiO_2 for these functions. Most important for the performance of dye-sensitised solar cells was the development of a mesoporous semiconductor structure. This becomes evident considering the limited light capture of a dye monolayer on a flat surface. For an extinction coefficient (ε) around $1\text{-}4*10^5\,M^{-1}\,cm^{-1}$ the cross section for light absorption, given by

$$\sigma = \varepsilon \cdot 1000 \cdot \frac{\ln(10)}{N_A} \qquad (2.1)$$

is between 0.0038 and 0.15 nm^2. This is smaller than the area occupied by the sensitiser (1-2 nm^2), i.e. only a few percent of the incoming light can be absorbed. On the other hand deposition of multilayers of dye on the surface in order to increase its light absorption is not of advantage, since outer dye layers act only as light filter, with no contribution to injection. In contrast mesoporous structures based on particles of 10-20 nm provide surface areas 1000 times larger than the apparent geometric one, depending on film thickness and porosity. The enhanced light absorption leads to a drastically improved light harvesting efficiency (LHE):

$$LHE = 1 - 10^{-A} = 1 - 10^{-\Gamma*\sigma} \qquad (2.2)$$

with Γ=dye coverage [cm^{-2}] and σ=absorption cross section [cm^2] (scattering by the film is neglected).

Untreated TiO_2 is an isolator which becomes "photo doped" and therefore conductive by electron injection of the adsorbed dye. Electronic contact between the nanoparticles is established by sintering the nanoparticles together, enabling the entire surface-adsorbed molecular layer to be accessed electronically. The interconnection of the nanoparticles by the sintering process allows the deposition of a mechanically stable, transparent film of typically a few micron thickness. Increase of the free electron concentration in the dark is not necessary and may even be detrimental for the photoelectrochemical behaviour of the TiO_2.

Amongst several semiconductors studied for photoelectrochemical applications, TiO_2 is by far the most commonly used, because of its energetic properties, its stability, and the Lewis acidity of the surface, which allows attachment of dyes. It is furthermore a low cost material which is widely available. TiO_2 is used in its low-temperature stable form anatase (pyramide-like crystals), as rutile shows non-negligible absorption in the near-UV region

(350–400 nm). This excitation within the band gap leads to generation of holes, which are strong oxidants and cause long-term instability issues in the solar cell.

2.1.2   <u>Sensitiser</u>

The dye is the photoactive element of the photovoltaic device, harvesting the incident light for the photon-to-electron conversion. To be used as sensitiser for a single junction photovoltaic cell the dye must fulfil the following requirements:

Photochemical Properties

The dye should ideally cover a wide range of the solar spectrum. More than 50 % of the solar energy is emitted in the region from 400 to 800 nm. Thus ruthenium dyes that adsorb throughout the visible spectrum (panchromatic) capture most of the sunlight. However, the further the absorption edge is at longer wavelength the lower is the photovoltage. Thus a shift of the dye spectrum to longer wavelength will not yield higher energy conversion efficiencies as the loss in photovoltage is not fully compensated by the gain in photocurrent.

The extinction coefficient of the dye should be high throughout the entire absorption spectrum, in order to absorb most of the light with a minimum quantity of dye material. Since the white light harvesting efficiency is limited by the absorption in the weaker absorbing regions, a high extinction coefficient at wavelengths different from the maximum absorption peak is particularly important.

The excited state life time of the dye must be long enough for efficient electron injection. In general this requirement is not a limiting factor, as electron injection occurs on the subnanosecond time scale and thus can compete efficiently with other excited state decay processes.

Electrochemical Properties

For efficient electron injection the oxidation potential of the dye excited state $\phi^0(S^+/S^*)$ needs to be more negative than the conduction band potential of the SC ($\phi_{fb}=\phi_{cb}$ for nano-size particles).

$$\phi^0(S^+/S) < \phi_{cb} + \frac{\Delta E_{0,0}}{F} \qquad\qquad (2.3)$$

where $\Delta E_{0,0}$ is the excitation energy of the dye, ϕ_{cb} the conduction band edge of the semiconductor and F the faraday constant. On the other hand the oxidation potential of the dye oxidised state $\phi^0(S^+/S)$ has to be more positive than the oxidation potential of the regeneration system.

$$\phi^0(S^+/S) < \phi(D^+/D) \tag{2.4}$$

Recently it has been shown that the excess of vibrational energy of the dye acquired during the excitation could be used in the electron injection process.[1-3] Therefore, dyes with lower (S^+/S^*) energy than the conduction band, but excited with photons that bring them in a vibronic level that lies above the conduction band edge are also able to inject in the semiconductor.

Chemical Properties

For efficient electron injection the dye needs to be bound to the TiO_2 surface via physi- or chemisorption. Groups such as carboxylate, phosphonate or sulfonate are commonly used for the surface attachment onto oxide semiconductors. Therefore standard dyes bear attachment groups which enable chemisorption of the dye on the TiO_2 surface. With decreasing distance of the dye to the surface the electron injection rate increases. The rate can be further accelerated when the π-system of the dye in the excited state can be delocalised into the semiconductor.

So far dye adsorption from solution is the most convenient method for the dye uptake. The ideal dye solution is based on an inert solvent which allows reasonable amounts of dye to be dissolved and which does not or only in negligible amounts adsorb on the TiO_2 surface.

Stability

The dye must possess long-term stability for reproducible device characterisation as well as for future commercial applications which requires cell lifetimes of 20 years with 10^8 redox turnovers under illumination. Despite intensive research in the field of sensitiser engineering so far no dye has been reported that may replace the ruthenium complex *cis*-[Ru^{II}(dcpby)$_2$(NCS)$_2$] as standard dye for the application in dye-sensitised solar cells. This is mainly due to the enhanced stability of the ruthenium complex compared to other sensitisers.

A vast variety of different sensitisers systems, that fulfill these requirements more or less, were studied for the application in the DCCS. In the context of artificial photosynthesis natural dyes such as chlorophyll[4] and different porphyrins[5] were used. Organic dyes with high extinction coefficient such as Cyanines and Xanthenes are known from their application in photographic films for the sensitisation of AgCl crystals and were also used as sensitisers in photoelectrochemical devices to create photocurrent. The photochemical properties of merocyanine dyes and their application in the dye-sensitised solar cell has been intensively studied by Nüesch.[6,7] Inorganic particles of nanometer scale (quantum dots) have been

recently used in photo electrochemical cell as well as in SSD.[8] This type of sensitiser offers the advantage of choosing the region of adsorption by tuning the size of the nano particle sensitiser.

The "N3 Dye"

The highest efficiencies for dye-sensitised solar cells were reported for devices based on $(Bu_4N)_2[Ru(dcbpyH)_2(NCS)_2]$.[9] This dye was also mainly used in this work and was obtained by reaction of the fully protonated form, the N3 dye, with 0.5 dye mole equivalents of t-butylammonium hydroxide. The N3 is attached to the TiO_2 via two of the four carboxyl groups situated trans to the NCS ligand.[10] The dye adsorption onto TiO_2 follows the Langmuir theory with a binding constant of $K = 5 \cdot 10^4 M^{-1}$.[11] The area occupied by one molecule at the anatase surface at full monolayer coverage is 1.65 nm^2.

2.1.3   Hole Conductor

The hole conductor regenerates the oxidised dye after electron injection into the semiconductor, and transports the positive charge to the counter electrode. To function as dye mediator in the SSD the following requirements have to be fulfilled.

Electrochemical Properties

To enable reduction of the oxidised dye, the redox potential of the mediator must be more negative than that of the oxidised dye:

$$\phi(D^+/D) < \phi^0(S^+/S) \tag{2.5}$$

Since the maximum photovoltage obtainable is related to the position of the mediator redox potential, $\phi(D^+/D)$ should be as positive as possible. On the other hand the difference of the two potentials should be high enough to provide a driving force for the dye reduction and therefore an optimal regeneration rate. It is obvious that the redox-couple must be reversible at the counter electrode, while being inert to the TiO_2. Moreover the redox mediator, in particular its oxidised form, must not quench the excited state of the dye, so that the reaction has to be significantly slower than the electron transfer of the dye to the TiO_2.

Photochemical Properties

The mediator should not have any significant light absorption in the visible range, to avoid internal filter effects. This property is particulary important when illuminating the device through the counter electrode, or when using reflecting counter electrodes.

Morphological Properties

The hole conductor must be processable, without destruction of the dye adsorbed on the TiO$_2$. Typical deposition techniques for organic semiconductors are thermal evaporation, electrochemical deposition, and different coating techniques, such as spin-coating, dip-coating or tape-casting. For the formation of stable amorphous films, materials with relatively high glass melting temperatures are needed. Regarding the filling of the TiO$_2$ pores with the organic semiconductor, low molecular weight molecules are preferred to polymers.

Charge Transport Properties

The dye mediator system should be able to transport a current of a few mA/cm^2 without diffusion limitation or significant ohmic losses. This is a very stringent requirement to fulfill for most of the organic semiconductor systems, which typically show a rather low conductivity in the undoped state. The limiting current depends on the thickness dx of the charge-transporting medium, the number of charge carriers dn and the mobility μ, which is a material constant:

$$J_n = \mu \cdot k \cdot T \cdot \frac{dn}{dx} \tag{2.6}$$

As a remedy to this problem, common for organic semiconductors, the conductivity of the organic film can be enhanced by increasing the number of charge carriers through oxidative doping. Speaking in terms of inorganic semiconductor terminology the Fermi-level shifts towards the transport states upon doping. Furthermore the resistive losses can be reduced by adjusting the layer thickness of the hole conductor.

"spiro-MeOTAD"

Spiro-MeOTAD (2,2',7,7'-tetrakis(N,N-di-*p*-methoxyphenyl-amine)-9,9'-spirobifluorene) was designed for the application in organic devices based on the standard hole transport material N,N'-diphenyl-N,N'-bis(3-methylphenyl)-1,1'-biphenyl-4,4'diamine (TPD). The thermal stability of the glassy state could be drastically improved by connecting two TPD units via a spiro centre.[12-14] Due to the increased steric demand of the spiro molecule, solution and crystallisation properties are changed without significant change of the electronic properties of the base molecule. Compared to TPD, spiro-MeOTAD has a 60°C higher glass transition temperature, which enables the formation of stable amorphous films. While films of TPD are more or less crystallised after two months, pure spiro-MeOTAD film will stay in the amorphous state for years. However, the introduction of the spiro center also increases the melting point to 246 °C, which makes it impossible to produce layers of spiro-MeOTAD by thermal evaporation in UHV. The standard deposition technique is therefore

spin-coating of a solution of spiro-MeOTAD in chlorobenzene.

The substitution of TPD with two methoxy substituents leads to a seven times higher hole mobility of the material.[15] TPD molecules containing methoxy substituents show an improved stability of the corresponding radical cation, which has been assigned to increased electronic overlap of the molecular orbitals caused by the electron withdrawing methoxy groups. Spiro-MeOTAD contains 8 methoxy substituents and shows a 0.1 V higher oxidation potential, compared to the unsubstituted structure

The reduced form of the hole conductor is pale yellow and absorbs in the UV (λ_{max}=372 nm). Its four oxidation states can be obtained via chemical oxidation with [N(p-C_6H_4Br)][$SbCl_6$].[16] The spectrum of spiro-MeOTAD$^+$ shows an intense band at 511 nm and a shoulder at 700 nm. The spiro center connects two identical molecule units in a perpendicular arrangement and acts as an electronic barrier. Therefore the spectrum of the spiro-MeOTAD^{2+} is similar to the mono cation but with a doubled extinction coefficient. According to Weissörtel[14] the diradical cation of spiro-MeOTAD shows absorption maxima in $CHCl_3$ at 511 nm (ε=40100 $M^{-1} cm^{-1}$) and 1400 nm (ε=32200 $M^{-1} cm^{-1}$), while spiro-MeOTAD^{4+} exhibits an absorption maxima at 865 nm (ε=118000 $M^{-1} cm^{-1}$).

The mobility of the spin-coated spiro-MeOTAD has been studied by Poplavsky[17] by means of time-of-flight (TOF) measurements, dark-injection space-charge-limited current transients and steady-state current-voltage characteristics. The voltage dependent room temperature mobilities for film thickness ranging 4000 nm to 135 nm were determined to be in the around of $10^{-4} cm^2$/Vs. Contrary to earlier results published by Bach[18] employing smaller molecules of the same structural type as spiro-MeOTAD, the charge transport has been found to be a non-dispersive process. Analysis of the temperature-field behaviour of the time-of-flight mobility based on the Gaussian Disorder Model developed by Bässler et al.[19] revealed higher energetic disorder for the methoxy-substituted compound (spiro-MeOTAD) than for the non-substituted analogue. The comparison of similar molecules with and without spiro center revealed that the spiro-concept leads to high morphologic stability, without deteriorating its electronic properties.[18]

The conductivity of a pure, 1 μm thick film spiro-MeOTAD film is in the range of MΩ/cm^2. The relative low charge mobility has been compensated for by doping of the hole conductor film using Tris(p-bromopheny)ammoniumyl hexachloroantimonate [N(p-C_6H_4Br)$_3$][$SbCl_6$].[20] This oxidative doping of spiro-MeOTAD via a one-electron transfer leads to a dark conductivity increased by many orders of magnitude.

2.1.4   Counter Electrode

The counter electrode has ideally a high conductivity and exhibits an ohmic contact to the hole conductor, which requires workfunction matching of hole conductor and counter electrode. A large built-in potential between the electrode materials corresponding to a large difference in workfunction of the two materials decreases the U_{OC} considerably. Noble metals with high workfunction, such as gold and platinum as well as carbon and conducting polythiophene polymers were found to form an ohmic contact with spiro-MeOTAD.[16] Gold and platinum are typically applied by thermal evaporation in UHV or by sputtering in the case of platinum which is a very controllable technique and therefore reproducible. However, it is vigorous for the organic surface and there is some concern about chemical modification of the organic surface.[16,21] Metal counter electrodes have the advantage of reflecting the light[*] transmitted by the photoelectrode which cause a second traversal of the dye-sensitised film, thus enhancing light absorption for a given amount of dye. Inert metals which do not chemically react with the organic semiconductor are, however, known for their diffusion on the surface and into the interior of the organic even at room temperature.[22-24] This mechanism is highly dependent on the evaporation parameters such as evaporation rate and evaporation temperature.[25] Carbon and in particularly organic polymers have lower conductivities than the metals. Both carbon and conducting polymers are typically applied in form of pastes by screen-printing or tape coating. The definition of small electrode areas is difficult with this wet deposition techniques and the resulting devices are less reproducible. Carbon can also be applied in form of pressed graphite.[26] This technique is very fast and can be easily reversed. It is however complicated to apply in case of subsequent sealing. Gold electrodes were used in present work for the sake of simplicity and reproducibility. Metal films serve moreover as an oxygen barrier and can thus protect the organic material underneath. Better stability of gold electrodes compared to graphite electrodes were also observed in other SSD.[26]

2.2 Electron Transfer Dynamics

Dye-sensitised solar cells are working on the basis of differential kinetics. The presence of a local electrostatic field is not required to achieve good collection efficiencies. This

---

[*] Gold is an excellent reflector for the IR (800 nm-30 μm: 98 %). In the visible region an opaque gold film is still reflecting about 40 % of the incident light. Evaporated platinum films have a reflectance of 60-75 % between 400-800 nm.

distinguishes nanocrystalline devices from conventional photovoltaic cells in that the successful operation of the latter is contingent upon the presence of a potential gradient within the p-n junction.

Figure 2.1 summarises the electron transfer processes occurring at the dye-sensitised heterojunction. Recent studies of the *electron injection* dynamics from the electronically excited state of Ru(II)polypyridyl complexes into the conduction band of the TiO_2 demonstrated that the electron injection is occurring in the ultrafast time regime (fs to ps) and that the dye cation radical is formed with a yield of nearly 100 %.[27-30] Assuming, that the injection kinetics do not significantly change upon replacement of the electrolyte mediator by the solid-state charge transport material,[31] the injection of electrons by the sensitiser in the solid-state solar cell is expected to show similar characteristics as have been determined for the electrolyte cell.

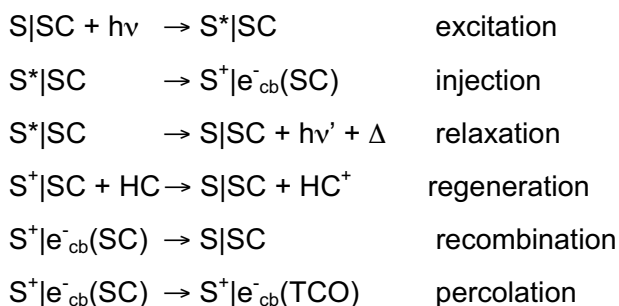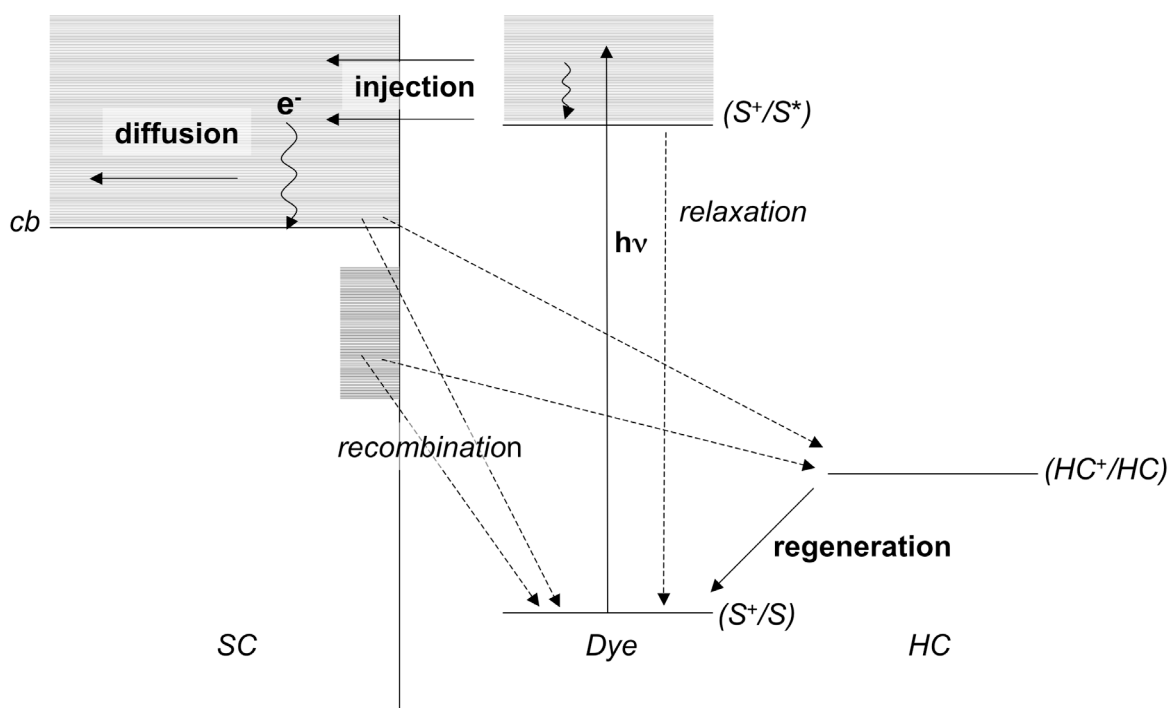|		
S|SC + hν	→ S*|SC	excitation
S*|SC	→ S$^+$|e$^-_{cb}$(SC)	injection
S*|SC	→ S|SC + hν' + Δ	relaxation
S$^+$|SC + HC	→ S|SC + HC$^+$	regeneration
S$^+$|e$^-_{cb}$(SC)	→ S|SC	recombination
S$^+$|e$^-_{cb}$(SC)	→ S$^+$|e$^-_{cb}$(TCO)	percolation

Figure 2.1 Electron transfer processes at the dye-sensitised heterojunction

The rate of electron injection has been shown to depend on a variety of parameters, such as the length of the spacer between electron donor and acceptor,[32] the density of acceptor states,[33] and the electronic coupling between the dye and the semiconductor.[34] Moser et al. have shown that the exciting wavelength has an influence on the quantum yield of the electron injection, implying that electron injection can take place from hot vibrational states.[2,3,35] The competition between relaxation of the dye excited state and the injection reaction is contra dictionary to Kasha's rule.[36] The electron movement in the nanocrystalline TiO_2 to the back contact (*percolation*) is significantly slower than in the TiO_2 single crystal. This has been demonstrated by photocurrent transient measurements after UV illumination of TiO_2 particles, which showed decay times of milliseconds to seconds.[37]

Back reaction of electrons in the TiO_2 with the oxidised ruthenium complex is extremely slow, occurring typically in the microsecond time domain. This slow *recombination* rate has been assigned to the weak overlap of the d-Orbital localised on the Ru metal and the TiO_2 conduction band, which are involved in this recombination process. Other recombination pathways are more important for the function of the cell and will be discussed in more detail in chapter 5.

The dynamics of the *interception* of the oxidised dye by the hole conductor have been found to proceed with a broad range of time constants from 3 ps $< \tau <$ 1 ns.[38] Multiple phases of injection process were assigned to the heterogeneous nature of the heterojunction, incomplete pore filling and the thereby resulting lateral hole migration between neighbouring dye molecules[39,40] not in contact with the regeneration material. The hole injection quantum yield has been calculated to be 50 % after 900 ps. At longer times, around 10 ns, the efficiency of hole transfer approaches unity.

2.3 References

[1] F. Lenzmann, J. Krüger, S. Burnside, et al. *J Phys Chem B* **2001**, *105*, 6347-6352.

[2] J. E. Moser and M. Grätzel. *Chimia* **1998**, *52*, 160-162.

[3] J. E. Moser, M. Wolf, F. Lenzmann, et al. *Z Phys Chem* **1999**, *212*, 85-92.

[4] A. Kay, R. anHumphry-Baker and M. Grätzel. *J Phys Chem* **1994**, *98*, 952-959.

[5] A. Kay and M. Grätzel. *J Phys Chem* **1993**, *97*, 6272.

[6] F. Nüesch, J. E. Moser, V. Shklover, et al. *J Am Chem Soc* **1996**, *118,* 5420-5431.

[7] F. Nüesch and M. Grätzel. *Chem Phys* **1995**, *193*, 1-17.

[8] R. Plass, S. Pelet, J. Krueger, et al. *J Phys Chem B* **2002**.

[9] M. K. Nazeeruddin, R. Humphry-Baker, P. Liska, et al. *submitted for publication* **2003**.

[10] K. S. Finnie, J. R. Bartlett and J. L. Woolfrey. *Langmuir* **1998**, *14*, 2744-2749.

[11] A. Hagfeldt and M. Graetzel. *Acc Chem Res* **2000**, *33*, 269-277.

[12] J. Salbeck, F. Weissörtel and J. Bauer. *Macromol Symp* **1997**, *125*, 121-132.

[13] J. Salbeck, N. Yu, J. Bauer, et al. *Synth Met* **1997**, *91*, 209-215.

[14] F. Weissörtel. Ph. D. Thesis, 1996.

[15] J. S. Facci, M. Abkowitz, W. Limburg, et al. *J Phys Chem* **1991**, *95*, 7908-7914.

[16] U. Bach. Ph.D. Thesis, EPFL, 2000.

[17] D. Poplavskyy and J. Nelson. *J Appl Phys* **2003**, *93*, 341-346.

[18] U. Bach, K. de Cloedt and M. Grätzel. *Adv Mat* **2000**, *12*, 1060-1063.

[19] H. Bässler. *Phys Stat Sol B* **1993**, *175*, 15.

[20] M. Abkowitz and D. M. Pai. *Phil Mag B* **1986**, *53*, 193.

[21] A. Ioannidis, J. S. Facci and M. Abkowitz. *J Appl Phys* **1998**, *84*, 1439-1444.

[22] M. Probst and R. Haight. *Appl Phys Lett* **1997**, *70*, 1420-1422.

[23] R. Willecke and F. Faupel. *J Polym Sci Part B* **1997**, *35*, 1043-1048.

[24] R. Willecke and F. Faupel. *Macromol* **1997**, *30*, 567-573.

[25] A. C. Dürr, F. Schreiber, M. Kelsch, et al. *Adv Mater* **2002**, *14*, 961-963.

[26] B. O'Regan, F. Lenzmann, R. Muis, et al. *Chem Mater* **2002**, *14*, 5023-5029.

[27] Y. Tachibana, J. E. Moser, M. Grätzel, et al. *J Phys Chem* **1996**, *100*, 20056-20062.

[28] R. Eichberger and F. Willig. *Chem Phys* **1990**, *141*, 159.

[29] J. Kallioinen, V. Lehtovuori, P. Myllyperkiö, et al. *Chem Phys Lett* **2001**, *340*, 217-221.

[30] C. Bauer, G. Boschloo, E. Mukhtar, et al. *J Phys Chem B* **2001**, *105*, 5585-5588.

[31] J. R. Durrant, Y. Tachibana, I. Mercer, et al. *Z Phys Chemie-Int J Res Phys Chem Chem Phys* **1999**, *212*, 93-98.

[32] J. B. Asbury, E. Hao, Y. Wang, et al. *J Phys Chem B* **2000**, *104*, 11957-11964.

[33] B. Langdon, V. MacKenzie, D. Asunskis, et al. *J Phys Chem B* **1999**, *103*.

[34] K. Kalyanasundaram and M. Grätzel. *Coord Chem Rev* **1998**, *77*, 347–414.

[35] J. E. Moser, D. Noukakis, U. Bach, et al. *J Phys Chem B* **1998**, *102*, 3649-3650.

[36] M. Kasha. *Compl Mol* **1950**, 14-19.

[37] A. Hagfeldt and M. Grätzel. *Chem Rev* **1995**, *95*, 49-68.

[38] U. Bach, Y. Tachibana, J.-E. Moser, et al. *J Am Chem Soc* **1999**, *121*, 7445-7446.

[39] P. Bonhôte, E. Gogniat, S. Tingry, et al. *J Phys Chem B* **1998**, *102*, 1498-1507.

[40] T. A. Heimer, S. T. D'Arcangelis, F. Farzad, et al. *J Inorg Chem* **1996**, 5319-532.

3 EXPERIMENTAL METHODS

This chapter focuses on the individual measurement techniques, and their relevant theoretical background. The characterisation of the performance of the solid-state solar cells (SSD) was established employing photovoltaic techniques, including white light current-voltage characteristics and the determination of the incident-light-to-current conversions efficiency (IPCE). These DC characterisation techniques were accomplished by optical and electrical impedance spectroscopy as well as laser transient spectroscopy. The individual components of the SDD were studied by means of different spectroscopic techniques, such as UV/VIS and FTIR- spectroscopy, X-ray photoelectron spectroscopy and the Kelvin-Probe technique.

3.1 Photovoltaic Device Characterisation

The standard characterisation techniques of solar cells include the determination of the DC current-voltage characteristic under white light illumination of different intensities and the determination of the photocurrent under low intensity monochromatic light.

Current-voltage characteristics of solar cells are described based on the Shottky equation for thermionic emission:

$$I(V) = I_{Ph} - I_0 \cdot \exp\left[\frac{q \cdot (V + I \cdot R_S)}{n \cdot k \cdot T} - 1\right] - \frac{V + I \cdot R_S}{R_P} \tag{3.1}$$

where R_S is the series resistance, R_p the shunt resistance, n the ideality factor, I_0 the saturation current of the diode, and I_{ph} the photo current. The Shottky equation models the dark current in a one-diode system and offers only a simplified representation of the present system. The real structure of the device is much more complicated corresponding to multi-diode model that take into account different charge transport processes in the cell. However, already the simple Shottky approach yields reasonable good fits for most of the devices and is useful for general discussion of the shape of the IV curves.

Analysis of the photocurrent-voltage curves includes the determination of the following parameters:

Short-circuit current (I_{SC}): Cell current measured at an applied potential of zero volt. I_{SC} is a function of the illumination intensity.

Open-circuit potential (U_{OC}): Cell potential measured when current in the cell is zero, corresponding to almost flat valence and conduction bands. U_{OC} is obtained from Equation 1.1 by setting the current to zero:

$$V_{OC} = \frac{n \cdot k \cdot T}{q} \ln\left(\frac{I_{Ph}}{I_0} + 1 - \frac{V_{OC}}{I_0 \cdot R_p}\right) \approx \frac{n \cdot k \cdot T}{q} \ln\left(\frac{I_{Ph}}{I_0} + 1\right) \tag{3.2}$$

Maximal power output (P_{max}): For a given bias voltage the power output of the cell is the product of the measured cell current and the voltage $P(V) = I \cdot U$. Imax and Umax are the coordinates of the maximum in the $P(V)$ curve (maximum power point). The maximum power corresponds visually to the area of the largest rectangle, which can fit inside the current voltage curve (Figure 3.2).

The fill factor (FF) is the ratio of the maximum power to the external short and open circuit values:

$$FF = \frac{I_{max} \cdot U_{max}}{I_{SC} \cdot U_{OC}} \tag{3.3}$$

This parameter indicates the deflection of the current-voltage characteristic from a square like curve and is therefore dependent on series and shunt resistance. Figure 3.1 illustrates the influence of increasing series resistance R_s and decreasing shunt resistance R_p on the current-voltage characteristic. To obtain high fill factors R_s has to be as small as possible, while R_p needs to be as high as possible.
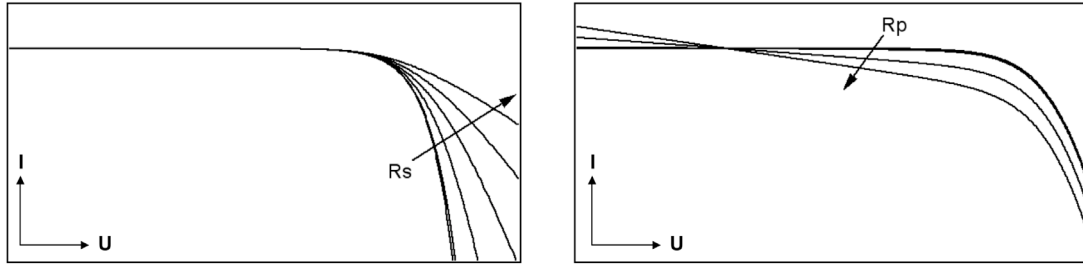
Figure 3.1: Illustration of the influence of increasing series resistance R_s and decreasing shunt resistance R_p on the current-voltage characteristic of a solar cell (I=current, U=potential).

The **Efficiency (η)** describes the performance of the solar cell and is defined as the ratio of the maximum electric power extracted to the radiation power incident on the solar cell surface:

$$\eta = \frac{P_{max}}{P_{in}} = \frac{I_{SC} \cdot U_{OC} \cdot FF}{P_{in}} \tag{3.4}$$

The efficiency is a function of the U_{OC}, the I_{SC} and the FF of the cell. Accordingly, improvement of the photovoltaic yield is the result of the optimisation of these three parameters.
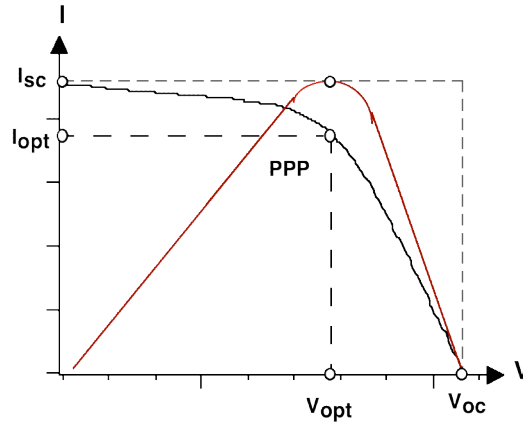
Figure 3.2: Scheme explaining maximal power output

To compare solar cell characterised in different laboratories all over the world, photovoltaic cells are measured under a set of standard test condition. Essentially, these specify that the temperature of the cell should be 25°C and that the solar radiation incident on the cell should have a total power density of 1000 W/m^2, with a spectral power distribution characterised as AM1.5. The Air mass (AM) is the ratio of the path length of the suns rays through the atmosphere when the sun is at a given angle θ to the zenith, to the path length when the sun is at its zenith (Figure 3.3). This relation can be approximated by:

$$AM \approx \frac{1}{\cos\theta}$$
(3.5)

An Air Mass distribution of 1.5, as specified in the standard test conditions, corresponds to the spectral power distribution observed when the suns radiation is coming from and angle to overhead of about 48°.
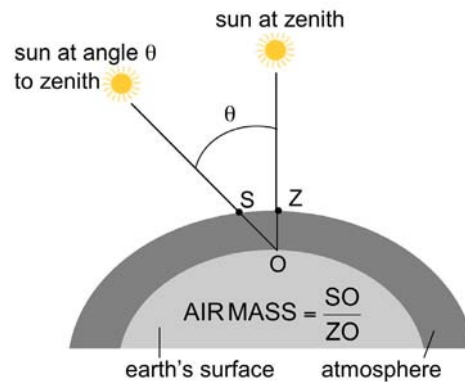
Figure 3.3: Illustration of the "air mass" concept.

The determination of the photocurrent under monochromatic illumination is established to derive the **Incident-photon-to-electron conversion efficiency (IPCE)**, which is defined by the ratio of the number of electrons generated in the solar cell to the number of photons incident *on* the photoactive surface of the device at a given wavelength.

$$IPCE(\lambda) = \frac{n_{electrons}(\lambda)}{n_{photons}(\lambda)} = \frac{I(\lambda) \cdot h \cdot c}{P_{in}(\lambda) \cdot e \cdot \lambda} \approx \frac{1239 \cdot I(\lambda)}{P_{in}(\lambda) \cdot \lambda},$$ (3.6)

where $I(\lambda)$ corresponds to the measured current in $\mu A/cm^2$, $P(\lambda)$ is the input optical power in W/m^2 and λ the wavelength of the incident irradiation in nm. In general the IPCE is measured under short-circuit conditions and is graphically displayed versus the corresponding wavelength in a photovoltaic action spectra. The IPCE corresponds to the photo response or external quantum efficiency. Correcting the IPCE for the number of photons, which are not adsorbed by the test cell leads to the internal quantum efficiency or:

Absorbed-photon-to-electron conversion efficiency (APCE), which is defined by the ratio of the number of electron-hole pairs generated in the solar cell to the number of photons absorbed by the photoactive surface of the device at a given wavelength. The APCE is calculated dividing the IPCE by the light harvesting of the test device:

$$APCE(\lambda) = \frac{IPCE}{1-T}$$ (3.7)

In general the spectra of artificial light sources differ from the spectrum of the sunlight. Measurements under simulated white light conditions have therefore to be corrected for this spectral mismatch, using the following **mismatch factor:**[1]

$$M = \frac{M_{RC}}{M_{TC}} = \frac{\int E_{AM1.5}(\lambda) \cdot S^{RC}(\lambda) \cdot d\lambda}{\int E_{sim}(\lambda) \cdot S^{RC}(\lambda) \cdot d\lambda} \cdot \frac{\int E_{sim}(\lambda) \cdot S^{TC}(\lambda) \cdot d\lambda}{\int E_{AM1.5}(\lambda) \cdot S^{TC}(\lambda) \cdot d\lambda}$$ (3.8)

with: $E_{AM1.5}(\lambda)$= relative spectral irradiation intensities at AM1.5

$E_{sim}(\lambda)$= relative spectral irradiation intensities under simulated sunlight

$S^{RC}(\lambda)$= relative spectral sensitivity of reference cell (calibrated at standard AM 1.5)

$S^{TC}(\lambda)$= relative spectral sensitivity of test cell

For the determination of this mismatch the spectral response curves of a test cell, a reference cell (calibrated at standard AM1.5, 100 mW/cm^2) and the spectral irradiation intensity of the simulated radiant source are determined. Integration over the product of the relative spectral irradiation intensity and the relative spectral sensitivity yields the corresponding short circuit current.

$$I = \int E(\lambda) \cdot S(\lambda) \cdot d\lambda$$ (3.9)

With (1.6) and (1.7) it follows for the short circuit current of the test cell under AM1.5:

$$I_{AM1.5}^{TC} = I_{sim}^{TC} \left(\frac{I_{AM1.5}^{RC}}{I_{sim}^{RC}} \right) \cdot \frac{M_{TC}}{M_{RC}} \qquad (3.10)$$

The correction for the spectral mismatch is then obtained by adjusting the lamp output, so that $I_{sim}^{RC} = I_{AM1.5}^{RC} \cdot M^{-1}$. Under this conditions $I_{sim}^{TC} = I_{AM1.5}^{TC}$ and the I-V curve will not need any corrective interpretation. If for technical reasons a lamp adjustment is not possible, the following fractional error ε has to be considered:

$$\varepsilon = \frac{I_{sim}^{TC} - I_{AM1.5}^{TC}}{I_{AM1.5}^{TC}} = \frac{M \cdot I_{AM1.5}^{TC} - I_{AM1.5}^{TC}}{I_{AM1.5}^{TC}} = M - 1 \qquad (3.11)$$

As the spectral response of dye-sensitised solar cells can be easily tuned by exchange of the sensitiser, the mismatch factor can become an important parameter for the photovoltaic characterisation. The photovoltaic setup used for the present work has been adjusted to match the spectral response of a DSSC sensitised with the N719 dye. Measurements of cells with other dyes have therefore to be corrected for the spectral mismatch Table 3.1 shows the fractional error in $I_{AM1.5}^{TC}$ calculated from the spectral response of SSD sensitised with different dye systems that have been used in the present work.

Dye	ε[%]
N719	1.2
Ag-N719	3.1
N749	-4.5
MC2	3.9

Table 3.1: Fractional error in $I_{AM1.5}^{TC}$ (400-800 nm) for different dye systems used in the present work. For the dye names compare the list of abbreviations.

The difference of SSD sensitised with N719 and DSSC sensitised with N719 can be assigned to the thicker TiO$_2$ layers used in the DSSC, which provoke an increased spectral sensitivity in the infrared.

Experimental Setup

Current-voltage characteristics were measured using a Keithley 2400 Source Meter and a sulfur lamp (solar 1000, Fusionlighting Inc/USA) as light source.[2] Light intensity was changed with meshes in front of the light source and measured with a Si Photodiode (calibrated at the ISE-Fraunhofer Institut in Freiburg, Germany). The spectral response of the silicon reference cell was adapted to the spectral sensitivity of the dye-sensitised solar cell with a Schott© KG3 filter in front of the reference diode. Efficiencies were corrected for the spectral mismatch.

To avoid obscuring of the current-voltage characteristics by charge equilibration processes the **scan rate** was adapted to the system. This was established by measuring the hysteresis between forward and backward scan for different light intensities and the current respectively voltage response to a rectangular light signal of varying length and light intensity. In particular the later experiment shows that the SSD is reacting much more slowly to a light or a potential impulse than the DSSC.

For the IPCE measurements light of a 300 W Xe lamp were spectrally narrowed to a monochromatic light using a motor driven double monochromator (Spex Gemini 180, Jobin Yvon Instruments SA). The spectral response of the test cell as a function of wavelength was determined relative to the spectral response of a calibrated silicon reference cell. No corrections for surface- and interface reflections losses were made for standard characterisations.

3.2 Nanosecond Laser Spectroscopy

Recombination dynamics at the TiO_2/HC interface were studied by means of time-resolved laser absorption spectroscopy. The dye was excited by pulsed laser photolysis at a wavelength where the absorbance of the dye is relatively low to assure a homogeneous absorption profile throughout the dye-sensitised TiO_2 layer. The typical excitation wavelength for experiments based on the N719 dye was 600 nm (OD~0.2). The reaction of the photo injected electron in the TiO_2 with the hole conductor is monitored as change in optical density of the hole conductor absorbance:

$$HC^+ + TiO_2 / e_{inj}^- \xrightarrow{\text{recombination}} HC + TiO_2$$
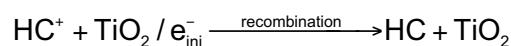
An observation wavelength of 1000 nm was chosen, where the radical cation of the spiro-MeOTAD has a strong absorption maximum. At this wavelength, and in the time regime of interest only the electrons in the TiO_2 contribute to the measuring signal. For the absorption of the electrons in the TiO_2 a decadic extinction coefficient ε=3400 M^{-1} cm^{-1} has been determined by Rothenberger.[3] This is small compared to the extinction coefficient of the hole conductor around 1000 nm (21700 M^{-1} cm^{-1}) so that the perturbation of the decay signal by the electrons in the TiO_2 is expected to be negligible.

The light intensities of observation and excitation beam have to be minimised to allow reproducible and reliable measurements. The observation beam was spectrally narrowed using band-pass filters and attenuated to less than 1mW/cm^2. The energy of the excitation beam was adjusted based on measurements of the change of the recombination kinetic as a function of the excitation beam intensity. Figure 3.4 illustrates the increase in recombination rate when increasing the laser energy from 0.04 mJ/cm^2 to 1.4 J/cm^2.
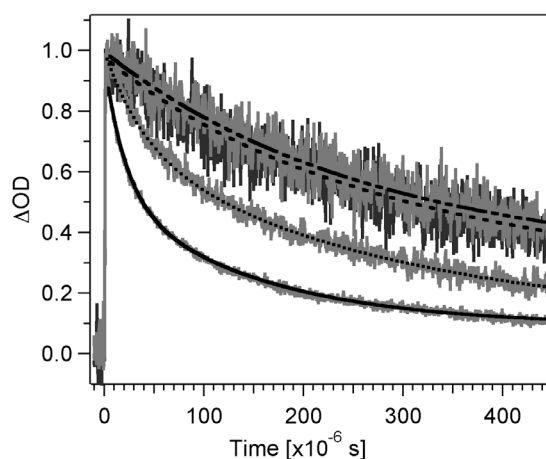
Figure 3.4: Dependence of recombination kinetics on energy of excitation beam. The spectra were normalised to a change in optical density of 1. The curves, followed from the bottom to the top of the graph, correspond to 1.4, 0.3, 0.1 and 0.07 mJ/cm^2.

The decay curve changed from uniform single exponential to bi-exponential. In all experiments, the excitation intensity was attenuated to 0.04 mJ/cm^2, which corresponds to less than one excited dye molecule per pulse per TiO$_2$ particle. The reproducibility of the measurements was controlled by monitoring the change of the ground state absorption maximum before and after the transient absorption experiments.

Experimental Setup

The pulsed laser photolysis were carried out using a pulsed Nd:YAG Laser as excitation source. The output wavelength was adjustable in the range from 400 nm to 700 nm by passing the laser beam through a broadband optical parametric oscillator (OPO). The pulse width (fwhm) was 5 ns for a repetition rate of 30 Hz and an energy of 1 mJ/cm^2. The laser beam energy was controlled by the adjustment of the energy dissipation in the discharge lamps responsible for the pumping of the laser and the use of attenuation filters in front of the beam. The energy of the laser beam incident on the sample was measured using a thermopile. The beam size was tuned by a plan concave lens to irradiate a sample area of ca. 1cm^2. The sample surface was kept at an angle of 30° to the excitation beam.

The absorption measurements were performed using a Xe arc lamp (Osram XBO, 450 W) as illumination source and a photodiode (SH 100) as detector at right angle to the exciting laser. The analysing light beam was passed through several band-pass filters before the sample and a grating monochromator between the sample and the detector. The data acquisition was established with a digital Tectronics oscilloscope.

Measurements employed the same device structure as for the photovoltaic experiments, without electrodes, i.e. the conducting SnO_2:F layer and the gold counter electrode (open circuit).

3.3 Kelvin-Probe Technique

The Kelvin probe technique is a non-contact and non-destructive method for measuring the potential difference between a reference probe and a sample surface. The sample and the reference electrode are setup in a capacitor arrangement. If electrical contact is made between probe and sample via the back contacts, the Fermi-levels of the sample and the reference electrode equalise, resulting in the generation of an electrical charge on the respective surfaces. This charge gives rise to a potential difference ΔU, which relates to the difference in work function:

$$-e \cdot \Delta U = \varphi_{ref} - \varphi_{sample} \tag{3.12}$$

If a potential U_{dc} is applied to the system that corresponds exactly to ΔU the surface charges will become zero. The space between the sample and the reference is varied while the plates remain connected under bias. The resulting change in capacitance of the capacitor induces a change in the capacitor charge and hence a current in the external circuit. This current can be zero only if the capacitor is discharged. The contact potential difference (CPD) between sample and reference is therefore easily found by determining the external bias for which no external current is observed. Knowing the work function of the reference electrode the work function of the sample is derived from:

$$\phi_{sample} = \phi_{ref} - U_{dc} \cdot e \tag{3.13}$$

The Kelvin Probe is therefore a technique that allows the indirect determination of very small charges, which makes it an extremely useful tool for the characterisation of high resistivity materials.

Experimental Setup

Kelvin Probe measurements were established using a Kelvin Probe setup from Besocke (Jülich, Germany). This setup includes a gold grid as reference electrode (ϕ_{ref}=5.1 eV, electrode surface area a=0.5 cm^2), which is mounted on an oscillator reed with a piezoelectric ceramic (Figure 3.5). The piezoelectric ceramic excites the reed mechanically with frequencies between 150 to 190 Hz, resulting in vibrational amplitude of the gold grid at the other end of the reed of about 1 mm.
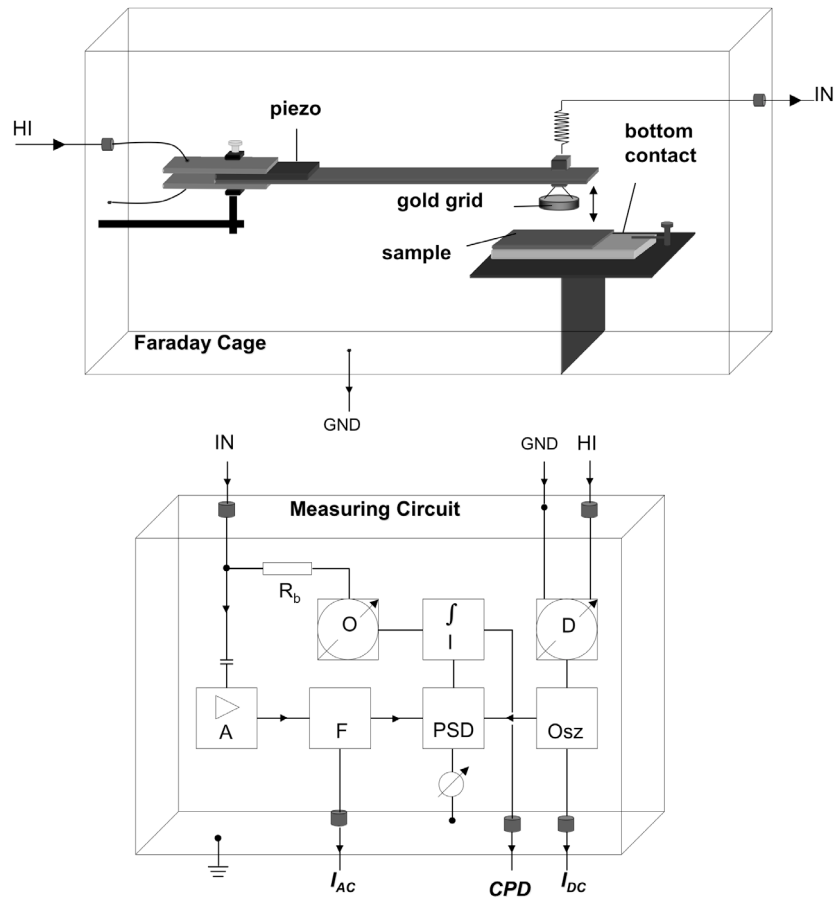
Figure 3.5: Scheme of Kelvin-Probe setup, including Faraday cage containing probe and sample and measuring circuit. A: pre-amplifier, F: tunable bandpass filter, PSD: phase sensitive detector, Osz: oscillation control of probe electrode, D: control of distance between sample and probe, I: control of integration time, O: precision offset voltage supply (used for manual adjustment of compensation potential, set to zero for automatic mode),

Stable vibrations are obtained by applying an appropriate AC voltage to the piezoelectric element (Osz). The reference-to-sample distance can be finetuned by DC biasing the piezoelectric element (D). A lock-in amplifier (PSD) is used to measure reliably the AC current at a specific vibration frequency which may be as low as a few fA ($C < 1$ pF), therefore a very large value for the resistor R_b (1 GΩ) is necessary, yielding voltages in the order of μV-mV. The contact potential difference CPD is obtained by applying the DC voltage necessary to nullify the AC current in reverse polarity back to the vibrating capacitor circuit. Reference and sample electrode are installed in a Faraday cage inside a glove box (argon atmosphere, H_2O < 10 ppm). The average reference-to-sample distance is about 0.5 mm. The whole setup was connected to one common earth connection to avoid obscuring of the experimental results by earth loops.

3.4 Frequency Resolved Techniques:
Electrical and Optical Impedance spectroscopy

DC techniques do not provide any information about internal system dynamics. Time dependent electrical and optical perturbations of the system of interest and the measurement of the transient response yield supplementary information about internal processes. The perturbations bring the system out of the equilibrium. In general the provoked electrochemical processes are non-linear and are typically described by an exponential expression, such as the Butler-Volmer Equation in the case of a semiconductor in contact with an electrolyte.[4] However, when the system is disturbed with a small harmonic signal superimposed on a steady state DC signal, a linearisation of the response is possible. Mathematically this linearisation is established by developing the exponential expression in a Taylor series and neglecting terms of higher order. The most common types of external perturbation involve small amplitude modulation of illumination intensity superimposed on a constant background illumination or application of a small potential perturbation on top of a large predetermined steady-state potential. Due to the internal electron transport the frequency resolved response lags behind the excitation signal showing a phase shift. The intensity modulated photocurrent spectroscopy (IMPS) measures the AC photocurrent resulting from the incident light modulation, whereas the Intensity modulated photovoltage spectroscopy (IMVS) measures the AC-photovoltage. IMVS measurements can be applied at any constant current.[5] In practice, however, this technique is limited to the special case in which no current flows through the external circuit, i.e. open circuit conditions. In contrast electrical impedance spectroscopy (EIS) is measured in every working state of the solar cell and measures the AC current resulting from potential modulation. The experimental outputs are given as optical admittance A_{IMPS} and A_{IMVS} respectively as electrical impedance Z_{EIS}:

$$Z_{EIS}(\omega) = \frac{\Delta U}{\Delta I} \cdot \exp(i \cdot \varphi) \quad A_{IMPS}(\omega) = \frac{\Delta I}{q \cdot \Delta \Phi} \cdot \exp(i \cdot \varphi) \quad A_{IMVS}(\omega) = \frac{\Delta U}{q \cdot \Delta \Phi} \cdot \exp(i \cdot \varphi) \quad (3.14)$$

with: ΔU=amplitude of AC potential, ΔI=amplitude of AC current, $\Delta \Phi$=amplitude of incident modulated photonflux and φ= phase shift.

EIS and IMVS are equivalent techniques, differing only in the location of the current source. In EIS, the current is a response to an external voltage source, whereas in IMVS, the current is generated in situ by the adsorbed dye on the TiO_2 surface. In IMVS the electrical properties of the electrodes do not contribute to the signal.

EIS data is in general analysed by fitting the transient response to an equivalent electrical circuit model. Most of the circuit elements in the model are common electrical elements such as resistors, capacitors, and inductors, representing physical processes in the system. The

measurement of the transient response to a perturbation should always be used as a check for a model of a physical system, rather than developing a model on the basis of the impedance spectrum. An assignments of circuit elements to physical processes should be done based in combination with other experimental techniques to derive information about the microscopic structure of a material. The description of a response behaviour is, however, unambiguous; i. e. more than one equivalent circuit can describe it.

Generally, characteristic frequency responses can be identified with particular physical elements. For instance, electrochemical interfaces are typically simulated by a parallel combination of a resistor and capacitor ("Voigt network"). In this respect a resistor is defined as an element, hindering the current throughput without inducing a phase shift (faradaic process) with respect to the voltage. Resistance of the material between electrodes is a significant factor for the overall impedance of the system, in particular in a two electrode-setup where no compensation for the IR drop can be easily calculated. For example the ohmic contact between the TCO and the TiO_2 would be represented as a resistor. Charge transport occurring via diffusion processes are typically described as a Nernst diffusion impedance.[6] The current flow over a charge transfer resistance is determined by the electrochemical reactions that occur at the electrode surface. Correspondingly the amount of current is controlled by the diffusion of reactants both towards and away from the electrode.

All systems that are able to store charge, such as dielectric double layers at the interface between a semiconductor and an electrolyte or the space charge layer between two semiconductors can be modelled by a capacitor. The value of such a double layer capacitor will depend on many variables including electrode potential, temperature, electrolyte composition, oxide layers and electrode roughness. The current passing a capacitor is shifted by $-90°$ with respect to the voltage. A value of $90°$ is rare; most real systems do not show this ideal behaviour. Accordingly a mathematically altered form of the capacity, the so-called constant phase element (CPE) is used. Several theories have been proposed to account for the non-ideal behaviour of space charge layers, but none has been universally accepted. The CPE is therefore only of empirical nature and is often related to electrode roughness, inhomogeneous reaction rates at surfaces, varying thickness or composition of coatings.

Inductors are characterised by a phase shift of the current with respect to the voltage by $+90°$. Inductors are rarely used for modelling of real systems. They are nevertheless included in this discussion as some authors have ascribed inductive behaviour to adsorbed reactants. The adsorption process and the electrochemical reaction are potential dependent; the net result of these dependencies can be an inductive phase shift in the cell current.

Another source for inductive behaviour is non-homogeneous current distribution. In many cases the inductance is induced by cell lead inductance and potentiostat non-idealities and represents an error in the EIS measurement.

Based on the discussed passive circuit elements several models have been developed for the DSSC.[7,8] The charge transfer across the TiO_2/electrolyte interface is typically represented by the parallel combination of a charge transfer resistance (R_{ct}) and a space charge layer capacitance (C_{SC}). The time constant of such an RC circuit corresponds to the time constant for interfacial charge transfer. Rate constants for recombination and charge transfer (mostly first-order respectively pseudo-first order) can only be simulated by an equivalent RC time constants if the external resistance is negligible.

Internal microscopic processes of charge recombination and charge transfer across the interface cannot be represented satisfactorily by single passive linear electric elements. Instead they are better described by rate constants and concentration terms. First-order rate constants for recombination and charge transfer can only be represented in principle by equivalent RC time constants if the external resistance is negligible. In any case R and C values have no physical significance on their own. The more complex these differential equations are, describing the physical system, the more difficult it is to find a mathematical solution. Often simplifying assumptions are needed in order to find a solution, which can be used to fit the measured data.

Model for analysis of optical impedance data

The experimental IMPS data have been analyzed making use of a model developed for the electrolyte-based dye-sensitized cells. This theory has been discussed in detail elsewhere,[9-11] and only a brief overview is given here. Small amplitude perturbation superimposed on steady illumination allows linearization of the periodic photocurrent response, and the effects of trapping can be taken into account explicitly or by using the effective diffusion coefficient approximation. Electron transport in dye-sensitized TiO_2 solar cell can be described by a continuity equation:

$$\frac{\partial n(x,t)}{\partial t} = G(x) + \frac{\partial J_n(x,t)}{\partial x} - R(x,t) \tag{3.15}$$

where $n(x,t)$ is the local electron concentration. The first term on the right is the rate at which electrons are generated by photosensitization. The second term involving the electron current density J_n describes the electron transport in the mesoporous network. The last term takes into account the loss mechanism, i.e. recombination processes. Several models have been proposed to solve this equation,[12-17] which differ mainly in the treatment of the electron trapping processes in the TiO_2 network. In the present work the model of Dloczik et al.[9] has

been used, which. treats the effect of trapping by using an effective diffusion coefficient $D_{eff} = D \cdot n_{free} / n_{total}{}^{*}$ to describe electron transport. In the limit of small amplitude modulation, the recombination term can be expressed as a first order decay of the electron density characterized by a pseudo-first-order electron lifetime τ_n. Because of the small TiO_2 particle size, which does not allow any band bending, electron transport in the TiO_2 is dominated by diffusion. Based on these assumptions the continuity equation becomes:

$$\frac{\partial n(x,t)}{\partial t} = \eta \cdot \alpha \cdot exp(-\alpha \cdot x) + D_{eff} \frac{\partial^2 n(x,t)}{\partial x^2} - \frac{n(x,t) - n_0}{\tau_n} \tag{3.16}$$

where α is the absorption coefficient determined by the dye coverage and the surface area/volume ratio of the nanocrystalline electrode, η is the electron injection efficiency, and n_0 the electron concentration in the dark. Equation 1.14 has been solved assuming that electrons are extracted at the back contact over a potential-dependent energy barrier with a characteristic extraction rate. For high values of the extraction rate constant, the current becomes diffusion controlled. The predicted IMPS response appears in the lower complex plane as a consequence of the phase lag arising from the time required for electrons to diffuse to the back contact. The measured external current can be obtained by multiplication of the theoretical internal current by an attenuation factor:

$$T = \frac{1 - i\omega \cdot R \cdot C}{1 + \omega^2 \cdot R^2 \cdot C^2} \tag{3.17}$$

Here R is the series resistance of the contacts and C is the capacitance of the contacts.

Bode plots, as well as the complex plane plots were fitted using a nonlinear-least-squares fit program ("Igor" software, Wavemetrics), based on the Levenberg-Marquardt algorithm. The constant parameters in the fits of the current responses were derived independently. An initial estimate for the absorption coefficient $\alpha = A / d$ was determined from absorption spectroscopy and film thickness measurements (Alpha step). Light scattering of the 2 μm thick TiO_2 films is negligible. Reflection at the 20 nm thick gold film was neglected. Light absorption by the hole conductor radical cation was considered empirically by defining an effective absorption coefficient, which was derived from the fit of the highest light intensity IMPS response. A high value of the extraction constant (10^4 cm/s) was chosen to correspond to diffusion-controlled electron extraction under short circuit conditions. D_{eff} and τ_n were varied to obtain the best fit to the measured curve. The values for R and C were obtained by impedance measurements under comparable illumination

---

* n_{free} is the density of free conduction band electrons and n_{total} is the total density of free and trapped electrons.

conditions. Consideration of the attenuation factor improved the fit of the curve at high frequencies, but changed the value for the diffusion coefficient only slightly.

The theory of the IMVS response has been discussed in detail by Schlichthörl.[5] For the present analysis it is sufficient to note that the small amplitude photovoltage response is characterized by a first order electron lifetime τ_n, which is the inverse of the pseudo first order rate constant for electron hole recombination. The IMVS response is therefore a semicircle in the lower complex plane with a minimum at $\omega = \tau_n^{-1}$.

Experimental Setup

The experimental set-up for IMPS and the IMVS measurements has been described previously[18] and is shown schematically in Figure 3.6. Intensity-modulated measurements were carried out using a Solartron 1250 frequency response analyzer, which is used to drive a LED and to measure the optotelectronic transfer functions. The LED (λ = 480 nm) provided both the DC and AC components of the illumination. The modulation depth of the AC component superimposed on the DC light was 8 %. The light intensity was adjusted using calibrated neutral density filters (Schott). Photocurrents were measured using a battery-operated potentiostat consisting of low-noise operational amplifiers. Photovoltages were measured using a high-impedance low-noise battery-operated pre-amplifier (Stanford SR560: input impedance 10^8 Ω). The entire setup was placed in a faraday cage to minimise electrical noise.
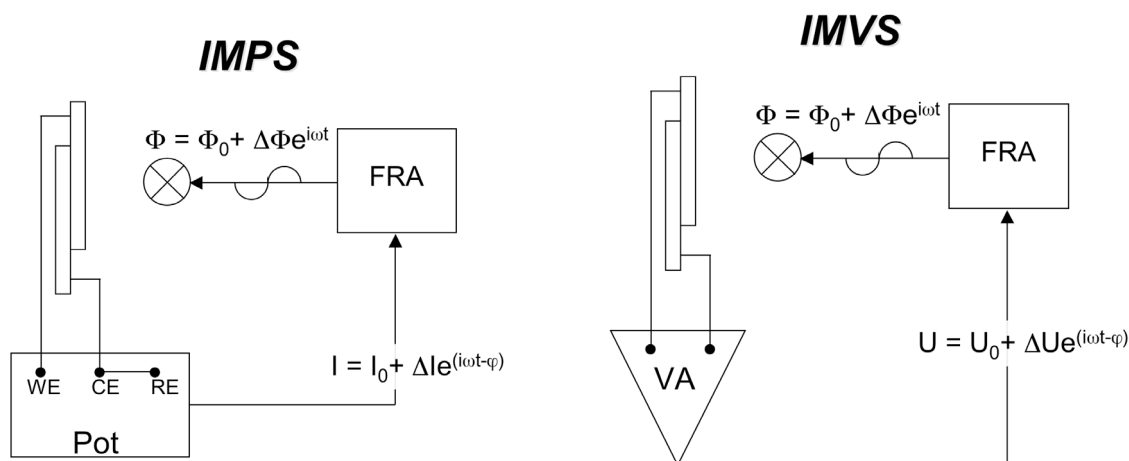

Figure 3.6 Scheme of IMPS and IMVS set-up.

The EIS measurement were performed using an Autolab measuring unit incorporating a frequency analyzer (FRA2 Module) and a potentiostat (PGSTAT12), which allows AC-impedance measurements in a frequency range from 10 μHz up to 1 MHz at a fixed DC potential or during a potential scan. A LED has been employed as light source that was

similar to the one used for the optical impedance measurements. LED and sample were placed in a faraday cage which allowed the complete exclusion of any other light. The light intensity was about 2 mW/cm^2 and therefore comparable to the light intensities employed for the IMPS respectively IMVS and the IPCE measurements. Fitting of the data to equivalent circuit models were established using either the FRA software supplied by Autolab$^©$, which is based on the program EQUIVCRT[19] or the Impedance Analysis software ZPlot available from Solartron Analytical.[*]

In this work data is presented in form of Nyquist plots (imaginary versus real part of the complex impedance) as well as in form of Bode plots (i.e. magnitude vs. logarithm of the frequency respectively phase shift as function of the logarithm of the frequency). The advantage of the logarithmic presentation in form of the Bode plots is that for data including a large frequency range no data compression is obtained as is the case in the Nyquist plot.

3.5 XPS

X-ray photoelectron spectroscopy (XPS) is a powerful surface analysis technique, which provides elemental information about a surface as well as chemical state information (electron spectroscopy for chemical analysis (ESCA)). A sample material is bombarded by monoenergetic soft X-rays, causing electrons to be ejected. Emitted photoelectrons are collected as a function of their energy from which binding energies can be obtained using the Einstein equation:

$$E_b = h\nu - E_k - \Phi \qquad (3.18)$$

where E_b is the binding energy of the electron, E_k its kinetic energy and Φ the work function of the spectrometer. On a finer scale it is also possible to identify the chemical state of the elements present from small variations in the determined kinetic energies.

The relative concentrations can be obtained with a sensitivity of 0.1-1 % of a monolayer (around 10^{15} atoms/cm^2) from the measured photoelectron intensities. The intensity I_A of a photoelectron peak of element A is given by:

$$I_A = I_{RX} \cdot \sigma_A \cdot f(E_K) \cdot \int_0^\infty C_A(z) \cdot \exp(\frac{-z}{\lambda_A \cdot \sin\alpha}) \cdot dz \qquad (3.19)$$

where I_{RX} is the intensity of the incident X-rays, σ_A the cross section of emission of a photoelectron from an inner core shell of A, $f(E_k)$ the detection efficiency of the spectrometer for a photoelectron with a kinetic energy E_k, $C_A(z)$ the concentration of element A as a function of the depth z, λ_A the inelastic mean free path of a photoelectron emitted by A and

---

[*] http://www.solartronanalytical.com/software/software.html

α the take-off angle of the photoelectron with respect to the surface of the sample. In a homogeneous matrix, the concentration of C_A can be approximated by the relation:

$$C_A = \frac{\dfrac{I_A}{S_A}}{\displaystyle\sum_{i=0}^{n} \dfrac{I_i}{S_i}}$$ (3.20)

with S_i as the relative atomic sensitivity factor.

XPS probes 2-20 atomic layers (3-10 nm) deep for a solid sample. The energy of the photoelectron depends on the angle (with respect to the surface) of the measurement. The escape depth z of the photoelectron depends on its inelastic mean free path length λ as well as on its emission angle α with respect to the surface. The sampling depth can therefore be varied by making use of the equation:

$$z = \lambda \cdot \sin\alpha$$ (3.21)

The lateral resolution of this technique is around 2-10 μm.

The particular strengths of XPS are semi-quantitative elemental analysis of surfaces, as well as chemical state analysis for vacuum-compatible materials as diverse as biological to metallurgical samples. Due to the very small emission cross section and the corresponding long analysis times, this technique is not applicable for hydrogen and helium.

Experimental Setup

XPS analyses were performed at the *Laboratory of Metallurgical Chemistry* (EPFL-LMCH-DMX). The XPS consists of a Axis Ultra spectrometer from Kratos (Kratos, Manchester, U.K.) equipped with a concentric hemispherical analyzer and using a monochromatised aluminium anode X-ray source (a K$\alpha_{1,2}$ 1486.6 eV, full width at half maximum, fwhm = 0.85, 15 kV, 150 W). Dye-sensitised TiO_2 films with a thickness of 1 μm were investigated under ultrahigh vacuum conditions: 10^{-8}-10^{-7} Pa. Spectra were taken at a 90° takeoff angle with respect to the surface. A sample area of 300 x 700 μm^2 was analyzed with a pass energy of 80.0 eV for survey scans and 40.0 eV for high resolution elemental scans. The spectrometer was calibrated using Cu 2p3/2 (932. eV) and Au 4f7/2 (84.0 eV) signals. Atomic concentrations were determined based on Scofield's surface sensitivity factors.[20] The C 1s spectrum of C-H/C-C at 285.0 eV served as reference for the determination of peak positions. After background subtraction, the spectra were fitted by assuming a Gaussian/Lorentzian (90-70/10-30) peak shape except for the asymmetric Ti metallic peak. The experimental data was analyzed using the software CasaXPS.[*]

---

[*] http://www.specs.com/products/ESCA/software/CASAXPS/CasaXps.htm

3.6 Absorption and Fluorescence Spectroscopy

In context with the research on organic solar cells electronic excitation spectra are extremely useful for characterisation of dye uptake and doping of the organic semiconductor. Due to its low time consumption, and its generally non-destructive character the UV/VIS spectroscopy can easily be included in the preparation process of the solar cell.

Experimental Setup

Absorption spectra were recorded using a spectrometer with a diode array (HP Chemstation 8453) or a Varian spectrophotometer (Cary), depending on the sample properties and the requirements in terms of signal-to-noise ratio. For Reflectance measurements the Cary spectrometer was equipped with an integrating sphere. UV/VIS spectra of solutions were recorded in a 1 cm path length quartz cell. Thin dye-sensitised films were measured in ethanol to reduce interference effects that might obscure the absorption spectrum. A special cuvette to fix the film close to the cuvette window[21] was used for these measurements.

Fluorescence spectra were measured on a SPEC Fluorolog Fluorimeter II, equipped with a Xe-lamp, a single monochochromator for the excitation and a double monochromator for the emission spectrum. A Hamamatsu R2658 photomultiplier was used for the detection. Fluorescence spectra of solutions were recorded in a right angle geometry. The optical density of the reference and sample were kept below 0.02 for the determination of fluorescence quantum yield. The excitation of solid samples was established in a front face geometry with an active mode-locked Nd YAG laser pulse, using the frequency-doubled line at 532 nm. All solvents were dearated before measurements (N_2 bubbling, 15 min).

Absorption and emission spectra were analyzed based on the Gauss curve shape model (Multi peak fit package, Igor software, WaveMetrics Coorperation, Lake Oswego, OR).

3.7 FTIR-Spectroscopy

Vibrational spectroscopy provides the most definitive means of identifying surface species generated upon molecular adsorption and the species generated by surface reactions. It is based on the fact that infrared illumination stimulates molecular vibration (and rotation). Energy will only be absorbed if there is a net change of dipole moments due to the vibrational motion of the molecule, i.e. a transition dipole moment. This energy adsorption can be monitored making use of several different techniques, from which Fourier Transform Infrared (FTIR) spectroscopy has become the standard technique for chemical

characterisation. With the development of attenuated total reflection (ATR) or internal reflection spectroscopy FTIR gained importance as a straightforward and non-destructive tool for surface characterisation. The ATR technique is based on the fact that a material will reflect much of the incident radiation depending upon its actual reflectivity, when the angle of the incident light is different from zero degree. If an IR transparent crystal such as diamond is placed behind and in good optical contact with the sample, light passing into the diamond can be made to emerge on the opposite side having made a reflection at the diamond-sample interface. The number of reflections N the light will undergo as it propagates down a crystal with the thickness W and the length L before emerging at the other end is given by:

$$N = \frac{L}{W}\text{cotan}(\phi) \qquad\qquad (3.22)$$

At each reflection, an evanescent electric field (E) is generated in the sampled medium, the intensity of which decays exponentially with distance (z) from the surface:

$$E = E_0 \cdot \exp[\frac{-z}{d_p}] \qquad\qquad (3.23)$$

where E_0 is the intensity of the incident radiation and d_p the penetration depth, which is a function of the refractive index η_1 of the ATR crystal, refractive index η_2 of the sample medium, and the angle of incidence θ:

$$d_p = \frac{\lambda}{2 \cdot \pi \cdot \eta_{12}\sqrt{\sin^2\theta - \eta_{12}}}, \text{ with: } \eta_{12} = \frac{\eta_2}{\eta_1} \qquad\qquad (3.24)$$

Considering the refractive index of diamond and a typical organic polymer to be 2.4 and 1.5 respectively, the top 2 μm of the surface will be sampled at 45º incidence. The intensity of the reflected light at each reflection point will be reduced by the presence of infrared absorbing material in the sample medium. The emerging light contains important absorbance information about the sample. The quality of ATR spectrum is dependent on sample contact rather than sample thickness.

Even higher signal resolution can be obtained from photoacoustic spectroscopy (PAS).[22] PAS is mainly used to study inorganic surfaces, but it is also applicable to the solid phase. The principle of PAS relies on heat transfer.[23] The modulated infrared radiation is directed towards the sample. Absorbed radiation is transformed into heat which is then transmitted to the surrounding inert gas resulting in local pressure variations, which are detected by a sensitive microphone. The technique is less sensitive to interference such as light scattering or reflection since it does not record the resulting infrared wave, but is dependent on thermal diffusion. PAS directly measures the absorbance spectrum of the layer without having to

infer the desired absorbance spectrum based on a reflection or transmission measurement. The spectral range of a photoacoustic detector depends only on the transparency of the sample chamber window. With suitable windows a detector can operate from the UV to the far-infrared. The main inconvenience of this method is that the analysis chamber must be flushed with an inert gas to avoid interferences with atmospheric pollutants.

Experimental Setup

FTIR spectra were measured using a Digilab FTS-7000 step-scan spectrometer (Randolph, MA), equipped with a DTGS detector. Dyed films and dye solutions were measured using an attenuated total reflectance (ATR) accessory based on a single reflection diamond element (Specac, Orpington, Kent, UK). The diamond ATR top plate was mounted onto a fully enclosed beam condensing optics box used to focus the IR beam. Typically this results in a sensitive sampling area of approximately 1mm in the centre of the diamond crystal. Solid samples are forced into almost perfect optical contact with the diamond using a sapphire anvil assembly mounted overhead on a unique swing bridge. Reproducible loads of 3 kbar can be applied using a special torque wrench supplied with the unit. Solutions were covered with a plastic cap to avoid solvent evaporation. The beam condensation is achieved using lenses of ZnSe,(transmission to around $650 cm^{-1}$) in combination with mirrors. The spectra were recorded at a resolution of $4 cm^{-1}$ in a spectral range of 400-4000 cm^{-1}(Rapid scan mode). The absorption spectra were the result of an average of 64 scans, recorded at room temperature. The digital signal processing (DSP) algorithm incorporated into the Bio-Rad spectrometer software was used for the data acquisition. The FTIR spectra of dye-sensitised films where corrected for the absorption of the TiO_2 by subtraction of a pure, preheated TiO_2 layer of the same thickness.

For the PAS measurements the ATR accessory was replaced by a helium-purged MTEC300 photoacoustic cell (Portmann Instrument AG). The Helium purging of the sample and microphone volumes enhances sensitivity by a factor of 2 to 3, allows higher frequency operation, and removes moisture and CO_2. Water vapour from the sample after being sealed in the sample chamber is minimised by a cup of desiccant ($MgClO_4$) which is placed in the sample holder beneath the sample cup. Under ideal working conditions a peak-to-peak noise of less than 0.2 % at 2000 cm^{-1} can be expected. The setup has been used in step-scan mode. Typically 256 scans at a resolution of 2 cm^{-1} were used to collect the spectra in the range from 400 to 4000 cm^{-1}.

3.8 References

[1] C. H. Seaman. *Sol Energy* **1982**, *29*, 291-298.

[2] C. von Planta. Ph.D. Thesis, EPFL, 1996.

[3] G. Rothenberger, D. Fitzmaurice and M. Grätzel. *J Phys Chem* **1992**, *96*, 5983-5986.

[4] N. Shaw. Ph.D. Thesis, University of Bath, 1999.

[5] G. Schlichthörl, S. Y. Huang, J. Sprague, et al. *J Phys Chem B* **1997**, *101*, 8141-8155.

[6] R. Kern, Ph.D. Thesis, Albert-Ludwigs-Universität Freiburg i. Brsg., 2001.

[7] J. van de Lagemaat, N. Park and A. Frank. *J Phys Chem B* **2000**, *104*, 2044-2052.

[8] T.-S. Kang, K.-H. Chun, J. S. Hong, et al. *J Electrochem Soc* **2000**, *147*, 3049-3053.

[9] L. Dloczik, O. Ileperuma, I. Lauermann, et al. *J Phys Chem B* **1997**, *101*, 10281-10289.

[10] G. Franco, L. M. Peter and E. A. Ponomarev. *Electroch Commun* **1999**, *1*, 61-64.

[11] N. G. Park, G. Schlichthörl, J. van de Lagemaat, et al. *J Phys Chem B* **1999**, *103*, 3308-3314.

[12] E. A. Ponomarev and L. M. Peter. *J Electroanal Chem* **1995**, *397*, 45-52.

[13] G. Schlichthörl, N. G. Park and A. J. Frank. *J Phys Chem B* **1999**, *103*, 782-791.

[14] J. v. d. Lagemaat and A. J. Frank. *J Phys Chem B* **2000**, *104*, 4292-4294.

[15] T. Yoshida, A. Shinada, T. Oekermann, et al. *Electrochemistry* **2002**, *70*, 453-456.

[16] P. E. d. Jongh and D. Vanmaekelbergh. *Phys Rev Lett* **1996**, *77*, 3427.

[17] P. E. d. Jongh and D. Vanmaekelbergh. *J Phys Chem B* **1997**, *101*, 2716.

[18] L. M. Peter and K. G. U. Wijayantha. *Electrochim Acta* **2000**, *45*, 4543–4551.

[19] B. A. Boukamp. Equivalent Circuit (EQUIVCRT.PAS), 1988.

[20] J. H. Scofield. *J Electron Spectrosc* **1976**, *8*, 129.

[21] S. Gattoni, Ph.D. Thesis, EPFL, 2001.

[22] F. Gosselin, M. D. Renzo, T. H. Ellis, et al. *J Org Chem* **1996**, *61*, 7880-7981.

[23] J. F. McClelland, S. J. Bajic, R. W. Jones, et al. Photoacoustic Spectroscopy. In *Modern Techniques in Applied Molecular Spectroscopy*; Mirabella (Ed.) ed.; Wiley: New York, 1998; pp Chapter 6, pp. 221-265.

4 DEVICE PREPARATION

This chapter discusses the materials and technique used for the preparation of solid-state dye-sensitised solar cells (SSD). The device is based on a monolithic design. The TiO_2 photocathode, the hole conductor film and the counter electrode are fabricated successively in a multi-step process, employing wet and dry processing techniques.

4.1 Materials

Unless otherwise stated all chemicals were purchased from Aldrich (Switzerland) and at least reagent grade, respectively puriss. p.a. for solvents.

Chlorobenzene and Acetonitrile, used for the preparation of the spin-coating solution contained less than 0.01 % and 0.1 % H_2O (Karl-Fisher Analysis) respectively and were stored under inert atmosphere until use.

Solution of additives for the spin-coating solution, such as $Li[(CF_3SO_2)_2N]$ in acetonitrile, were prepared and stored in dry atmosphere.

tert-butylpyridine (*t*BP) were purchased from Fluka, purified by distillation (Fischer column) and stored under dry atmosphere until use.

The standard dyes N3 ($[Ru(2,2'-bipyridyle-4,4'-dicarboxylate)_4(NCS)_2]H_4$) and N749 ($TBA_2[Ru(H_2tcterpy)(NCS)_3]$) were supplied by Solaronix (Aubonne, Switzerland) and were dissolved in a 1:1 mixture of acetonitrile:tert.-butanol or in ethanol The deprotonated form of the dye (N719, $[Ru (2,2'-bipyridyle-4,4'-dicarboxylate)_2(NCS)_2]H_2(Bu_4N)_2$) was obtained by adding two dye equivalents of a solution of 40 % tert.-butylammonium hydroxide in H_2O to the N_3 solution. All other dye solutions used were supplied by Dr. Mhd. Nazeeruddin and Dr. S. Zakeeruddin (LCMB, EPFL) and were used as received.

Di-iso-propoxytitanbis(acétylacétonate) (TAA), used as precursor for the spray-pyrolytic deposition of compact TiO_2 layers was purchased from Fluka. The TAA was stocked under inert atmosphere and was diluted with ethanol to a final concentration of 0.02 M prior to use. Under normal atmospheric conditions the color of the precursor solutions changed from yellow to orange. Although current-voltage characteristics of layers prepared from aged solutions and from fresh solutions did not show any significant difference, precursor solutions were always prepared freshly before use.

2,2',7,7'-tetrakis(N,N-di-p-methoxyphenyl-amine)-9,9'-spirobifluorene (spiro-MeOTAD) was supplied by Covion Organic Semiconductor GmbH, Frankfurt/Germany (purity>99.8 % HPLC analysis) and was used as received.

Screen-printable TiO_2 colloids pasts for the preparation of the nanocrystalline TiO_2 layers were prepared by P. Comte following the procedure described by Barbé:[1]

1. *precipitation* (hydrolysis of Ti-alkoxides using 0.1 M HNO_3)

2. *peptisation* (heating at 80 °C for 8 h) followed by filtering

3. *hydrothermal growth/autoclawing* (12)

4. *sonification* (ultrasonic bath, 400 W, 15 x 2 s)

5. *concentration* (45°C, 30 mbar)

6. *binder addition* (carbowax/Polyethyleneglycol, M_w=20 000)

The porosity, particle size and specific area for the different TiO_2 colloids used in the present work are summarised in Table 4.1. Compared to the TiO_2 films in electrolyte cell, TiO_2 films in the SSD have a higher porosity to improve the filling of the TiO_2 network with the spiro-MeOTAD. Upon dye uptake the effective porosity of the TiO_2 film is reduced by about 25 %. The dye deposition influences the more the porosity of the film, the more the pore size distribution is centred at low values.[2]

Colloid Name	Porosity [%]	Particle Size [nm]	Specific Surface [m^2/g]
JDD1x-S7	69.3	15	104
RCO1x-S1	65.3	15	105
PC100x-S2	66	19	83
PC117	65.1	19.5	83
PC131	65	15	104

Table 4.1: Characteristic parameters for different nanocrystalline films prepared and characterised by P. Comte. The pore size and specific surface area have been derived from N_2 adsorption experiments (BET). The porosity was calculated from the ratio of the cumulative pore volume V_p, to the total volume V_{tot}, which is given by $V_{tot}=V_P+\delta(TiO_2)^{-1}$. (density of anatase $\delta(TiO_2)$=3.85 g/cm^3).

4.2 General Device Assembly

Two different types of devices were employed for the studies: a device with four small diodes possessing an active area of 0.16 cm^2, and a larger device with an active area of about 1 cm^2 (Figure 4.1). The device bearing four active diodes has been used for device parameter screening purposes, yielding information about the device homogeneity. The large device design was used for physical characterisations, such as the impedance studies, as it simplifies the encapsulation of the photovoltaic active area. Compared to the small diode device the large device has been improved in respect of resistive losses and definition of the active area. This becomes evident when comparing the photovoltaic characterisation of the two device types measured with and without mask. The difference in performance for the small diode device is around 10 %, whereas it is negligible for the large cell. Furthermore measurement errors caused by the interaction of the incident irradiation with the borders of the mask are less important for the large cell geometry as for the device containing for small diodes. Accordingly, not loss in performance is obtained for the large cell, although the active area is a factor of 5 higher.
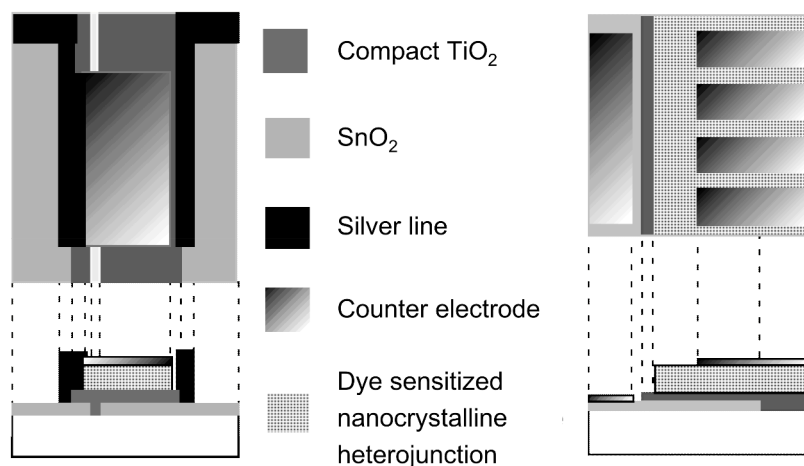

Figure 4.1: Schema of large active area and small active area device.

4.2.1 TCO Substrates

If not stated otherwise TCO substrates were chemically structured using Zn granulate (20 mg/cm^2) in combination with either 4N HCl or 2 M citric acid (1 ml/cm^2). Scotch$^{©}$ tape was used to mask a TCO area for the back contact in the final device. The use of HCl has

the advantage of a fast removal of the SnO_2 layer. After two treatments of 3 min reaction time the SnO_2 is completely removed. However, for some types of TCO substrates and for fine structuring HCl is too vigorous, leading to very irregular etching borders. In this case citric acid has been used, which enables a more exact structuring but increases the reaction time up to 45 min. The structured TCO layers were purified by subsequent sonification in various solvents (1 x acetone, 2 x ethanol, 1 x Hellmanex$^{®}$ (2 % in H_2O), 3 x H_2O, 2 x ethanol) for 10 min in each solvent. Cleaned substrates were stored in pure ethanol. Prior to deposition of TiO_2 the layers were additionally cleaned by an UV/Ozone treatment (UVO-Cleaner®, Model No. 256-220, Jelight company Inc.) for 15 min.

Choice of the TCO

An effective TCO should have high electrical conductivity combined with low absorption of the visible light. However, the decrease of resistivity is correlated with a decreased transmission for a given material. Correspondingly the two parameters have to be optimised for the application of interest. In particularly for device used without compact TiO_2 layer the interfacial and material-compatibility properties of the TCO are also important, determining the attachment of the deposited material to the TCO.

The TCO should pass the demanding processing conditions for the device preparation without change of its physical properties. The resistance of TCOs will increase, if heated to high temperatures and for long time. However, the TCO typically remains stable up to temperatures slightly above the optimised deposition temperature. Fluorine doped SnO_2 films are generally very stable, so that the softening of the glass substrate is more limiting than any thermal decomposition of the conducting layer. In contrast indium tin oxide (ITO) films, used in particularly for the preparation of OLEDs, show significant losses of conductivity upon heating over 200°C.

A selection of commercially available TCOs has been compared concerning their optical and electronic properties as well as their thermal stability. As a quantitative measure (figure of merit) for the performance of the TCO the ratio of the resistance to the transmission of 550 nm radiation has been used. A small value indicates better performance of the TCO. Table 4.2 demonstrates that all glass types are thermally stable except for the Asahi glass. The Solaronix glass and the Tec8 glass showed the best performance. However, at the time of these experiments the Solaronix glass was not available on larger scales. On the other hand the chemical structuring of the Tec8 glass is difficult. For reasons of availability Asahi glass has been used for device parameter screening purposes, avoiding sintering temperature over 450°C. For high performance devices NSG and Solaronix glass were used.

Glass type	T_{550} [%]	R_0 [Ω/□]	R_1 [Ω/□]	R_2 [Ω/□]	R_0/T [Ω/□]
Solaronix (9 Ω/□, 1mm)	85	8.4	8.6	8.8	0.10
Asahi, (10 Ω/□, 1mm)	82	13.5	12.5	60.2	0.16
NSG (12 Ω/□, 1mm)	82	12	12.9	14	0.15
Tec8 (8 Ω/□, 3mm)	80	7.7	7.7	7.9	0.10
Tec15 (15 Ω/□, 3mm)	82	13	14.6	14.3	0.16

Table 4.2: Comparison of TCO substrates commonly used for the preparation of SSD and DSSC, with T=Transmission at 550 nm, R_0=initial resistance, R_1=resistance after first sintering, R_2= resistance after second sintering, and R_0/T=figure of merit. In parenthesis behind the glass type the nominal resistance of the glass is given as well as the thickness of the glass. Resistance measurements have been performed using the four-point technique.[3,4] The sintering involved heating at 500 °C for 10 min (heating rate 10 min).

4.2.2 Compact TiO$_2$ Layer

Compact films of TiO$_2$ were deposited by aerosol pyrolysis of the precursor TAA[®], according to the procedure described by Kay[5] respectively Kavan.[6] The samples were heated to 450 °C (NiCr/Ni thermopile) on a temperature-controlled hotplate and the precursor solution was sprayed from a distance of 20 cm using a chromatographic atomiser (Glas Keller, K1596). For layers of about 100 nm thickness 30 spray processes of roughly 75 µl precursor solution with an interval of 10 sec were performed, which corresponds to an overall consumption of 0.09 ml/cm^2. The interval between each spray process allows the complete evaporation of precursor solvent and to restore the original substrate temperature. Thin 1 mm float glass, structured by a sandblast, was used as mask to cover lines of SnO$_2$ for later contact formation. The substrates were thermally equilibrated on the hotplate for 5 min prior to the spray-coating process and left for at least 10 min after the deposition, to complete the transformation of the precursor to TiO$_2$ and to evaporate residual organics. Layer thickness measured by electron microscopy was approximately constant for 20 to 30 spray processes. Nevertheless layers prepared with 30 spray processes were more homogeneous and dense, and give more reproducible current-voltage characteristics. The compact nature of the TiO$_2$ layer manifests itself by a perfect blocking of anodic reactions on the bare TiO$_2$ electrode. The resulting TiO$_2$ layer posses mainly anatase character[6] and is presumably n-doped.

4.2.3   Nanocrystalline TiO$_2$ Layer

20 mm broad stripes of TiO$_2$ paste were deposited by manual screen-printing, respectively squares of 2*0.8 cm^2 for the large area device. After the coating step the films were allowed to saddle for about 30 min at room temperature under normal atmospheric conditions in a dust free container. The layers were then fired to remove organic additives and to sinter particle to a mechanically adhering and electrically conducting film. A special sintering program has been followed to obtain reproducible grain growth and phase transformation during the sintering. The temperature program consists of heat ramps and isotherms, that are chosen to separate the combustion of the additives and the sintering in time. This was done in order to avoid contamination due to carbon inclusions, a problem, which may occur if organics are trapped in pores, which close during calcination before they can burn off. The upper sintering temperature, which is typically 500-600 °C, is determined by the physical properties of the substrate (compare chapter 4.2.1). The firing atmosphere is affecting the doping of the TiO$_2$. Firing an oxide in a reducing atmosphere such as hydrogen for example may create oxygen vacancies, which leads to n-type doping. Previous work by Kay[5] has shown that best results for the TiO$_2$ colloids are obtained for sintering in dry air or under a constant flux of oxygen.
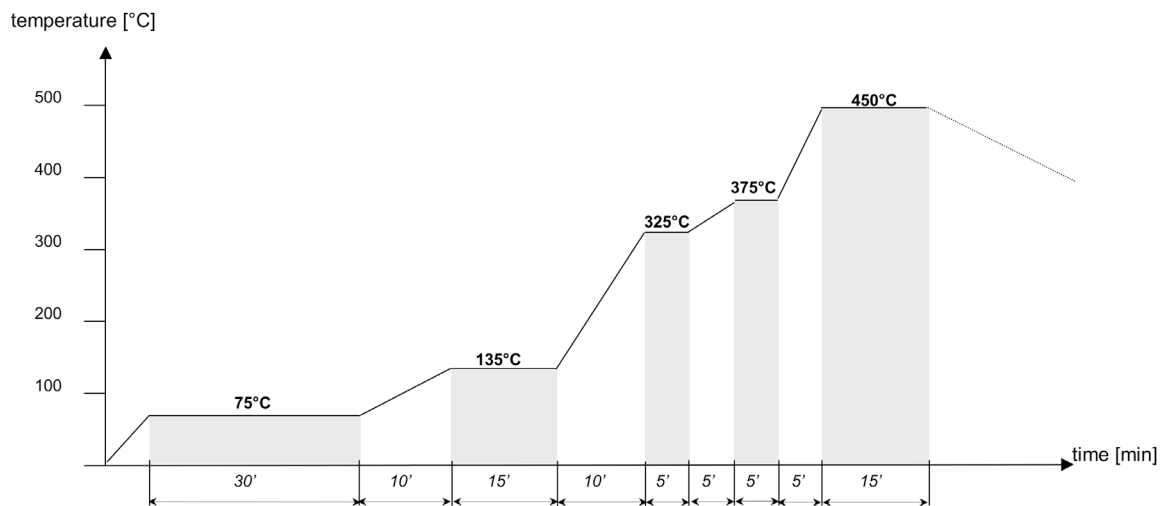

Figure 4.2: Temperature program for sintering of screen-printed films.

TiO$_2$ films of different thicknesses could be realised using appropriate screens in combination with pastes of different TiO$_2$ colloid contents and different amounts of organic additives. As the filling of the pores is not only dependent on the properties of the pores in the nanocrystalline network but also on a variety of other parameters, such as post

treatments of the TiO_2, the dye coverage or the properties of the spin-coating solution, a pre-estimation of the pore filling is difficult. The layer thickness of the TiO_2 has been therefore optimised for a given set of colloid, dye and spin-coating solution on the base of the photovoltaic performance of the corresponding device. If not otherwise specified no scattering particles were added to the TiO_2 pastes and the films obtained where highly transparent.

In general TiO_2 films were subject to a $TiCl_4$ post-treatment. This treatment has been shown to increase the injection of electrons into the TiO_2 and thus the current that is delivered by the solar cell. The positive effect has been assigned to the increased surface area for dye adsorption and to the formation of a native surface TiO_2 layer of higher purity. Furthermore Ti complexes in $TiCl_4$ solution are believed to condense at interparticle necks, thereby increasing the interparticle connection and the electron percolation. However, the treatment causes a decrease of the average pore size and the porosity. Therefore the $TiCl_4$ concentration and time of treatment needs to be optimised regarding the required pore size.

50 µl/cm^2 of a 0.02 M $TiCl_4$ solution were applied to the nanocrystalline film for 12 h at room temperature in a dust free environment. Contact areas were protected with adhesive tape. Afterwards the samples were washed with a large amount of distilled water and sintered for a second time for 15 min at 450 °C (ramp: 10 min).

4.2.4   <u>Sensitiser</u>

If not used directly after preparation, the TiO_2 films were stored in a desiccator over silica gel until the final assembly of the solar cell. Before the dye uptake TiO_2 layers were again heated to 450 °C for 15 min. The firing leads to a partially dehydroxylated, highly activated surface for dye adsorption. Typically the nanocrystalline TiO_2 films were soaked in the corresponding dye solution for 16 h in the dark prior to the spin-coating process.

Influence of Dye Structure

Beside the requirements for an efficient sensitiser discussed in chapter 2, the dye structure has also an influence on the quality of the heterojunction between TiO_2 and the hole conductor. For related organic devices, such as LEDs, the consequences of the introduction of organic molecules on the band energetics, morphology, and stability (hydrophobicity) of organic/inorganic contacts have been studied in detail. Goncalves-Conto et al.[7] have demonstrated that the wettability of ITO substrates by organic semiconductors can enable adsorption of self-assembled monolayers (SAM) of appropriate molecules onto ITO. Similarly the spin-coating of the hole conductor leads to films of better quality when the

deposition has been established on the dye-sensitised TiO_2 instead of the pure TiO_2. A dye with organic chains pointing towards the hole conductor might therefore diminish the activation energy for the hole conductor to fill the nanoporous network.

On the other hand Bauer[*] has shown that the introduction of a spacer between attachment group and redox center of the dye is slowing down the injection rate. This result is less important for the performance of the solar cell, since the injection is still much faster than the competing reactions. However, voluminous organic chains pointing towards the hole conductor might have a similar influence on the interception kinetics, and what is even more important, might shield the TiO_2 surface and therefore affect also recombination kinetics.

The influence of the structure and the electrostatic properties of the sensitiser on the heterojunction TiO_2/spiro-MeOTAD was studied using a series of ruthenium dyes with systematically differing hydrophobic character, which were obtained by the systematic exchange of the substituents at the bipyridyl ligands of the N3 type of dye (Figure 4.3). For the sake of simplicity molecule names have been defined, indicating the number of C atoms in the organic chain situated at the bpy ligand.

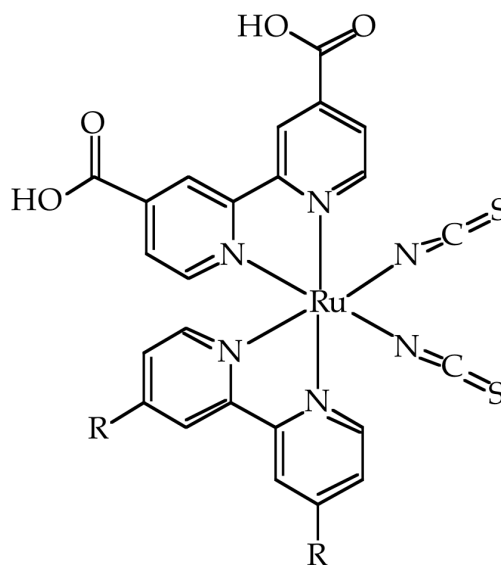| R	Abbreviation
$-CO_2H$	N3
$-CH_3$	$N3\_C_1$
$-CH_3,\ -C_9H_{10}$	$N3\_C_1C_9$
$-C_4H_9$	$N3\_C_4$
$-C_9H_{10}$	$N3\_C_9$
$-C_{12}H_{13}$	$N3\_C_{12}$

Figure 4.3: Hydrophobic dye structures with aliphatic chains of different length. All dyes were synthesised by Md. K. Nazeeruddin and S. M. Zakeeruddin.

---

[*] unpublished results

These hydrophobic dyes show the same absorption spectrum as the N3 dye in ethanol solution, but possess a 18 % lower molecular extinction coefficient.[*] Upon adsorption to the TiO_2 surface the dye spectra are blue shifted, with a maximum absorption around 505 nm, while the corresponding absorption maximum of the N3 and the N719 dye is about 515 nm. The kinetics of the dye adsorption have been found to alter slightly for the different dyes.[8] However, a typical time for dye uptake was 24 h which is long enough to achieve a equilibrium between dye adsorption and desorption.

Figure 4.4 summarises the photovoltaic parameters of SSD sensitised with the different hydrophobic sensitisers. A clear trend is observed, showing improved performance for increased chain length of the sensitiser. For comparison the results for the N3 are also shown, although they cannot directly be compared with the hydrophic dye series. The same is true for the N3_C4 as the organic side chain is a branched rather than linear.
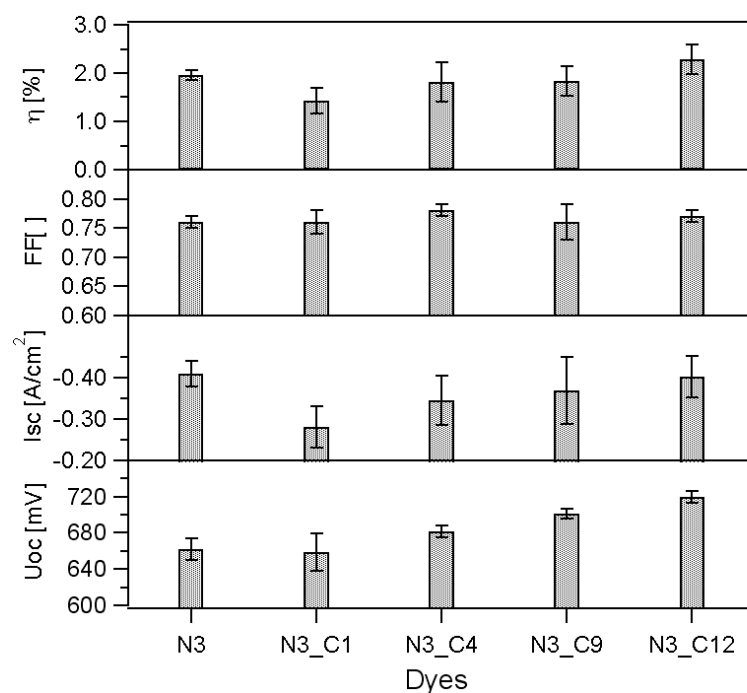

Figure 4.4: Comparison of the photovoltaic performance of SSD sensitised with the different hydrophobic dyes at 10 % Sun. The TiO_2 film thickness of the SSD was 2 μm and the hole conductor composition was 0.2 M in spiro-MeOTAD, 0.13 mM in $Li(CF_3SO_2)_2N$, 0.18 M in tBP and 0.76 mM in $N(p-C_6H_4Br)_3SbCl_6$. The composition of the hole conductor film will be discussed more in detail in chapter 5. Comparison at 10 % Sun has been chosen avoid problems of charge transport in the hole conductor (non-linear response behaviour).

---

[*] personal communication Md. K. Nazeeruddin

As photochemical and electrochemical properties of the members of the hydrophobic dye series are very similar, the structure of dye may play an important role in the formation of the heterojunction, as expected. In a similar study on the DSSC,[9] the improved performance of these devices was correlated with lower interfacial charge recombination as a result of a lateral interaction of the long chains of the sensitiser. The influence of the hydrophobic dyes on the recombination dynamics in the SSD has been studied employing nanosecond laser experiments. The differences in the recombination kinetics were rather small and did not exceed an order of magnitude.[8] However, the long chains are expected to shield the inorganic oxide surface, forming an organic environment which might be advantage for the filling of the pores with the organic holeconductor and therefore for the morphology of the heterojunction. The exact mechanism for the improved performance is not clear. Yet this experiment demonstrated that the dye structure can have an important effect on the interface.

4.2.5   <u>Deposition of the spiro-MeOTAD</u>

The samples were removed from the dye solution, washed in the same solvent which was used for the dye uptake and dried under an argon flow. 100 (150) µl of spin-coating solution were applied to the sample of large (small) sample geometry and a thin film was formed by rotating the sample at 1500 rpm for 30 s with an acceleration of 200 rpm. The samples were then dried in argon for 45 min and in vacuum for one hour at (0.1 mbar), before being transferred into a vacuum chamber to apply a thin gold contact layer via thermal evaporation.

Thickness of the Hole Conductor Film

In previous work the concentration of the spin coating solution was maximised to obtain a spacing layer between dye-sensitised heterojunction and the Au counter electrode. The highest solubility of 400 mg/ml was obtained with the solvent chlorobenzene. In other solvents of comparable physical properties, such as toluene or p-xylol, the solubility of spiro-MeOTAD was significantly lower. Spin coating using solvents with low boiling points such as THF yielded films with inhomogeneous thickness distribution.[10] Figure 4.5 shows the SEM cross-section of the solid-state dye-sensitised heterojunction with a spiro-MeOTAD film on top of the TiO_2.
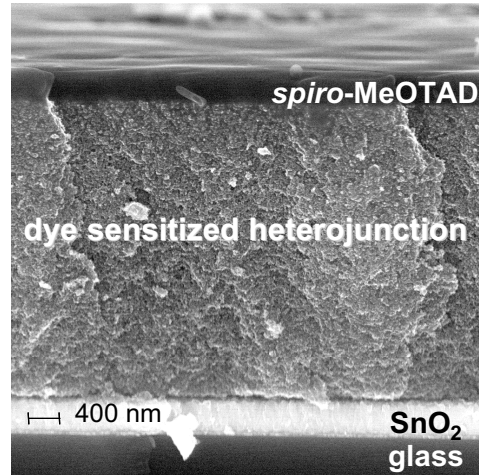
Figure 4.5: Scanning electron micrograph (SEM) showing the cross section of the solid-state dye-sensitised heterojunction between TiO_2 and spiro-MeOTAD.

It can be observed that the hole conductor forms a film on top of the TiO_2. In the SSD this film forms a barrier between the TiO_2 and the counter electrode. Assuming that the amorphous organic film can be treated like a bulk material in terms of the resistance R, i.e.:

$$R = \rho \cdot \frac{d}{a} \qquad (4.1)$$

(d=layer thickness, a=surface area, and ρ=specific resistance), the isolating film considerably increases the resistance of the device. In this respect the film on top of the TiO_2 should be as thin as possible, while still forming a pinhole free barrier layer. The thickness of organic film on top of the TiO_2 is depending on the spin coating parameters, such as spin coating speed and concentration of the spin coating solution. Figure 4.6 indicates the correlation between spin coating speed respectively concentration and layer thickness.

From the SEM cross section in Figure 4.5 a thickness of about 400 nm can be determined for the hole conductor film on top of the TiO_2, which has been prepared from a 0.2 M spin-coating solution. Assuming that the relation between concentration of spin coating solution and thickness is similar for the deposition of the hole conductor onto the nanocrystalline TiO_2, a reduction of the concentration of 50 % is expected to result in a film of about 200 nm on top of the nanocrystalline film. Photovoltaic experiments revealed no increased risk for short circuit currents in SSDs prepared from a spin coating solution containing 0.1M spiro-MeOTAD instead of 0.2 M. However, the SSD containing thinner organic spacer layers between TiO_2 and counter electrode performed more linearly in terms of varying light intensity.
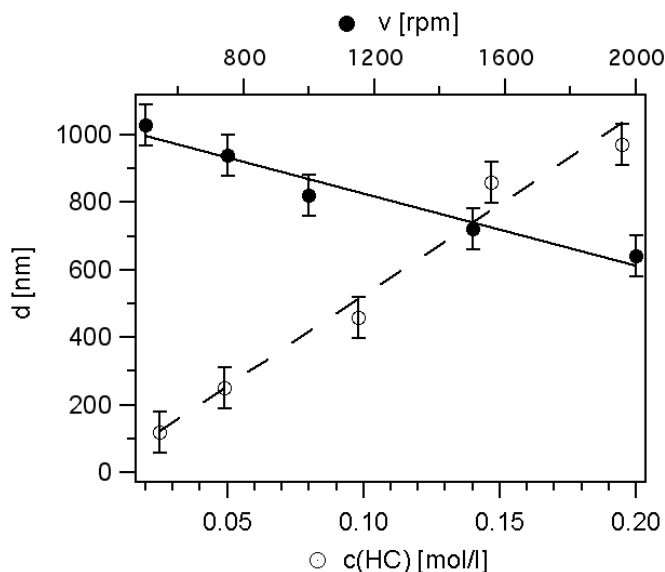
Figure 4.6: Relation between the spiro-MeOTAD concentration in the spin coating solution (○) respectively the spin coating (●) speed and the thickness of the resulting hole conductor film. The thickness of the dried film after spin coating on a bare glass substrate was determined by means of an alpha-step apparatus.

4.2.6   Deposition of the Counter Electrode

The metal contact electrode was deposited by thermal evaporation in UHV (5*10-6 mbar) using an Edwards evaporator (Vacotec Auto 560). Evaporation rates were 0.1–0.2 nm/s for the first 0.2 nm and 0.5–0.7 nm/s until the desired layer thickness was reached. The thickness of the layer was monitored by a quartz balance setup (FTM7 Film Thickness Monitor). A metal mask was used to define the contact areas on the sample.

Thicker gold layers are of advantage due to their higher reflectance and conductivity. Correspondingly best performance was observed for the thickest counter electrode in a device series with gold layers varying between 10 and 70 nm. The enhanced performance for thicker films was the result of increased short circuit currents. Devices with 60 nm gold film showed 22 % higher short circuit currents at 10 % Sun than devices with a 20 nm gold film. A 10 nm gold film is transparent, whereas a 20 nm is opaque. The deposition of thicker films requires longer evaporation times and thus longer thermal stress for the devices. Gold films of about 100 nm become mechanically instable and tend to peal off. Devices were therefore typically provided with a gold counter electrode of 30 nm.

4.2.7   <u>Sealing of Device</u>

Contrary to expectations at the early state of the development of the SSD it turned out that, as for most of the organic devices, sealing is necessary to maintain long-term stability devices and protect the active surface against mechanical stress. The devices have been sealed employing two techniques:

1.Encapsulation of the active area with Mylar 25 MC2 (DuPont) by thermal lamination. Mylar 25 is a one side metallised polyester film, overcoated on both sides with a heat sealable PVDC copolymer.

2.Coverage with a 2 mm glass sheet and sealing with a combination of the heat sealable Surlyn film and the epoxide Torr Seal[®] (Varian Vacuum Products) as shown in Figure 4.7. This encapsulation method is very similar to the one used for the electrolyte cell.
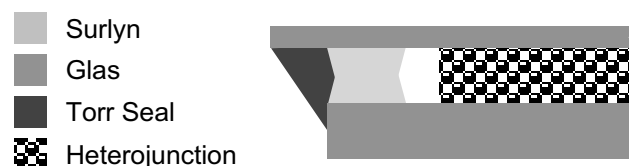

Surlyn
Glas
Torr Seal
Heterojunction

Figure 4.7: Illustration of sealing with Surlyn and Torr Seal.

The PVDC coating (Mylar 25 MC2) tend to lift off after a couple of days. The second sealing was mechanically stable over a long time and has been further tested immersing the device in a water bath. No water inleakage could be observed during a period of two hours. The sealing is therefore efficient in protecting the device against environmental conditions. Moisture included during device preparation, will be encapsulated as well. Hence it is important to exclude moisture and impurities during the cell preparation as much as possible.

4.3 Conclusions

- The SSD preparation described above includes:
     1. the structuring and cleaning of the TCO
     2. the deposition of the compact underlayer by spray pyrolysis
     3. the deposition of the nanocrystalline TiO_2 by screen-printing and the dye uptake
     4. the spin-coating of the hole conductor with following drying and
     5. the deposition of the counter electrode by thermal evaporation.

• The total preparation time is on average 35 h/device. Accordingly the preparation of the SSD is more time consuming than the preparation of the electrolyte cell. Compared to the electrolyte cell increased time demand is caused by the structuring of the glass, the deposition of the compact underlayer, the spin coating process and the time for the drying of the cell prior to the deposition of the counter electrode. In terms of an industrial application a drastic reduction of the preparation time is expected from automation of several deposition steps, similarly as it has been already established for the electrolyte cell. This includes in particular the automatic screen-printing. Further gain in preparation time as well as in precision is expected from substrate structuring using a laser instead of the chemical etching method. Time intensive steps such as the dye uptake and the drying after the hole conductor deposition can be accelerated by increasing the temperature of the dye solution respectively the drying chamber. The dye uptake from an ethanol solution at 80°C is already an established method, reducing the time for the dye uptake from several hours to 30 min. The drying of the hole conductor film at increased temperatures should be accompanied by studies of the morphology of the hole conducting film to avoid crystallisation of this material.

• The dye structure was found to play an important role in the formation of the heterojunction. A series of N3 type dyes, for which four carboxyl groups were exchanged by aliphatic chains of differing length, was studied in the SSD. A correlation of the photovoltaic performances with the chain length of the aliphatic chain was obtained. No significant influence of the chain length on the recombination dynamic was observed. The effect was thus rationalised in terms of an improved wettability of the long-chain dye sensitised TiO_2 by the organic hole conductor.

• The spiro-MeOTAD material that does not penetrate the pores of the TiO_2 forms an isolating organic film between TiO_2 and counter electrode. This film on top of the heterojunction is important to avoid short circuits, but it increases the resistance of the cell. The thickness of this spacer layer was optimised with respect of a functional spacer layer on the one hand, and low film resistance on the other hand. The thickness of the hole conductor was controlled via the spin coating parameters, in particularly the speed of the coating process and the concentration of the spin coating solution.

4.4 References

[1] C. Barbé, F. Arendse, P. Comte, et al. *J Am Ceram Soc* **1997**, *80*, 31557-71.

[2] N. Papageorgiou, C. Barbe and M. Grätzel. *J Phys Chem B* **1998**, *102*, 4156-4164.

[3] P. Hemenger. *Rev Sci Instrum* **1973**, *44*, 698.

[4] D. Schroder. Semiconductor material and device characterization, Wiley, 1990.

[5] A. Kay. Ph.D. Thesis, EPFL, 1994.

[6] L. Kavan and M. Grätzel. *Electrochim Acta* **1995**, *40*, 643.

[7] S. Goncalves-Conto, M. Carrard, L. Si-Ahmed, et al. *Adv Mat* **1999**, *11*, 112-115.

[8] M. Stalder, Travail Diplôme, EPFL, 2002.

[9] S. M. Zakeeruddin, M. K. Nazeeruddi, R. Humphry-Baker, et al. *Langmuir 18* **2002**, *18*, 952-954.

[10] J. Krüger. Diplomarbeit, Universität Heidelberg, 1998.

5 INTERFACIAL RECOMBINATION

CHEMICAL MODIFICATION OF THE HETEROJUNCTION

This chapter presents a variety of chemical modifications at the heterojunction of the SSD in order to inhibit interfacial charge recombination. The most promising approach was the blending of the hole-transporting medium with tert.-butylpyridine (tBP) and lithium ions. Nanosecond laser spectroscopy and photovoltaic characterisation measurements were used to study the impact of the additives on the SSD. Based on the introduction of these two additives into the spiro-MeOTAD medium and the optimalisation of device parameters, such as the TiO_2 layer thickness, the conversion efficiency could be enhanced up to 2.5 % at AM1.5.

5.1 Introduction

Charge carrier recombination is a major energy loss mechanism in dye-sensitised solar cells due to the close proximity of electrons and holes throughout the interpenetrating network and the lack of a suitable potential barrier at the interface. This is particularly the case for the solid-state solar cell, due to the missing charge screening as in the case of an electrolyte hole transporting material. The recombination reaction rate manifests itself in a decreased electron diffusion length in the TiO_2, which, contrary to the conventional pn junction solar cell, is not a material constant in dye-sensitised solar cells. Three recombination processes have to be considered which are of different importance for the function of the cell.

1. *Recombination of the photo injected electron with the oxidised dye* before the dye can be regenerated. This reaction, which has been studied in some detail,[1-3] is a remarkably slow process at short circuit (μs to ms), at least for the dyes used in the present work, and thus does not limit the short-circuit photocurrent. The rate of this reaction increases as the potential of the substrate electrode becomes more negative, i.e. as the cell voltage changes from short circuit (0 V) to its open-circuit photovoltage.[4] At open circuit, all the photo injected electrons recombine by one mechanism or another.

2. *The recombination of an electron in the SnO$_2$ substrate with the oxidised redox species*. This pathway is negligible as the compact TiO$_2$ layer between TCO and dye-sensitised TiO$_2$ network blocks the direct contact between TCO and hole conductor. The blocking character of this compact underlayer is obvious from dark current measurements of TCO/compact TiO$_2$/spiro-MeOTAD/Au devices of this compact underlayer A detailed study of the blocking behaviour of the compact layer in the electrolyte cell using time resolved techniques and the charge extraction method[5] has been carried out by Cameron.[6]

3. *The recombination of an electron in the TiO$_2$ with the oxidised redox species* is the main process diminishing the charge separation in the SSD. The charge recombination manifests itself in an enhanced dark current, which significantly reduces the maximum cell voltage obtainable. This interfacial recombination has been shown to be controlled by electron trapping in surface states.[3,7-9] A surface state is an intra band gap electronic level that arises from incomplete coordination of the atoms present at the interface by other lattice atoms resulting in dangling bonds or coordinatively unsaturated sites. The large surface area of the mesoporous TiO$_2$ gives rise to a large number of defect states at the heterojunction and at grain boundaries. The surface states have been studied by means of electrochemical spectroscopic methods[10-12] as well as transient photocurrent response[2] and have been assigned to Ti^{4+} surface sites. For the modelling of the charge transport an exponential distribution of traps below the conduction band[13-15] is often used. The occupancy of the surface states is a function of the Fermi-level and therefore also on the applied potential and/or the number of injected electrons. The interfacial recombination kinetics have been shown to increase with the application of a negative bias to the TiO$_2$ as well as for increasing incident light intensities.[3] On the other hand shifts in the conduction band due to intercalation or surface binding of potential determining ions, such as lithium, lead to increased occupancies in the case of a constant applied potential.

5.2 Strategies to Inhibit Interfacial Charge Recombination

Interface engineering seems to be a more promising strategy to improve device performance rather than investing in research of new semiconductor materials, as recombination processes in dye-sensitised solar cells take place mainly at the interface rather than in the bulk. In this respect several techniques have been developed for the DSSC and for similar organic devices such as OLEDs and electrochromic devices. Making use of the experience gained in these studies, different approaches to inhibit interfacial recombination have been studied for the application in SSDs.

5.2.1   <u>Interface Dipole</u>

For organic LEDs, barrier heights at the interface between organic semiconductors and metals could be successfully decreased by the introduction of an additional interface layer. Typical examples for these surface layers are LiF or organic self-assembling molecules.[16-18] The beneficial effect of this interface layer has been assigned to the formation of dipole fields diminishing the workfunction difference of the semiconductor materials, thereby decreasing charge injection barriers. However, the consequences of an interfacial dipole field can also be exploited to increase the barrier for charge transfer, as it is needed to suppress the dark current in the solar cell. This approach was demonstrated by the chemical modification of the heterojunction between TiO_2 and *spiro*-MeOTAD with a series of benzoic acids with different dipole moments.[19] A clear correlation has been found between the dipole moment of the modifying molecule and the dark current of the modified interface. Based on these results 1-methyl-4-phosphonatopropyl-1,4-diaza-bicyclo[2.2.2]octane was designed. In this dipole molecule, the phosphonate acts as attachment group, which is forming a strong bond between the TiO_2 surface and the metylbicyclo[2.2.2]octane groups. As a strong electron withdrawing group it provides the molecule with a high dipole moment.[*] Preliminary experiments were very promising: The work function of the with the dipole molecule modified TiO_2 was decreased by 500 mV and nanosecond laser experiments showed a slow down of the charge transfer from the TiO_2 to the hole conductor by one order of magnitude. However, the photovoltaic characterisation of a SSD, where the dipole molecule was co-adsorbed with the dye molecule, showed sigmoidal curves of high series resistance. This behaviour has been attributed to the poor wettability of the with the dipole molecule modified TiO_2. Furthermore the dipole field might not only impede the electron transport from the TiO_2 to the holeconductor but also the electron injection by the dye. Accordingly a better strategy seems to be the interface passivation with neutral molecules.

5.2.2   <u>Interface Separation Layer</u>

The sensitising dye cannot cover the entire TiO_2 surface, and the uncovered areas are potential sites for interfacial recombination. A method that will cover the exposed oxide surfaces with an ultra thin, electrically insulating film should substantially decrease the recombination rate by physically preventing the close approach of hole conductor cation to the TiO_2. Coatings applied on top of the already dye-functionalised film will provoke a high

---

[*] Using the software Cache and Mac Spartan plus a dipole moment of 38.6 D respectively 40 D was determined.

risk of chemically modifying the dye or if the insulating film becomes too thick, render the dye inactive. In a study on recombination kinetics in the DSSC, Gregg et al.[20] used thin films of poly(methylsiloxane), prepared by vapour-phase reaction of exposed TiO_2 surfaces with CH_3SiCl_3 which leads to a marked decrease in the rate of interfacial charge recombination.

Another very promising approach to reduce the interfacial recombination in the electrolyte cell is to coat the nanocrystalline TiO_2 with a thin layer of another metal oxide film with a higher conduction band edge. This surface coating is increasing the physical separation of injected electrons and the oxidised dye / redox couple, which is retarding the recombination reaction. Significantly improved device performances have been reported for coatings of $ZnO^{[21]}$ and $MgO^{[22]}$ on SnO_2 and of $Nb_2O_5^{[23,24]}$ and $Al_2O_3^{[25,26]}$ on TiO_2. The conduction band edge of the surface coating materials is negative of both the conduction band edge of the TiO_2 and the dye excited state oxidation potential, which makes the mentioned materials efficient barrier materials for electron injection and charge recombination reactions.

This strategy was tested for SSD in the form of Nb_2O_5 and ZrO_2 overcoating layers which were prepared by dip-coating of a standard TiO_2 layer in the corresponding organic precursors $Nb(OC_3H_7)_5$ and $Zr(OC_3H_7)_4$. The samples with the ZrO_2 sample showed 17 % higher IPCE values compared with the reference device without overcoating. However, the modified device was highly non-linear, showing diminished device performance for higher light intensities. This behaviour might be due to a decreased filling of the dye-sensitised TiO_2 pores with hole conductor upon deposition of another surface coating. This assumption is based on BET measurements of comparable TiO_2 over layers showing increasing surface area and decreasing pore size upon deposition of thin oxide surface film.[*]

5.2.3 Charge Screening

In the DSSC the electrolyte completely penetrates the porous TiO_2 network. Any electric fields, including those caused by photo injected electrons will be neutralised over very short distances by migrating ions. Therefore, under normal operating conditions, there should be essentially no macroscopic electric fields within a range of about 20-50 nm[27] in the TiO_2 film, depending on the electrolyte concentration and composition. Accordingly, during steady state illumination, the injected electrons will experience little or no electric field, so that their motion will be governed primarily by concentration gradients; that is, it will be diffusional. Since there are essentially no electric fields present in the dark, a transient electric field (image force) will be created by the photoinjection process upon illumination. The photoinduced field will oppose further charge separation and promote charge recombination.

[*] Personnel communication P. Comte

These field-induced recombination process are expected to be mitigated by the presence of mobile ions in the film, which can rearrange and screen photoinduced electrostatic fields. In the SSD these local fields are expected to play a major role in acceleration of charge recombination, since the pore filling is less perfect and charge carriers in the solid hole-transporting medium are less mobile than in the electrolyte. The presence of mobile ions is essential for the working process of the SSD as has been shown by comparison of SSD with and without lithium ions in the hole conducting matrix.[28] SSD without lithium showed IPCE of 5 %, whereas SSD with lithium yielded IPCE of 33 %. The beneficial effect of lithium ions has been correlated with its high mobility in organic amorphous media[29] and its capability to intercalate into the TiO_2 network.[30]

Different salts have been tested for the charge screening at the interface in the SSD, varying the cation on the one hand and the anion on the other hand. Photovoltaic experiments revealed $Li(CF_3SO_2)_2N$ (LiTFSA) as the most effective salt for the application in the SSD. Compared to the application of the lithium salt directly to the spin-coating solution of the hole conductor, an important loss in device performance was found when treating the dye-sensitised TiO_2 with the lithium solution prior to hole conductor deposition. This indicates that lithium ions play an important role for the charge separation not only at the interface but also inside the hole-transporting medium. Most of the compounds studied, in particular salts of sodium and magnesium, but also organic molecules such as crown ethers, hindered the film formation of the organic amorphous film. The corresponding SSD showed distorted current-voltage characteristics due to high resistive losses.

Beside its screening effect, lithium ions, particularly in aprotic solvents, are influencing the flat band potential of the TiO_2 and with this the driving force for electron injection.[31] The consequence of this band shift in the presence of lithium in the electrolyte of DSSCs is an enhanced photocurrent and a diminished photovoltage.[32] In SSD the charge neutralisation effect of lithium ions is more important than the influence on the TiO_2 band energetics, as no loss of photo potential was observed upon application of lithium. The change of the device performance for varying lithium ion concentrations in the hole conductor matrix will be demonstrated in more detail in the following discussion.

5.2.4   Modulation of Surface Trap Occupancy

Chemically surface states can be correlated with Lewis acids that readily form complexes with electron donating compounds. Such a surface complex can result in a large shift of the redox level for the Ti(IV)/Ti(III) electronic state from the band gap into the conduction band, in which case trapping of electrons can no longer occur.[33] The suppression of back electron

transfer in DSSC by application of 4-*tert*butylpyridine (tBP) to the electrolyte has been explained by such a passivation of recombination centers below the conduction band edge.[34] A more detailed explanation for the beneficial effect of tBP on the device performance is the shift of the conduction band/trap state energetics caused by the proton scavenging character of tBP.[35] The adsorption of strong Lewis basis is furthermore expected to alter the spatial overlap of the donor and acceptor wave functions for the back electron transfer as well as the reorganisation energy λ for the reaction of the trapped electrons.[36] Based on these models a selection of bases has been screened by Kelvin probe and photovoltaic measurements for their utility in the SSD as a recombination inhibiting agent.

Effect of Bases on the band Energetics of TiO$_2$

The effect of the base on the TiO$_2$ has been determined via the change of the TiO$_2$ work function, which has been measured by means of the Kelvin Probe technique. The work function of a semiconductor is defined as the energy difference between the vacuum level and Fermi level. A change of the work function $\Delta\Phi$ is either due to a change in the electron affinity $\Delta\chi$, the band bending V_{bb} or a combination of both. The contact potential difference after modification is therefore given by:

$$CPD = \left(\Phi_{bS} - \Phi_P\right) - \left(\Phi_{aS} - \Phi_P\right) = \Delta\Phi = \Delta\chi + \Delta\left(q \bullet V_{bb}\right) \tag{5.1}$$

where the index b stands for before, a for after modification, S for sample and P for probe (gold grid). Hence $\Delta\Phi$ is expected to reflect a modification of the Fermi level due to change of the occupancy of surface states as well as a modification of the band bending by the base.

Table 5.1 compares the differences in contact potential difference for TiO$_2$ layers before and after treatment with a base solution in acetonitrile. For the first measurement the remaining solution on the TiO$_2$ surface was only dabbed of and the samples was dried in Ar (Δ_1CPD). For the second measurement the samples have additionally been rinsed with dry acetonitrile(Δ_2CPD). Precautions have been taken to exclude environmental influences for this experiment. The change of the CPD value after rinsing is expected to indicate the stability of the adsorption to the TiO$_2$ surface. For all samples, a negative ΔCPD has been obtained upon base modification. The shifts in CPD do not scale with the pK$_b$ of the base, which indicates that the deprotonation is not the only reaction taking place at the surface of the TiO$_2$. A significant change of the CPD after additional rinsing has been observed for the phthalazine, DABCO and the piperazine, which might be assigned to a weak interaction of the base with the TiO$_2$ surface. It is striking that the proton sponge shows only a minor influence on the workfunction although it is a very strong base. Considering the steric demanding environment of the nitrogens in the proton sponge molecule a coordination of

the molecule to the surface is unlikely. The effect of this molecule is thus expected to be the result of the deprotonation of the TiO_2 surface only.

Additive	pK_b	Δ_1CPD [mV]	Δ_2CPD [mV]
Phthalazine	3.5	-490	-100
tBP	5.2	-98	-100
DABCO	8.6	-317	-90
Piperazine	9.8	-407	-340
DBU	11.6	-498	-560
Proton sponge	16.3	-95	-50

Table 5.1: Contact potential difference between non-modified TiO_2 surface and TiO_2 surface treated with different bases. Treatment has been performed by immersing the TiO_2 layer for 24 h in a 1 mM solution of the corresponding base in acetonitrile. Δ_1CPD corresponds to the measurement of the only dried samples (Ar). Δ_2CPD has been measured after rinsing the samples three times with acetonitrile. The whole experiment has been performed inside a glove box. Prior to molecule adsorption the TiO_2 films have been heated for 20 min at 450 °C in Ar atmosphere and were directly transferred to the glove box to cool down in Ar atmosphere. The given values present the average of the measurements of 5 samples per base. The average measurement error for the CPD values is ± 50 mV. For the molecule names and structures compare the list of abbreviations respectively the abstract A.1.3.

Effect of Bases on the SSD

For the application of the bases as additives in the SSD, the chemical consequences of their introduction into the SSD network has to be considered. To establish a modification of the interface between the hole conductor and the TiO_2 two approaches can be envisaged:

⇒ A *pre-treatment* of the nanocrystalline TiO_2 prior to deposition of the hole conductor solution by adsorption of the base from solution (typically acetonitrile) and

⇒ the direct application of the molecule to the spin-coating solution (*co-modification*).

Bases that did not show a stable CPD value upon rinsing might be dissolved from the surface during the spin-coating process and should therefore be used for co-modification. However several complications were encountered for the co-modification technique:

1. low solubility in spin-coating solution and crystallisation upon drying of spin-coated film

2. desorption of dye from TiO_2 surface (also complication with pre-modification)

3. quenching of hole conductor radical cation. Immediate disappearance of the oxidised form of spiro-MeOTAD in presence of bases with a pK_b over 6.

Figure 5.1 illustrates different levels of deformation of current-voltage characteristics due to modification of the hole conductor or the dye-sensitised TiO_2 surface with a base. High series resistance of several $k\Omega$ inhibit the formation of a plateau in the typical voltage region, particularly for high light intensities (Figure 5.1(a)). For some treatments, especially for the pre-treatment, sigmoidal curves were obtained (Figure 5.1(b),(c)). This type of current-voltage characteristic might indicate another rectifying process in series with the photon-to-electron conversion process and might result from the loss in ohmic character of the contact with the counter electrode in presence of base.
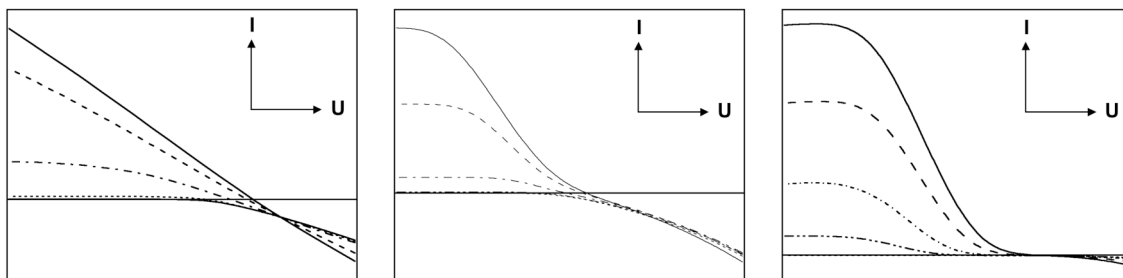

Figure 5.1: Illustration of distorted current-voltage characteristics resulting from the chemical modification of the heterojunction. The left graph corresponds to the pBP-modified sample, the middle one to the pre-tBP modified device, and the right on to the one treated with phthalazine (I=current and U=potential). The conditions of device preparation are given in the caption for Table 5.2.

Consequently, most of the bases that have a pronounced effect on the TiO_2 band energetics are not applicable in the SSD. Table 5.2 demonstrates the influence of a selection of bases on the performance of the SSD. For technical reasons not all samples could be measured in one series. To avoid differences due to device preparation conditions[*] only the differences relative to the reference sample of each series are given.

Except for the *pre*-PVP and the *pre*-tBP (vapour) modification all devices showed improved I_{SC} compared to the reference device without base treatment. This result is interesting regarding the effect of tBP on the performance of the DSSC. Typically tBP provokes an increase in U_{OC} and a decrease in I_{SC}, which has been attributed to the flat band determining properties of tBP. Striking is also the variation between the different tBP treatments with the best results for the co-tBP treatment. The negative result for the pre-tBP (solution) is assumed to be the result of a partial desorption of the dye from the surface,

---

[*] Changes in dye or colloid batch have been found to introduce a significant difference when comparing two series of SSD of otherwise equivalent preparation. Another incertitude is due to the high viscosity of the hole conductor solution, which is correlated to an error of about 10 % for the measured volumes.

which was not observed for other treatments. Despite the discussed complications the co-modification showed better results and higher reproducibility. U_{OC} values were on average only 20 % higher than for the unmodified case; I_{SC} values were only marginally higher than without tBP.[*] Beside a potential dissolution of the base upon deposition of the hole conductor this behaviour can be rationalised in terms of an influence of the base not only on the TiO_2/HC interface but also on the charge transport inside the hole conducting medium respectively at the interface HC/gold. This issue will be addressed in the following section.

Additive	ΔI_{SC} [%]	ΔU_{OC} [%]	$\Delta\eta$ (10 % Sun) [%]
co-4-phenylimidazole	43.5	-39.6	-20.35
co-phthalazine	46.7	61.4	27.95
co-PVP	43.8	83	35.05
pre-PVP	-50	+285	-0.14
co-pBP	49.9	0.9	25.2
pre-tBP(solution)	28	-15	-7.3
pre-tBP(liquid)	49.5	20.3	11.85
pre-tBP (vapor)	0	83	35.05
co-tBP	**50**	**16.4**	**56.25**

Table 5.2: Performance of SSD modified with different bases. Modification was established either via surface treatment of the dye-sensitised film prior to spin-coating of the hole conductor solution (prefix: *pre*) or by adding base to the spin-coating solution (prefix: *co,* c=0.15 M). The hole conductor matrix was 0.1 mM in $Li(CF_3SO_2)_2N$ and 0.2 mM in $N(p-C_6H_4Br)_3SbCl_6$.The devices were highly non-linear, showing much lower currents for high light efficiencies, To avoid limitation of charge transport, device comparison was established at 10 % Sun.

Table 5.2 shows the photovoltaic parameters at 10 % Sun, since all devices were highly non-linear and the photovoltaic output was charge transport limited rather than recombination-limited. Thus at high light intensities only a small or no improvement at all could be obtained for the modified devices. For the co-tBP sample a significant improvement in device performance could also be measured for higher light intensities. Accordingly the application of tBP to the hole conductor matrix has been studied more in detail, in particular in terms of its interaction with the other additives.

The influence of the deprotonation of the dye, i.e. the transformation of N719 into N712 upon base treatment is expected to be negligible, as similar experiments with N3_C9 instead of N719 lead to the same conclusions.

---

[*] The given averaged values (at 10% Sun) are based on all measurements, not only on the data presented in Table 5.2.

5.3 The Influence of Lithium Ions and tBP on the SSD

The discussion of the different strategies to inhibit interfacial charge recombination revealed the modification of the hole conductor matrix with tBP as the most promising approach to improve the device performance. The application of lithium ions was found to be essential for the device function. The direct introduction of the tBP into the hole conductor solution changes the dielectric properties of this solution and allows higher amounts of lithium salt to be dissolved. The tBP is expected to assist the dissolution of the lithium ions as a result of the interaction of lithium ions with the amine function of the tBP. The interaction of these two additives and their influence on the electronic processes in the SSD was investigated by photovoltaic and nanosecond laser experiments.

5.3.1 Photovoltaic Characterisation of Modified Devices

A series of solid-state devices with varying quantities of lithium salt and tBP in the spin-coating solution were compared in terms of their influence on photovoltaic parameters. Table 5.3 compares the photovoltaic output for varying LiTFSA concentrations and Table 5.4 the variations for increasing tBP concentration.

Increasing the concentration of lithium ions in the spiro-MeOTAD results in clearly enhanced short circuit currents and open circuit voltages for low light intensities (10 % Sun). However, the devices show non-linear behaviour in short circuit current for higher light intensities. The significant lower fill factor at 1Sun compared to 10 % Sun indicates that the charge transport is the limiting factor at high light intensity.

$c(Li[CF_3SO_2]_2N$ [mmol/l]	10 % Sun			
	I_{SC} [mA/cm^2]	U_{OC} [mV]	FF [%]	η [%]
13	0.335 ± 0.09	660 ± 12.0	0.66 ± 0.07	1.62 ± 0.23
26	0.362 ± 0.06	684 ± 8.60	0.77 ± 0.05	2.10 ± 0.08
39	0.389 ± 0.04	701 ± 1.69	0.77 ± 0.06	2.43± 0.04
$c(Li[CF_3SO_2]_2N$ [mmol/l]	100 % Sun			
	I_{SC} [mA/cm^2]	U_{OC} [mV]	FF [%]	η [%]
13	1.43 ± 0.45	677 ± 12.10	0.56 ± 0.03	0.61 ± 0.11
26	2.84 ± 0.23	711 ± 10.60	0.55 ± 0.06	1.23 ± 0.17
39	3.50 ± 39.04	761 ± 6.23	0.58 ± 0.06	1.70 ± 0.04

Table 5.3: Change in device performance at 10 % Sun and 100 % Sun light intensity for varying LiTFSA concentration. To allow larger quantities of lithium salt to be dissolved tBP was also added in a concentration of 0.07 mol/l in the spin-coating solution.

c(tBP) [mol/l]	10 % Sun			
	I_{SC} [mA/cm^2]	U_{OC} [mV]	FF [%]	η [%]
0.07	0.409 ± 0.04	663± 6.5	0.70 ± 0.03	2.00 ± 0.08
0.10	0.412 ± 0.04	711 ± 2.9	0.66 ± 0.01	2.05 ± 0.19
0.17	0.384 ± 0.12	734 ± 10.3	0.65 ± 0.10	1.89 ± 0.43
c(tBP) [mol/l]	100 % Sun			
	I_{SC} [mA/cm^2]	U_{OC} [mV]	FF [%]	η [%]
0.07	4.2 ± 0.16	719 ± 9.32	0.33 ± 0.03	1.09 ± 0.11
0.10	3.61 ± 0.31	773 ± 5.62	0.32 ± 0.03	0.94 ± 0.02
0.17	1.2 ± 0.23	857 ± 0.61	0.56 ± 0.02	0.58 ± 0.09

Table 5.4: Change in device performance at 10 % Sun and 100 % Sun light intensity for varying tBP concentration. The concentration of LiTFSA was for all samples 10 mmol/l.

The comparison of SSD containing different quantities of tBP reveals a pronounced effect of this additive on the open circuit potential. While the U_{OC} is increasing for increasing tBP concentrations for low and high light intensity, the tendency for the short circuit current is nearly the opposite. For low light intensities the I_{SC} shows a maximum value for intermediate tBP concentrations and drops again for further increase in tBP concentration. For high light intensities I_{SC} is decreasing for increasing tBP concentration. Remarkable is also the drop of the fill factor for high light intensities in presence of tBP. Only for the highest tBP concentration the IV curve has again a square like behaviour as a result of the high U_{OC}. The low fill factors are the result of a distortion for potentials near and greater than the potential of the maximum power point. Figure 5.2(a) shows typical IV curves for different light intensities in the presence of tBP. Distortions of current voltage characteristics are often the result of scan rates that are too fast to allow system equilibration and thus quasi-steady-state conditions. One of the device features responsible for this distortion is the voltage-dependent diffusion capacitance, which is exponentially dependent on the bias voltage and linearly dependent on the light intensity.[37] In the present case however the distortion phenomenon occurs also at very low scan rates. The corresponding current dynamics (Figure 5.2(b)) imply that the distortion is the result of a charging process at the heterojunction. The charge transport in the hole conductor cannot keep up with the charge generation, leading to the build-up of an electric field at the interface, which favours the interfacial charge recombination. For potentials smaller than the potential of the maximum power point the dark current becomes more important lowering the measured photocurrent.
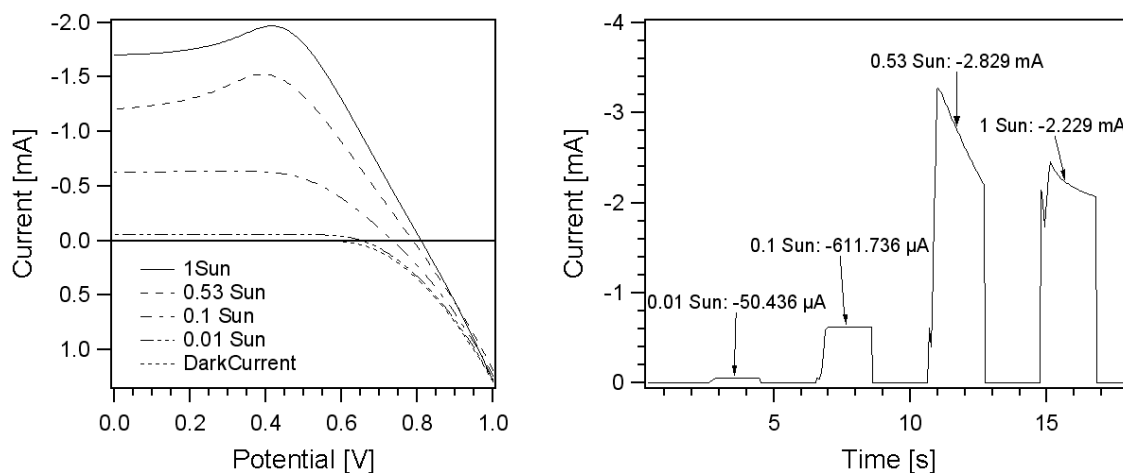
Figure 5.2: Current-voltage characteristics (a) and corresponding current dynamic measurements (b) demonstrating the overshoot problem in presence of tBP in the hole conductor film .

It is striking that this feature is only observed in presence of tBP and not for unmodified cells. One explanation is the blocking of the recombination by the tBP, which allows the build up of an electric field. In the unmodified case this charge is lost by interfacial recombination. Furthermore, the fitting of the dark currents of the SSD showed a doubling of the series resistance in the presence of tBP indicating less efficient charge transport in the presence of tBP. The effect was found to diminish or to completely disappear when increasing the lithium salt concentration and/or after long periods of illumination. The effect was also less important for devices based on TiO_2 layers thinner than 2 μm.

In order to find the reason for the increased resistance in the hole conductor, spectroscopic long-term studies were performed with the hole conductor spin-coating solution. As discussed above, the application of bases with high pK_b values lead to the quenching of the hole conductor radical cation. Upon application of the tBP, no colour changes, diagnostic for the degradation of the radical cation, were observed. However, long-term studies of doped spiro-MeOTAD solution containing tBP showed that a slow decrease of the doping level is occurring in the presence of the tBP. In contrast the introduction of tBP into a solution of spiro-MeOTAD^{2+}(PF$_6$)$_2$ or a spiro-MeOTAD solution, doped with NOBF$_4$, provoked the immediate disappearing of the typical red colour of the radical cation. The stability of the hole conductor cation in presence of the [N(p-C$_6$H$_4$Br)][SbCl$_6$] might be explained by the weak oxidising properties of the [SbCl$_6$]⁻ complex.[*] Similarly [N(p-

---

[*] The oxidising power of the [SbCl$_6$] anion has been shown to be sufficient to effect iodide oxidation.[38]

$C_6H_4Br)][SbCl_6]$ is more stable than $[N(p-C_6H_4Br)]$ $[BF_4]$ due to re-oxidation of neutral amine by the $[SbCl_6]$ anion.[39,40]

Since the hole conductor solution is normally prepared directly before the spin-coating, losses of the radical cation in the solution are expected to be around 10-20 %. The reaction is retarded in the solid state. The adsorption of tBP respectively pyridine on metal oxides has been studied in detail by FTIR, since pyridine serves as an analytical tool to detect surface states acting as Lewis acids.[41-43] From this study it is known that pyridine can bind physically or chemically via the nitrogen to the oxide surface. While the physical coordination is rather weak and will not stand higher temperatures, the chemical coordination of the pyridine shows high temperature stability.[44] tBP molecules that are not chemically fixed will evaporate during the drying of the organic film in the UHV. Thus, depending on the preparation time, temperature and the vacuum used for the drying process the tBP concentration in the hole conductor film will decrease while leaving an self-assembled tBP at the TiO_2 surface. Accordingly the final doping level of the hole conductor is dependent on the preparation conditions, but will be lower than in the SSD without tBP.

The overshoot issue could be solved by applying higher lithium salt concentrations relative to that of tBP in the hole conductor and by thinning of the hole conductor film thickness between the dye-sensitised heterojunction and the counter electrode. Figure 5.3 illustrates the influence of tBP (co-modification) on current-voltage characteristics and the IPCE of the SSD. The concentrations of the two additives TFSA and tBP were chosen considering the trends observed for varying the TFSA and tBP concentrations in the spin-coating solution (Table 5.3, Table 5.4). Comparison of the two devices reveals an increase in excess of 100 % in U_{OC} and of 26 % in the I_{SC} for the tBP-treated electrode. The overall efficiency for the tBP treated device was 2.5 % at AM 1.5. The higher I_{SC} for the co-modified cell is also reflected in higher peak values for the corresponding IPCE (Figure 5.3(b)).

An equivalent device based on the same hole conductor composition, but employing the large device geometry (compare chapter 4), was sent to the National Renewable Energy Laboratories (NREL), USA[*] for certification by independent device characterisation. The performance determined at the EPFL and presented in Figure 5.3(a) was confirmed by NREL. The original measuring report is given in the Appendix A.1.3. The corresponding device was encapsulated and equipped with an UV-filter.

---

[*] NREL device characterisations: http://www.nrel.gov/measurements/device.html
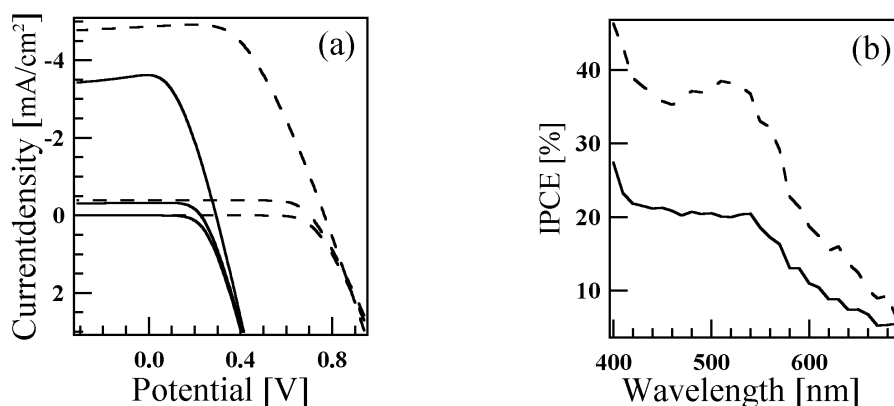
Figure 5.3: (a) Current-voltage characteristics in the dark and at an illumination intensity of 1/10 Sun and 1 Sun (corresponding to global AM1.5 10 mW/cm^2 and 100 mW/cm^2) in presence (dashed line) and absence (solid line) of tBP in the hole conductor matrix. (b) IPCE of solid-state dye-sensitised solar cells in presence (dashed line) and absence (solid line) of tBP in the hole conductor matrix. The spin-coating solution for the deposition of the hole conductor contained 0.15 M spiro-MeOTAD 0.26 mM in Li(CF$_3$SO$_2$)$_2$N, 0.11 M in tBP, and 0.4 mM in N(p-C$_6$H$_4$ Br)$_3$SbCl$_6$. An active electrode area of 0.16 cm^2 has been defined by a black mask.

The influences of lithium ions and tBP in the SSD are different compared to the corresponding data reported for the DSSC. In the DSSC increasing lithium ion concentration in the electrolyte provokes increasing I$_{SC}$ and decreasing U$_{OC}$ while increasing tBP leads to higher U$_{OC}$ and lower I$_{SC}$. The opposed characteristics of these additives were rationalised in terms of their influence on the energetics of the conduction band/ trap states and therefore on the kinetics of charge recombination: While lithium causes a band edge shift away from the vacuum level, tBP provokes a band edge shift in the other direction by deprotonation of the TiO$_2$ surface.[3,31,35] In the case of the SSD the increased U$_{OC}$ for higher lithium concentrations indicate that the charge screening effect in presence of lithium ions should be more important than the induced band edge shift. This effect will be studied more in detail by transient laser experiments.

5.3.2 Kinetics of Interfacial Charge Recombination

The influence of the additives in the hole conductor solution on the recombination dynamics in the SSD was studied using nanosecond transient absorption spectroscopy. The pulsed laser intensity was adjusted to a low energy of 0.04 mJ/cm^2 to ensure excitation of ≤1 excited molecule/nanoparticle. The dependence of the recombination kinetics on the excitation energy has been discussed in more detail in chapter 3 (Experimental methods). The use of low energy densities for excitation and observation light resulted in decay curves,

which can be fitted to a first order kinetic. However, the drawback of these low energy measurements and an observation wavelength of 1000 nm is the low signal-to-noise-ratio.
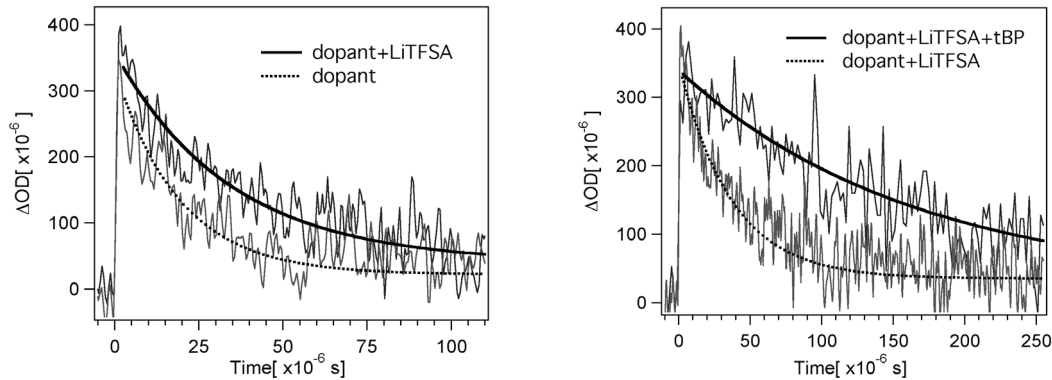

Figure 5.4: Dependence of the transient absorption decay kinetics of the hole conductor cation for different hole conductor compositions. Left graph: influence of lithium (15 mM in spin coating solution) for doped sample (0.2 mM N(p-C_6H_4 Br)$_3$SbCl$_6$ in spin coating solution). Right graph influence of tBP (0.2 M) for a sample containing dopant and LiTFSA (15 mM and 0.2 mM N(p-C_6H_4 Br)$_3$SbCl$_6$ in spin coating solution).

Figure 5.4 illustrates the influence of lithium ions in the hole conductor matrix and the effect of the additional application of tBP. For a hole conductor matrix prepared from a spin-coating solution, containing 10 mM LiTFSA, the change in recombination rate compared to the reference sample without lithium ions is rather small(Figure 5.4(a)). Much more pronounced is the supplementary application of tBP to the hole-transporting medium. In the presence of tBP only ca. 50 % of the signal has decayed within 100 μs, whereas in the absence of tBP the decay of the signal is complete at this time. Moreover the presence of the tBP allows higher lithium salt concentrations in the organic spin-coating solution, which leads to more important changes in the recombination dynamics of the corresponding devices. As indicated in Table 5.5 the recombination rate is decreased by 56 % when using 50 mM LiTFSA instead of 15 mM. Further increase in lithium salt concentration does not provoke any significant change in the electron dynamics.

c(LiTFSA) [mM]	k_r [s^{-1}]
15	1858
50	819
125	696

Table 5.5: Single exponential time constants for different concentrations of LiTFSA in the spin-coating solution. To enable the dissolution of high amounts of lithium salt, 0.2 M tBP were added to the spin-coating solution.

Figure 5.5 illustrates the influence of the dopant on the recombination kinetics. A clear acceleration of the recombination is observed for the doped spiro-MeOTAD. The strong dependence of the recombination dynamics on the concentration of the radical cation raises the question, whether the slowdown of the recombination in presence of the tBP is due to the decrease of the doping level. Figure 5.5. shows however that there is still a significant difference between a sample containing all three additives and one with lithium salt and tBP only.
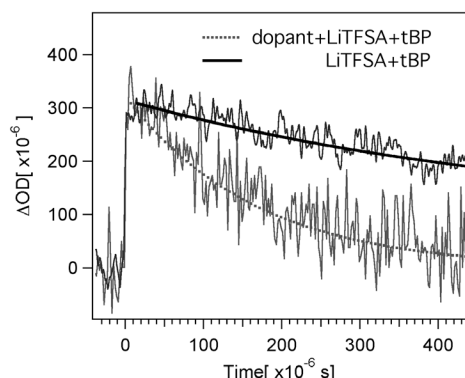
Figure 5.5: Dependence of the transient absorption decay kinetics of the hole conductor cation on the doping (15 mM, 0.2 M tBP and 0.2 mM $N(p-C_6H_4\ Br)_3SbCl_6$ in spin coating solution).

Increase of the excitation energy to 1mJ/cm^2 lead to an increase of the recombination kinetics for all samples and a transformation from single exponential kinetics to bi-exponential kinetics. However, the trends for the different hole conductor compositions discussed so far, remain the same for excitation of more than one dye molecule per nanoparticle.

Sample	k_{r1} [s^{-1}]	k_{r2} [s^{-1}]
dopant	52453	68489
dopant+LiTFSA	30508	**100720**
dopant+LiTFSA+tBP	4917	6519

Table 5.6: Comparison of recombination kinetics for aged samples

Table 5.6 compares kinetics for are freshly prepared device and a device aged under illumination. Significant increase in recombination dynamics is obtained for samples containing lithium ions but no tBP. Illumination experiments with spiro-MeOTAD solutions containing LiTFSA showed photodoping of the hole conductor for wavelengths under 410 nm, which coincides with the absorption spectrum of the hole conductor (see spectrum of spiro-MeOTAD in the Appendix A.1.1). The photodoping is clearly coupled with the lithium

ion, while the counter ion and solvent do not change the photodoping. The reaction was also observed in inert and dry atmosphere, using dry equipment and solvents. From this observation it is concluded that lithium acts as an activating agent, possibly via coordination to the nitrogen functionality of the spiro-MeOTAD. As the solvent and LiTFSA are theoretically inert against a redox reaction with the hole conductor, no direct redox partner could be identified. No impurities from the synthesis process or from the solvent, which might be responsible for the oxidation reaction, could be detected spectroscopically. It is also possible that the oxidation of the spiro-MeOTAD takes place as lithium activated excimer formation with subsequent auto doping. Lithium ions were already earlier suspected of catalyzing the doping of the hole conductor.[45] In this context, the influence of the lithium ions was discussed to assist the oxidation of the spiro-MeOTAD by the $[SbCl_6]^-$ ion by withdrawing chloride ions from the chemical equilibrium. No photo effect was specified in respect of the observed doping reaction.

Mismatch Between White-Light and IPCE Measurements

For the SSD discussed in section 5.3.1 the short circuit current obtained in the white-light experiment did not agree with the integrated current derived from the a IPCE experiment.[*] Furthermore important differences between IPCE measurements of the same cell were found depending on the time of exposure to high white light intensities prior to the IPCE measurement. Higher short circuit current in the white-light experiment than expected from the IPCE measurement is also a known phenomenon for the DSSC and was attributed to thermal activation of the charge transport at the higher light intensities used for the white-light characterisation. Improved charge transport at higher light intensities was furthermore expected from the filling of trap states by photoinjected electrons. In addition UV illumination was found to provoke large enhancements in photocurrent.[46-48] In the case of the SSD the main reason for the different values of short circuit currents obtained from the two experiments is expected to be the lithium-activated photodoping. The spectrum of the sulphur lamp used for the white light characterisation (Appendix A.1.2) shows only a very low contribution of light below 400 nm. Nevertheless for light intensities superior to 50 % Sun, clear photodoping was observed. The result of the photodoping is a significant improvement in charge transport by the hole conductor, making the cell more linear in terms of the current output at different light intensities. Simultaneously, the photo doping will provoke a decrease of the IPCE due the increased charge recombination for higher doping

---

[*] The IPCE was typically measured in the wavelength region from 400-800 nm.

levels. The photodoping was also observed when the IPCE spectrum included the UV light region.

Due to this photodoping effect reliable photovoltaic characterisations require the use of UV-filters. Furthermore for all devices of an experimental series the same measuring parameters were used, including time of exposure to a light source.[*] Typically IPCE measurements were performed before and after the white-light measurements to check for the photodoping effect. For the same reason impedance measurements discussed in chapter 7 employed monochromatic light of low intensity.

5.4 Conclusions

• The blending of the hole conductor matrix with tBP and lithium salt was found to be the most promising approach to retard interfacial charge recombination and to considerably improve the device performance of the SSD. The introduction of tBP results in a drastic enhancement in U_{OC}. The presence of lithium ions in the hole conductor matrix increases the current output, and - to a lesser extent - also the open circuit potential.

• The effect of the two additives are different from the one in the DSSC, where the increase of the U_{oc} due to tBP and the increase of the I_{SC} were mainly attributed to the flat band potential determining properties of theses components. The charge screening effect of lithium ions at the interfaces seems to be more important than the effect of these ions on the band energetics of the TiO_2. Devices without lithium ions show very bad performance indicating that lithium ions are essential for device function. The simultaneous presence of lithium and tBP in the spin coating solution changes the dielectric properties of the chlorobenzene based solution and actually helps dissolving higher amount of lithium.

• Distorted current-voltage characteristics were obtained in the presence of tBP. This was attributed to the superposition of the photocurrent and the enhanced dark current resulting from the build up of charge at the interface as a result of the electron transfer blocking behaviour of the tBP. In addition the tBP was found to lower the doping level of the hole conductor. Distortion of the current-voltage characteristics could be avoided by application of higher lithium concentration to the hole conductor and by adjusting the layer thickness of the spiro-MeOTAD film and the TiO_2.

---

[*] In the early stages of the present work, the white-light measurement was performed using a sample holder, which allows the subsequent measurement of four devices with each 4 diodes (i.e. 16 diodes). Although saving overall measuring time this measurement technique significantly enhanced the exposure of the devices to high light intensities.

- UV light provokes the photodoping of spiro-MeOTAD in the presence of lithium ions. This process is independent on the solvent used for the spin-coating and the counter ion of the lithium salt. Application of a UV filter could avoid the photo doping of the spiro-MeOTAD in solution and rendered also the device more stable against the doping process. The photodoping manifests itself in a drastic increase in charge transport and in a significant drop of the IPCE values.

- The doping concentration of the hole conductor was found to be the most important factor for the increase of the recombination kinetics. This implies a trade-off for the SSD: At low doping levels the cell works with a high efficiency at low light intensity, but is non-linear for increasing light intensities. Best device performance is typically obtained for 20 % Sun. For higher doping levels the cell works with a comparable efficiency at all light levels. This efficiency is however rather low compared to the efficiency at low doping level and low light intensity. The compromise between doping and recombination can be changed towards higher efficiencies for all light levels using high lithium concentrations and adjusting the layer thickness of the TiO_2 and the HC film. The main problem however persists, which is the low charge transport of the hole conducting material.

5.5 References

[1] K. Kalyanasundaram and M. Grätzel. *Coord Chem Rev* **1998**, *77*, 347–414.

[2] B. O'Regan, J. Moser, M. Anderson, et al. *J Phys Chem* **1990**, *94*, 8720-8726.

[3] S. A. Haque, Y. Tachibana, R. L. Willis, et al. *J Phys Chem B* **2000**, *104*, 538-547.

[4] S. A. Haque, Y. Tachibana, D. R. Klug, et al. *J Phys Chem B* **1998**, *102*.

[5] N. W. Duffy, L. M. Peter, R. M. G. Rajapakse, et al. *J Phys Chem B* **2000**, *104*, 8916-8919.

[6] P. J. Cameron, L. M. Peter and K. G. U. Wijayantha. "The "Comorant" Workshop on Nanomaterials for Photo Energy Conversion";Official satellite meeting of the 14th IPS, 2002.

[7] K. Schwarzburg and F. Willig. *Appl Phys Lett* **1991**, *58*, 2520-2523.

[8] F. Cao, G. Oskam, G. J. Meyer, et al. *J Phys Chem* **1996**, *100*, 17021-17027.

[9] P. E. d. Jongh and D. Vanmaekelbergh. *Phys Rev Lett* **1996**, *77*, 3427.

[10] B. O'Regan, M. Grätzel and D. Fitzmaurice. *Chem Phys Lett* **1991**, *183*, 89-93.

[11] G. Rothenberger, D. Fitzmaurice and M.Grätzel. *J Phys Chem* **1992**, *96*, 5983-5986.

[12] G. Redmond, D. Fitzmaurice and M. Grätzel. *J Phys Chem* **1993**, *97*, 6951-6954.

[13] N. W. Duffy, L. M. Peter and K. G. U. Wijayantha. *Electrochem Commun* **2000**, *2*, 262-266.

[14] N. Kopidakis, E. A. Schiff, N. G. Park, et al. *J Phys Chem B* **2000**, *104*, 3930-3936.

[15] G. Schlichthörl, S. Y. Huang, J. Sprague, et al. *J Phys Chem B* **1997**, *101*, 8141-8155.

[16] F. Nüesch, L. Si-Ahmed, B. Francois, et al. *Adv Mater* **1997**, *9*, 222.

[17] L. Zuppiroli, L. Si-Ahmed, K. Kamaras, et al. *Eur Phys J B* **1999**, *11*, 505-512.

[18] I. H. Campbell, J. D. Kress, R. L. Martin, et al. *Appl Phys Lett* **1997**, *71*, 3528-3530.

[19] J. Krüger, U. Bach and M. Grätzel. *Adv Mat* **2000**, *12*, 447-451.

[20] B. A. Gregg, F. o. Pichot, S. Ferrere, et al. *J Phys Chem* **2001**, *105*, ?

[21] G. R. R. A. Kumara, A. Konno and K. Tannakone. *Chem Lett* **2001**, *2*, 180-181.

[22] K. Tennakone, J. Bandara, P. K. M. Bandaranayake, et al. *Jpn J Appl Phys* **2001**, *40*, L732.

[23] A. Zaban, S. G. Chen, S. Chappel, et al. *Chem Commun* **2000**, 2231.

[24] S. G. Chen, S. Chappel, Y. Diamant, et al. *Chem Mater* **2001**, *13*, 4629-4634.

[25] E. Palomares, J. N. Clifford, S. A. Haque, et al. *Chem Commun* **2002**, 1464–1465.

[26] E. Palomares, J. N. Clifford, S. A. Haque, et al. *J Am Chem Soc* **2003**, *125*, 475-482.

[27] A. Zaban, A. Meier and B. A. Gregg. *J Phys Chem B* **1997**, *101*, 7985-7990.

[28] U. Bach, D. Lupo, P. Comte, et al. *Nature* **1998**, *395*, 583-585.

[29] J. Gao, G. Yu and A. J. Heeger. *Adv Mat* **1998**, *10*, 692-695.

[30] S.-Y. Huang, L. Kavan, A. Kay, et al. *Act Pass Electron Comp* **1995**, *18*, 23-30.

[31] C. A. Kelly, F. Farzad, D. W. Thompson, et al. *Langmuir* **1999**, *15*, 7047-7054.

[32] D. Cahen, G. Hodes, M. Gratzel, et al. *J Phys Chem B* **2000**, *104*, 2053-2059.

[33] J. Moser, S. Punchihewa, P. P. Infelta, et al. *Langmuir* **1991**, *7*, 3012-3018.

[34] M. K. Nazeeruddin, A. Kay, I. Rodicio, et al. *J Am Chem Soc* **1993**, *115*, 6382-6390.

[35] S. Y. Huang, G. Schlichthörl, A. J. Nozik, et al. *J Phys Chem B* **1997**, *101*, 2576-2582.

[36] J. Moser, S. Punchihewa, P. P. Infelta, et al. *Langmuir* **1991**, *7*, 3012-3018.

[37] G. Friesen and H. A. Ossenbrink. *Sol Energ Mat Sol C* **1997**, *48*, 77-83.

[38] R. Rathore, A. S. Kumar, S.V.Lindemann, et al. *J Org Chem* **1998**, *63*, 5847-5856.

[39] F. A. Bell, A. Ledwith and D. S. Sherrington. *J Chem Soc C* **1969**, 2719.

[40] G. W. Cowell, A. Ledwith, A. C. White, et al. *J Chem Soc B* **1970**, 227.

[41] M. Primet, P. Pichat and M.-V. Mathieu. *J Phys Chem* **1971**, *75*, 1221-1226.

[42] F. Bonino, A. Damin, S. Bordiga, et al. *J Phys Chem B* **2003**.

[43] S. Suzuki, H. Onishi, K. Fukui, et al. *Chem Phys Lett* **1999**, *304*, 225-230.

[44] M. I. Zaki, M. A. Hasan, F.A. Al-Sagheer, et al. *Colloids Surf A* **2001**, *(2001)*, 261–274.

[45] U. Bach. Ph. D. Thesis, EPFL, 2000.

[46] B. O'Regan and D. Schwartz. *Chem Mat* **1998**, *10*, 1501-1509.

[47] B. A. Gregg, S.-G. Chen and S. Ferrere. *J Phys Chem B* **2003**.

[48] S. Ferrere and B. A. Gregg. *J Phys Chem B* **2001**, *105*, 7602-7605.

6 LIGHT HARVESTING

SILVER COORDINATION OF THE SENSITISER

This chapter discusses different strategies to improve the light harvesting of thin TiO_2 layers. The dye uptake in the presence of silver ions presents a rather simple method to increase the dye loading and to significantly improve the device performance of thin TiO_2 layer devices. Different spectroscopic methods, such as UV-VIS-, IR- and X-ray photoelectron spectroscopy were used to study the influence of the silver ions on the dye and on the dye-sensitised device. The spectroscopic data imply that the silver is mainly binding to the sensitiser via the ambidentate thiocyanate, which allows the formation of ligand-bridged dye complexes.

6.1 Light Harvesting in SSD

The light harvesting (LH) of SSDs is considerably lower than for DSSCs. This is mainly a result of the thin TiO_2 layers used in the SSD. TiO_2 films with thicknesses higher than 4 μm are less mechanically stable upon drying of the hole conductor solution and tend to peel off. The maximum feasible TiO_2 film thickness depends on the porosity of the colloid used for the preparation of the film. In general the pore size and the pore size distribution of the mesoporous TiO_2 film is much more important in the SSD than in the DSSC, as the size of the hole conductor molecule* is large compared to the iodide system. In particular for SSD, employing polymers as the hole transporting material, it has been shown that the device performance decreases because of a lack of pore filling.[1] The filling of the pores with spiro-MeOTAD was studied by SEM and the measurement of photoresponse spectra for front and rear incident illumination.[2] From these studies and the fact that a compact underlayer is needed to block the direct contact between spiro-MeOTAD and SnO_2 it is expected that the

---

* The diameter of the spiro-MeOTAD is about 2 nm (MacSpartan© calculations)

organic hole conductor reaches down to the back substrate. However, the homogeneity of the filling of the whole porous TiO_2 network with hole conductor remains questionable. ORegan[3] has determined the average pore filling of the TiO_2 with the hole conductor CuSCN by weighing the TiO_2 films before and after deposition of the CuSCN. The degree of pore filling achieved was determined to be near 100 % for TiO_2 films <2µm thick and falls to ≈65 % for films near 6 µm. The decreased pore filling for thicker films has been explained by the blocking of pores by overlaying solution before deeper pores have filled during the deposition process and precipitation of CuSCN on or near the surface of the TiO_2 film. Beside inefficient charge collection, low APCE values can therefore also be the result of imperfect pore filling of the nanocrystalline TiO_2 network with the dye regeneration material.

Figure 6.1 shows the dependence of the solar cell performance on the thickness of the TiO_2 layer for a given colloid. The highest IPCE value is obtained for the sample with a 2.5 µm layer. The enhanced IPCE with increasing layer TiO_2 thickness is due to the increased light harvesting for thicker layers. For the thinnest TiO_2 layer the IPCE resembles very much the absorption spectrum of the dye sensitised layer. As the absorbance increases with increasing TiO_2 layer thickness, the LH spectrum (LH=1-T) becomes larger which is reflected in the IPCE spectrum for the cells with higher TiO_2 thicknesses. Reaching a certain layer thickness, the loss mechanisms becomes determining, lowering the conversion efficiency. This is in contrast to the findings for the electrolyte cell, where the IPCE is scaling with the layer thickness up to a layer thickness of 14 µm. Comparison of the maximum APCE, which corresponds to the LH independent conversion efficiency, is even more striking. Taking reflection losses at the substrate into account (depending on the TCO, 12-15 %) the APCE values for the cells with 1.5 and 2.5 µm are close to unity while the 4 µm only shows a maximum APCE of 45 %.
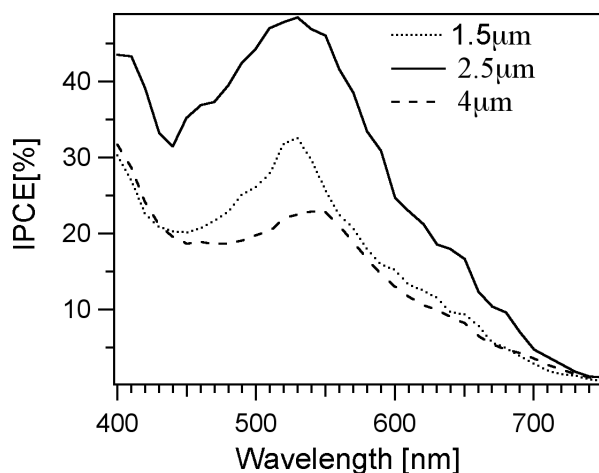

Figure 6.1: Dependence of IPCE on the thickness of the TiO_2 layer for a colloid with a porosity of 66 % and an active surface area of 83 m^2/g.

The spectral shape of the IPCE can give some hints for the identification of loss mechanisms in the device. Incomplete pore filling is expected to influence the cell performance in particular in TiO_2 layers near to the substrate, as the charge collection is most efficient in this region. Dye molecules which are not in contact with the hole conductor are inactive concerning energy conversion, but act as a filter attenuating the light incident to the photoactive part of the cell. At the same time the overall LH decreases. As a result of incomplete pore filling the IPCE spectra will show a flattened shape in the wavelength region where the dye is absorbing as well as lower values over the whole spectral range. On the other hand hole conductor situated near the substrate (i.e. good pore filling) should provoke a filter effect around 400 and 520 nm.[*] In particular the absorption at 520 nm can provoke a shift of the IPCE maximum to lower wavelength, letting pass only light of shorter wavelength. For the case of recombination limited charge transport the IPCE is expected to be narrow, as the photoactive part of the cell is limited to a thin layer at the substrate.

Whether the decrease of the IPCE for thick TiO_2 layers in the SSD is caused by insufficient pore filling or increased recombination or a combination of both is difficult to judge only from the IPCE data. However, the loss in efficiency with increasing TiO_2 film thickness is unambiguous. In addition to the improved spectral response, SSD based on thinner TiO_2 films show lower series resistance and higher open circuit potential. Correspondingly the SSD based on the 1 μm film shows a U_{OC} of 780 mV at AM1.5, which is 26 mV higher than for the 2 μm film cell, despite of the higher light harvesting for the latter cell. For the 3 μm film the U_{OC} drops even further to 719 mV. This discussion implies that a significant improvement of device performance can be expected when increasing the LH while keeping the dye-sensitised TiO_2 film as thin as possible.

6.2 Strategies to Improve the LH of Thin TiO_2 Films

Different strategies to improve the LH in dye-sensitised solar cells without changing the layer thickness of the nanocrystalline TiO_2 have been tested in the SSD:

1. Scattering Particles in the Mesoporous TiO_2

TiO_2 films containing scattering particles are produced either from a mixed colloid of standard and scattering particles or by deposition of a transparent film based on small TiO_2 particles and a second opaque layer on top (containing for example rutile particles). Reflecting particles are of bigger size so that the surface for dye adsorption is reduced when

---

[*] Absorption maxima of spiro-MeOTAD respectively its oxidised form.

keeping the same layer thickness. However, increasing the overall layer thickness to keep the overall TiO_2 surface constant leads back to the problem of increased TiO_2 layer thickness discussed above. Experiments using scattering particles show increased LH in the infrared. The white light photovoltaic characterisation of SSD based on scattering particles yielded lower photo potential and higher series resistance than for the reference with the standard TiO_2 film.

2. Modification of the Sensitiser

Application of dye with higher absorption coefficient

Organic dyes bear in general higher molecular extinction coefficients than metal organic dyes. Natural dyes have been used in the DSSC[4,5] and different groups of organic dyes were tested for the application in DSSC. In particularly merocyanines were extensively studied[6,7] and were applied as sensitiser in the SSD.[2] High IPCE values of up to 60 % were obtained with the so called MC2[*] merocyanine dye. However, merocyanines are less stable than the metal organic ruthenium complexes and the spectral response of merocyanines is much more dependent on the environmental conditions (for example protonation degree of TiO_2) than the N3 type dye. The strong dependence of the merocyanine dye spectra on the dye environment (solvatochromie) complicates the analysis of experiments with different hole conductor compositions.

Structural variations to enhance LH at low energies

The absorption range of the dye can be tuned by variation of the thiocyanate ligand (t_{2g} tuning), the bpy ligands (π^*level tuning) or the exchange of the central metal atom (heavy atom effect). Due to the spin-orbit coupling, the low energy spin-forbidden ^{3}MLCT transition becomes weakly allowed in ruthenium polypyridyl complexes. By replacing ruthenium with a central atom of higher atomic number, such as osmium, the ^{3}MLCT transition is expected to be enhanced corresponding to a higher absorption coefficient at low energies. There are promising examples for osmium polypyridyl complexes.[8,9] Similarly the thiocyanate ligand has been exchanged by the heavy iodide ligand, in order to increase the absorption coefficient of the spin-forbidden ^{3}MLCT transition as a result of the enhanced spin-orbit coupling.[10] However, the corresponding dyes could not replace N3 as standard sensitiser so far.

Polynuclear compounds

For the sensitisation of TiO_2 a number of polynuclear compounds, i.e. complexes with more than one ruthenium ion, have been studied.[11] This type of sensitisers have also been named

---

[*] 3-acetyl-5-12-(3-ethyl-2-benzothiazolydene)rhodanine, alternative abbreviation: KF 599

antenna molecules, due to their enhanced molecular absorption coefficient of the whole complex via the additional light absorption of peripheral units. Antenna molecules only add LH in the same spectral domain as the monomolecular systems. The spectral broadening of the LH is negligible. Due to their size, polynuclear complexes need a larger surface footprint and might coat the semiconductor surface less densely than their mononuclear analogues, which results in no net gain in the absorption of the device.

Surface Plasmon Resonance Effect

The possibility to improve the LH has also been evaluated by making use of the so-called surface plasmon resonance effect (SPRE).[12] Ihara found the absorption of N3 significantly increased in the presence of silver.[13] For long time there has been a great controversy about this enhancement mechanism. It is now widely accepted that two main mechanisms contribute, either independently or in tandem, to the SPRE. The electromagnetic theory considers that the enhanced signal intensities are due to the large increase in the electric field associated with the rough metal surface (surface plasmon excitation). The chemical mechanism considers the modulation of the Raman scattering cross-section of the adsorbate surface complex due to new charge-transfer transitions. The chemical enhancement of dye adsorption on the non-metallic surface in particular is the subject of recent studies,[14] while the electromagnetic enhancement mechanism on noble metallic surfaces such as silver, copper, platinum and gold has been studied widely and finds general application in the surface enhanced Raman scattering spectroscopy(SERS).[15-17] SERS requires a surface that is electrically conducting and has surface features of a size where the surface plasmons are able to resonate with light at the illuminating wavelength. Several methods have been published leading to SERS-active surfaces of varying quality.[18-20] However, the preparation of stable silver colloids, necessary for the SPRE is not straightforward. Furthermore the incorporation of silver particles in the device might also cause negative side effects, such as increased recombination at the interface. As a result SPRE is mainly used in analytical application (SERS) rather than for long-term application in devices like solar cells.

Bridged dye molecules

In the framework of this thesis another possibility has been found to improve the LH of SSD without changing the structure of the mesoporous TiO_2, but making use of the ambidentate thiocyanate ligand. Due to its ability to coordinate via the sulphur and/or the nitrogen, the thiocyanate forms a variety of complexes depending on the coordinating metal. The modes of metal coordination of chalcogeno cyanates in general, and the thiocyanates in particular, are best understood in terms of the hard-soft acid-base (HSAB) concept developed by Pearson, Basolo and Burmeister.[21,22] In accordance with the hard-soft acid-base concept, the S atom of the SCN-ligand, being a soft base, preferably coordinates to a soft acid,

whereas the N atom, being a hard base, coordinates to a hard acid. In this respect silver(I) is a good candidate as a soft acid favouring coordination to soft bases such as ligands containing sulphur and reacts readily with thiocyanate at room temperature. The chemistry of silver halogenides and silver pseudohalogenides has been studied in detail in the framework of the black-white photography.[23] Similar coordination processes based on metal ions such as Ag^+, Pt^+, Ni^{2+} with ruthenium complexes bearing cyano ligands instead of thiocyano ligands were studied by Demas.[24-26]

6.3 Impact of Silver(I) on the Performance of SSD

Silver ion modified devices were fabricated in an identical manner as described in previous chapters except for the dye uptake, which was performed from a dye solution containing one dye mol equivalent of silver nitrate. Current-voltage characteristics showed a significant improvement in the photovoltaic performance upon treatment with silver ions. Figure 6.2 displays the current-voltage characteristics of the reference device, the silver device and the post-treated silver device. The photovoltaic parameters of the three devices are summarised in Table 6.1.
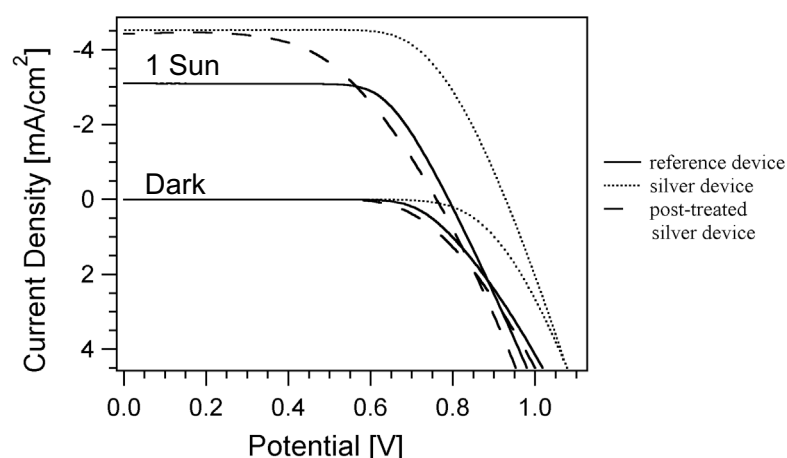
Figure 6.2: Current–voltage characteristics in the dark and at an illumination intensity of 1 Sun (corresponding to global AM 1.5 100 mW/cm^2) for a standard device without silver ions (solid line), a device dyed in the presence of silver ions (dotted line), and a device dyed in the presence of silver ions and washed with iodide solution prior to hole conductor deposition (dashed line). The spin-coating solution for the deposition of the hole conductor contained 0.1 M spiro-MeOTAD 0.13 mM in $Li(CF_3SO_2)_2N$, 0.11 M in tBP, and 0.4 mM in $N(p-C_6H_4 Br)_3SbCl_6$. An active electrode area of 0.16 cm^2 has been defined by a black mask.

The comparison reveals an increase of 13 % in open circuit voltage and of 31 % in short circuit current for the silver treated electrode relative to the untreated reference. Interestingly, the same improvement in short circuit current can be obtained when rinsing the silver treated TiO_2 film with iodide solution prior to hole conductor deposition, whereas the open circuit voltage shows similar values to the reference device without silver.

Device	J_{sc} (mA/cm^2)	U_{oc} (mV)	FF (%)	η (%)
reference device	3.5	821	0.69	2.1
Ag(I) device	4.6	931	0.71	3.2
post-treated Ag(I) device device	4.5	760	0.54	2.0

Table 6.1: Summary of the photovoltaic performance at an illumination intensity of 1 Sun (corresponding to global AM1.5 100 mW/cm^2) for the devices given in Figure 6.2.

6.4 Experimental Evidence for Silver Complexation

6.4.1 <u>UV/VIS Spectroscopy</u>

The presence of silver ions causes a pronounced change of the spectral behaviour of the dye in solution as well as when adsorbed onto TiO_2. Figure 6.3 shows the continuous addition of a silver nitrate solution to a solution of N3.
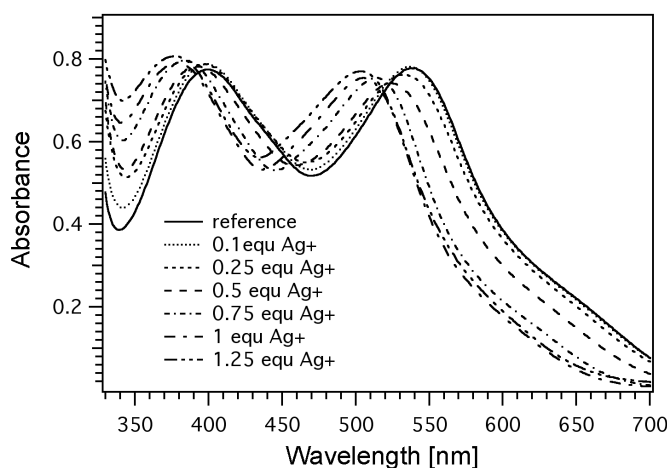
Figure 6.3: Titration of N3 in ethanol with an AgNO$_3$ solution in acetonitrile. While AgNO$_3$ solutions in ethanol show very slow deposition of elemental silver upon illumination, no silver reduction was observed for the acetonitrile solution. The dye was dissolved in ethanol, as its solubility is not high enough to perform this experiment in acetonitrile. To avoid any side reactions solutions were freshly prepared and handled under exclusion of light.

With increasing amount of silver ions the dye spectrum is shifted to lower wavelength. More than 1.5 dye equivalents of $AgNO_3$ cause hazing of the dye solution followed by precipitation.

Assuming that the silver ions do not cause any oxidative degradation of the dye the observed spectral feature can be assigned to the formation of a silver-dye complex. Based on the chemical nature of the silver ion, coordination is expected to take place either at the thiocyanate ligand and/or at the bpy carboxylic group. The observed spectral blue shift in the dye spectrum can be explained considering the energy transitions corresponding to the absorption bands of N3 in the visible region (Figure 6.4). The visible transitions of the Ru complex have metal-to-ligand charge-transfer (MLCT) character, involving the transfer of an electron from the metal d orbital to the π^* orbital of the bpy ligand. Ab initio calculations of a decarboxylated dye molecule and photoelectron spectroscopy indicate that the HOMO level is shared by both the Ru metal and the NCS ligands.[27,28] The MLCT transition energy can be increased by destabilisation of the bpy acceptor-based MO or by stabilisation of the metal based MO. In fact, the coordination of silver ions to the thiocyanate ligand leads to a decrease of electron density at the Ru(II) center and therefore to a blue shift of the corresponding MLCT transition. Blue shifts as a result of destabilisation of the bpy acceptor-based MO are obtained upon successive deprotonation of the bpy carboxylic acid groups. In contrast to the spectral shift caused by thiocyanate coordination the formation of silver carboxylate should withdraw electron density from the bpy ring and lead to a red shift comparable to the one obtained for the dye in solution of low pH. It might be possible that the spectral shift due to the silver carboxylate formation is obscured by the shift caused by the of the silver-thiocyanate coordination. From the UV/VIS experiment the coordination of the silver to the carboxylate cannot be excluded entirely.
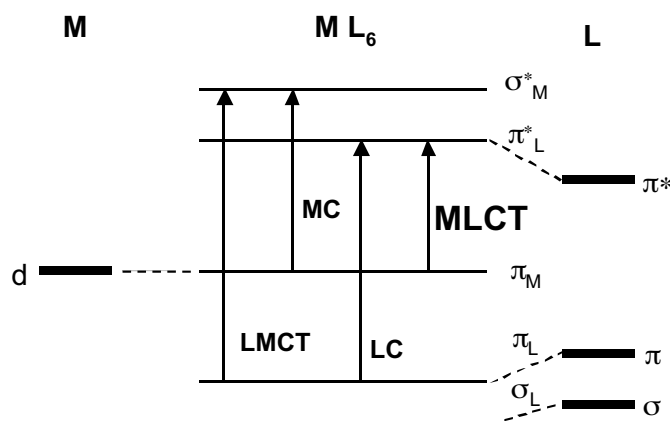

Figure 6.4: Simplified molecular orbital diagram for $[RuL_3]^{2+}$ complexes (with L=bipyridine) in octahedral symmetry showing the electronic transitions occurring at low energy.

Figure 6.5 displays the dye solution spectra, obtained after dye desorption from the surface of a 7 μm TiO$_2$ film using a phosphate buffer (pH 7). The comparison of the dye spectra with and without silver reveals a spectral blue shift of 28 nm. The appearance of a shoulder at 435 nm is believed to result from a MLCT transition (metal to thiocyanate[29]), which is normally not resolved in the dye spectrum without silver. It is striking that, although the dye uptake was established from a dye solution containing only 0.5 dye equivalents of silver, the spectral shift is larger than indicated in Figure 6.3. A similar change between the solution spectrum and the spectrum of the dye adsorbed onto TiO$_2$ film has also been observed employing the FTIR technique (chapter 6.4.3). These experiments show that the adsorption of the silver modified dye is favoured compared to the non-modified dye.
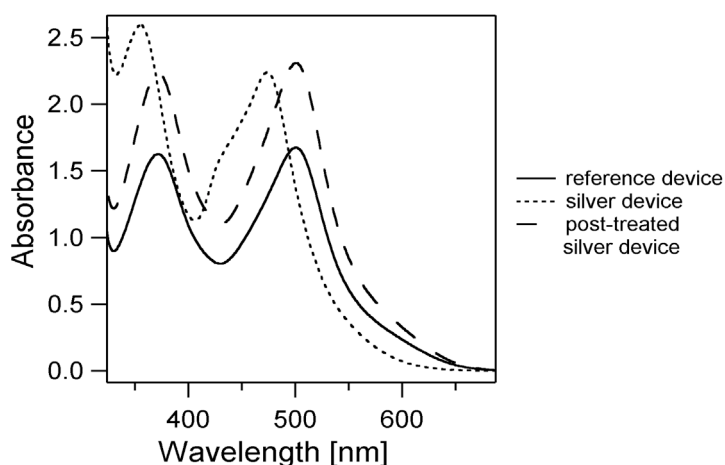
Figure 6.5: UV/VIS absorption spectra of (Bu$_4$N)$_2$[Ru(dcbpyH)$_2$(NCS)$_2$] in phosphonate buffer (KH$_2$PO$_4$ 0.026 M/Na$_2$HPO$_4$ 0.041 M, pH7) after desorption from TiO$_2$ surfaces. The solid curve shows the reference spectrum after dye uptake in absence of silver. The dotted curve corresponds to the spectrum for the dye uptake in presence of silver ions (0.5 dye equivalents), and the dashed curve to the spectrum for the dye uptake in presence of silver ions and subsequent removal of silver ions with iodide. The spectral shift of the curves compared to Figure 6.3 is caused by the aqueous solvent.

By removing the silver with an excess of iodide prior to dye desorption the original spectrum of (Bu$_4$N)$_2$[Ru(dcbpyH)$_2$(NCS)$_2$] is regenerated. The spectrum of the silver modified dye resembles the spectrum of the corresponding dicyano complex, which has been discussed to be the first step in the oxidative degradation of the N3 dye.[30,31] There might be some concern that the red shift caused by the treatment with iodide is the result of an exchange of NCS-Ag$^+$ by the iodide,[32] rather than by a recovery of the original dye.[*]

---

[*] In ethanol solution λ_{max} of [RuL$_2$(NCS)$_2$] and [RuL$_2$I$_2$] (L=bpy) are 534 and 536 respectively. However the extinction coefficient for the di-iodo complex is only the half of the one for the N3 dye.

However, such a ligand exchange is unlikely, since the experimental conditions are not adapted for a ligand exchange.[32,33] The recovery of the CN bond in the ruthenium complex after iodide treatment could also be proven by FTIR (chapter 6.4.3).

Assuming that the extinction coefficient did not change as a result of the temporary silver presence, the 38 % increase in absorption can be correlated to a higher amount of dye adsorbed to the TiO_2 surface.

6.4.2   <u>Fluorescence</u>

The emission spectrum for the silver modified dye system shows a spectral blue shift similar to the one observed in the absorption spectra (Chapter 6.4.1). The emission maximum for the N3 dye was measured at 880 nm, while the emission of the silver modified dye occurs around 725 nm (Figure 6.6). The increase in the energy of the MLCT excited state is generally accompanied by decreased non-radiative decay ("energy gap law"[34]), which corresponds to increased emission quantum yield. Relative emission quantum yields for the N3 dye with and without silver modification have been determined employing $[Ru(bpy)_3](PF_6)_2$ in H_2O as standard (ϕ_r=0.42). An emission quantum efficiency of 0.0009 has been determined for the N3 dye. Upon silver modification a value of 0.003 can be measured, which is significantly higher than the experimental error of about 5-10 %. The observed difference in emission quantum efficiency is thus in accordance with the theoretical predictions.[34]
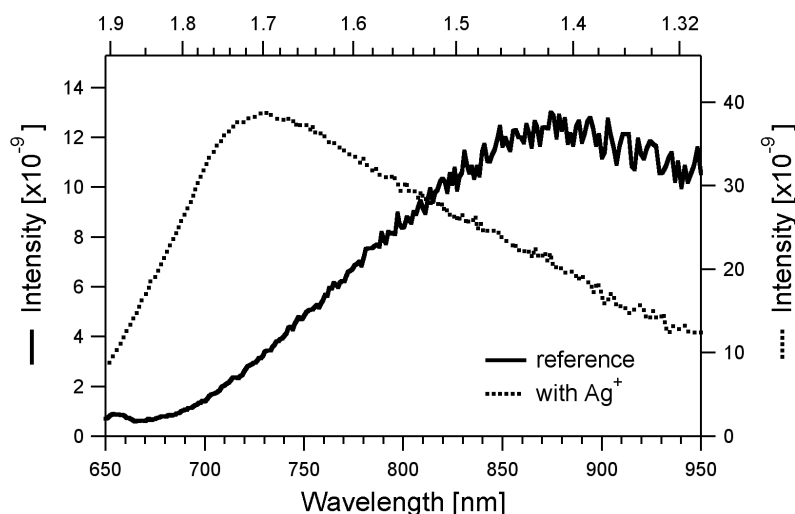

Figure 6.6: Emission spectra of N3 in ethanol, with (dashed line) and without silver (solid line) modification.

In terms of the application in the dye-sensitised solar cell the electronic interaction of the individual dye molecules needs to be considered. Electronic coupling of chromophoric units generally depends on the distance between the metal centers, the ability of the bridging ligand in delocalizing the electronic charge and the coordination environment of the metal ions. The photophysical observations in the polynuclear complex are the result of changes in the oxidation and/or reduction potentials, implication of the energy gap law and potential quenching processes. A conceptual model for this type of electronic coupling has been evaluated by Hush.[35] Classification of the coupling (from a delocalised class III to weakly coupled class II) has been established by Creutz.[36] One characteristic feature for electronic coupling between ruthenium units can be the quenching of the excited state of one unit by a neighbouring ruthenium unit, which might be unexcited (triplet-ground state annihilation) or also excited (triplet-triplet annihilation). Palaniappan[29] et al. observed weaker emission for a dimer of two [Ru(bpy)$_2$] units interconnected via a NCS bridge compared to the corresponding monomer. The observation of enhanced quantum efficiency for the modified dye system suggests that it behaves as silver-connected cluster of electronically separated units. However, for a conclusive interpretation of the extent of electronic coupling more photophysical and electrochemical data is necessary.

6.4.3   __FTIR Spectroscopy__

The UV/VIS experiment has shown that the silver coordinates reversibly to the N3 dye. The FTIR technique has proven useful for the study of dye structure and dye adsorption behaviour on the TiO$_2$.[37-40] Accordingly FTIR measurements were performed to further address the question of the coordination site of the silver. Figure 6.7 shows the photoaccoustic infrared spectrum of N3 powder in the region from 1000 to 2200 cm^{-1}. Regarding silver coordination to the N3 the following signals are of special interest:

1) *Coordination via the thiocyanate ligand: ν(CN)*

The thiocyanate has three characteristic vibrational modes ν(CN), δ(NCS), and ν(CS). The ν(CN) mode was chosen for the diagnostic of thiocyanate coordination, because of its distinctive position in the spectrum. The C-S stretching frequency and the NCS bending signal are of much lower intensity and often difficult to identify in the presence of other organic vibrations. N-bonding of the thiocyanate ligand leads to little change or to a decrease below the free ion value (2053 cm^{-1} in KSCN) while S-bonding results in an increase to near 2100 cm^{-1}. Bridging thiocyanate exhibit a signal well above 2100 cm^{-1}. The shift to higher wavenumbers for coordination through the sulphur can be attributed to increased contribution of the NCS$^-$ resonance structure with triple bond between nitrogen

and carbon. Accordingly wave numbers higher than 2100 cm^{-1} are expected for $\nu(CN)$ for silver ion coordination at the S side of thiocyanate ligand.

2) *Formation of silver carboxylate: $\nu(C=O)$, $\nu(CO_2^-)$, $\nu(C-O)$:*

For the N3 dye vibrational signals around 1740 and 1709 cm^{-1} are indicative for the presence of carboxyl acid C=O groups. The splitting of the vibrational signal is due to the inequivalence of the C=O in the trans position to the SCN group and in the trans position to the bpy ring. The antisymmetric and symmetric $\nu(CO_2^-)$ modes are found around 1610 cm^{-1} and 1380 cm^{-1} respectively. The splitting of these carboxylate stretching bands ($\Delta=\nu_{as}-\nu_s$) has frequently been used to distinguish whether the coordination of a metal by a carboxyl group is monodentate, bidentate or bridging.[41,42] The signals at 1272 and 1242 cm^{-1} have been assigned to the C-O stretching.[39] When half of the carboxyl groups are protonated (N719) only one band at 1235 cm^{-1} can be observed. For the completely deprotonated dye (N712) no band in this energy region can be observed. Coordination of the silver ions to the carboxyl group is likely to alter these three groups of vibrational bands. Depending on the mode of silver coordination, the negative charge is delocalised over the carboxylate group, resulting in two equivalent C-O bonds. This will result in the vanishing of the signals above 1700 and around 1235 cm^{-1}, as well as to the appearance of an intense, broad band at 1615 cm^{-1}. Even if the silver cation is binding in a similar manner as the proton the formation of silver carboxylate should be detectable by a clear shift of the discussed vibrational bands.
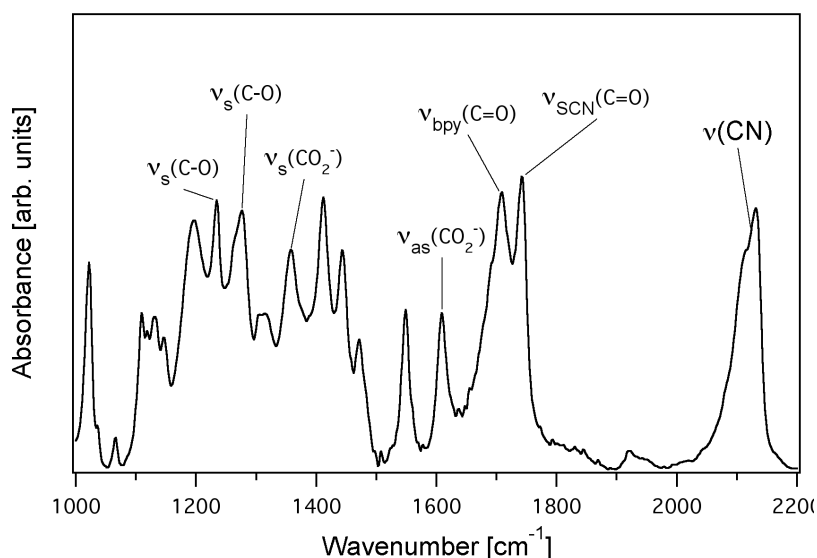

Figure 6.7: PAS spectrum of N3 powder (Solaronix) to demonstrate vibrational bands that might be altered by silver modification. The subscripts bpy and SCN indicate the splitting of the vibrational signal due to the trans position to the bpy ring and in the trans position to the SCN group. The high resolution of the PAS technique can even resolve the splitting of the $\nu(CN)$ band corresponding to the symmetrical and the anti symmetrical vibration of the thiocyanate groups.

Figure 6.8 shows the ATR-FTIR of silver modified N719 adsorbed onto a TiO_2 film. The amount of silver in the dye uptake solution was gradually increased up to half a dye equivalent of $AgNO_3$. Higher silver concentrations would induce precipitation of the dye on the TiO_2 surface.
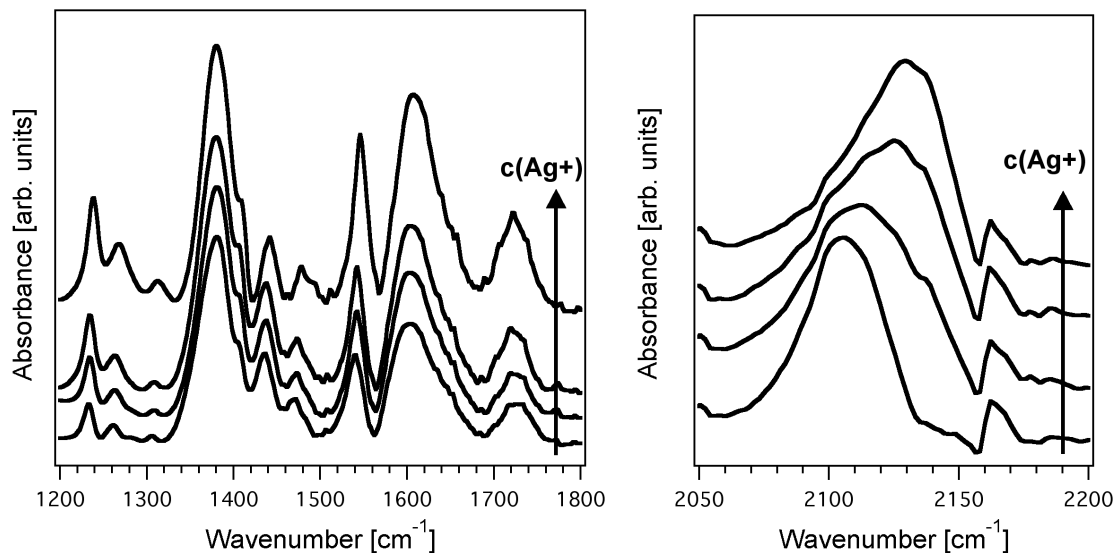

Figure 6.8: ATR-FTIR absorption spectra of N719 adsorbed on 3 μm thick TiO_2 film. The dye uptake was established from a dye solution containing 0,0.1,0.25 and 0.5 dye mol equivalents of silver ions.

A shift of the v(CN) band from 2104 cm^{-1} to 2131 cm^{-1} with increasing silver concentration is observed. 0.1 and 0.25 dye equivalents of silver show a small decrease in signal intensity and a peak broadening, which might be due to the presence of unresolved double peaks. For the carboxylic acid and carboxylate bands no significant shifts are visible, but an enhancement of signal intensity is observed for increasing silver concentration. Similar tendencies are observed when monitoring the influence of silver on the dye in solution (Figure 6.9). The decrease of the v(CN) signal at 2104 cm^{-1} and the increase of the v(CN) band at 2130 cm^{-1} are better resolved. No significant shifts are visible for the CO vibrations. The peak 1369 cm^{-1} is slightly shifted, which might be the result of the changing dielectric constant of the solvent upon application of $AgNO_3$. Corresponding to the UV/VIS experiment the v(CN) of the dye adsorbed on TiO_2 is already completely shifted to the maximal wave number for 0.5 dye equivalents. For the dye solution however this transition occurs only at much higher silver concentrations.

From these experiments it can be concluded that the silver coordination is taking place at the thiocyanate ligands. The impact of the silver ions on the discussed vibrational band does not depend on the protonation degree of the dye, i.e. the use of N3 (4 proton) or N719 (2 proton, 2 TBA).
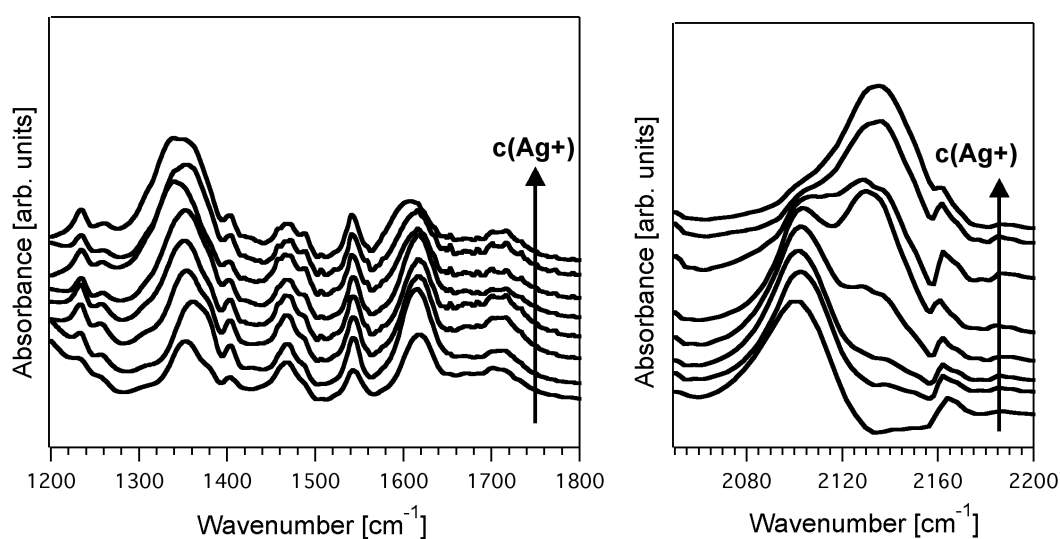
Figure 6.9: ATR-FTIR absorption spectra of N719 solutions modified with different amounts of $AgNO_3$ (0,0.1,0.25,0.5,0.75,1,1.25,1.5 dye mol equivalents of silver ions).

Similar to the observations made using UV/VIS spectroscopy, the spectral shift due to the silver modification is reversible by rinsing with iodide solution. The increase in peak intensity can again be assigned to an increased dye uptake onto the TiO_2 film.
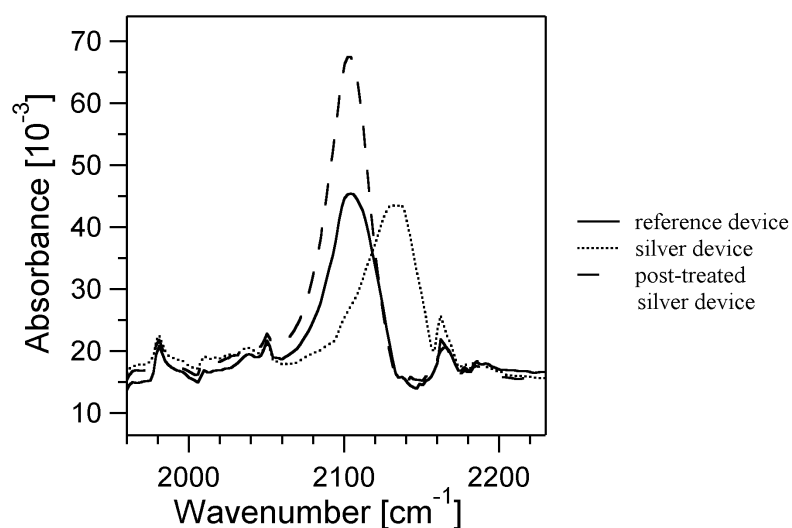

Figure 6.10: Infrared absorption spectra of $TBA_2[Ru(dcbpyH)_2(NCS)_2]$adsorbed onto 2 μm thick TiO_2 films in absence (solid line) and presence (dotted line) of silver ions and after removal of the silver ions with iodide (dashed line).

6.4.4   XPS Spectroscopy

X-ray photoelectron spectroscopy confirmed the presence of silver on the surface of the TiO_2 for the sample dyed in the presence of silver ions and washed with acetonitrile. Figure 6.11 represents the XPS survey of the binding energy region characteristic for Ag, Ru, C and N. The spectrum of the silver device shows two characteristic peaks at 368 eV and 378 eV, which are characteristic for silver $3d^{5/2}$ and $3d^{3/2}$. Figure 6.12 shows the high-resolution spectrum for Ag with a difference in binding energy of 6 eV between the two peaks, which is in accordance with the literature.[43] For the reference device no peaks were detectable around 370 eV within the experimental limits. The same is true for a sample, which was rinsed with a concentrated iodide solution after dye uptake from a silver containing solution. Furthermore no peaks are detectable at the characteristic binding energy of iodide around 619 eV for the post-treated silver sample. The atom ratio of the elements present on the TiO_2 surface has been calculated from the fits of the high-resolution spectra for the different peaks. The Ru/Ti atomic ratio for the sample containing silver is 38 % higher compared to the reference sample without silver.

The XPS spectrum of a TiO_2 layer which was immersed in a silver solution for the duration of the standard dye uptake, also showed the characteristic silver signals. Nevertheless the peak intensities were significantly lower compared to silver devices, indicating that the major silver content on the TiO_2 surface is coordinated to the dye and not attached to the TiO_2 itself.
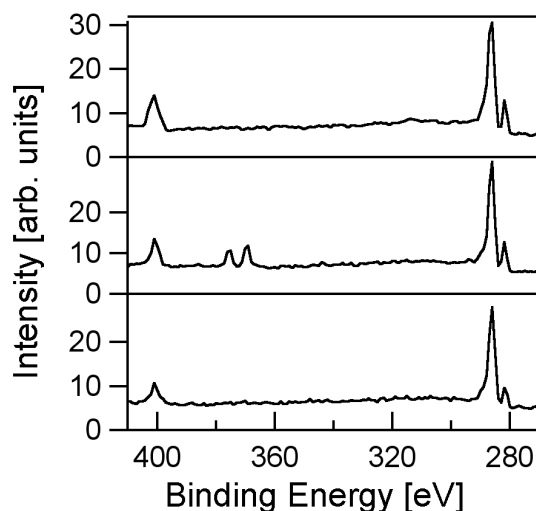

Figure 6.11: XPS spectra of $(Bu_4N)_2[Ru(dcbpyH)_2(NCS)_2]$ adsorbed onto a 1 μm thin TiO_2 film. The first curve shows the reference spectrum of aTiO_2 film after dye uptake in absence of silver ions. The second curve corresponds to the film after dye uptake in presence of silver ions, and the third curve to the film after dye uptake in presence of silver ions and subsequent removal of silver ions with iodide.

The chemical shift of Ag 3d photoelectron peaks does not allow for the clear distinction between the different chemical states of silver. In fact, the signal shift due to static charging of the sample has the same order of magnitude as the shift induced by a change in the oxidation state of the silver. Instead, the Auger parameter, defined as the difference in binding energy between the photoelectron line and the Auger line, can be accurately determined because static charge corrections cancel. From the fit of the of the Ag(MVV) high resolution spectrum the Auger parameters were computed as α_1=723.8 and α_1=719.9. These values indicate that silver is present in the form of Ag(I). Furthermore, metallic silver should be observable in the optical absorption spectrum due to the characteristic plasmon absorption at 440 nm as a result of the presence of reduced silver particles.[13] Such a characteristic peak was not observed for TiO_2 films dyed in presence of silver. However, it appeared when treating the samples with $NaBH_4$ solutions, indicating the reduction of silver ions on the surface.
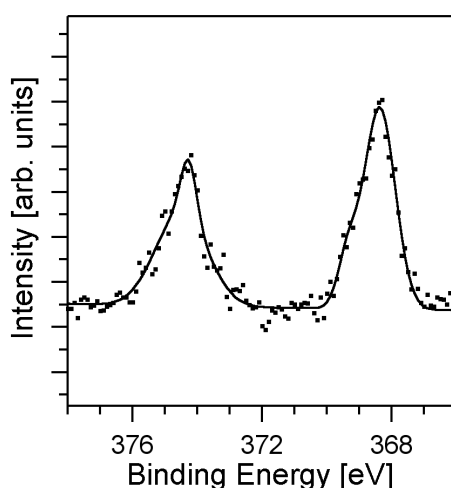

Figure 6.12: High-resolution XPS spectrum of the silver signal. The dotted curve represents the original data and the line the fitted data.

6.5 Further Investigation of the Silver Effect

From the spectroscopic evidences it is inferred that the silver is binding to the sensitiser via the ambidentate thiocyanate, allowing the formation of ligand-bridged dye complexes. Since isosbestic points are not strictly maintained in the spectral variation during titration of the dye with silver ions, both 1:1 and 1:2 adducts of silver and dye are likely to be formed. The model of dye interconnection via the thiocyanate ligand is supported by the work of Kinnaird,[44] who studied the complex formation of silver with $[Ru(bpy)_2(CN)_2]$. This

publication describes the completely reversible formation of DAg+ and D_2Ag+ complexes (with D=[Ru(bpy)$_2$(CN)$_2$]) via the cyano ligand, which show blue shifted UV/VIS spectra and decreased rates for non-radiative decay. Based on their potential to interconnect dye molecules, the silver ions are expected to assist the dye assembling on the surface and thus to increase the density of the molecular dye layer on the TiO_2. The more tightly packed dye layer is expected to block the electron back transfer from the TiO_2 to the spiro-MeOTAD. Accordingly the enhanced photopotential can be rationalized in terms of simultaneously increased photocurrent and decreased recombination current (see Equation 3.2).

Beside this dye organisation effect, silver ions might provoke additional effects in the SSD. Silver ions have already been reported earlier to affect the performance of photoelectrochemical devices.[13,45] Different mechanisms were postulated to account for this observation, such as increased conductivity due to the silver particles in an otherwise resistive film, an improved exchange of charge between the dye and the hole conductor, catalytic effects of the surface metal particles[46] or the enhancement of the photo excitation of electrons by the surface plasmon resonance of aggregated metal particles.[14,16,17]

Silver salts are known for their photosensitivity. There might be a risk that the in the dye layer incorporated silver ions are reduced to Ag(0) under illumination of the solar cell. Although this mechanism does not explain the increased optical density of the silver treated TiO_2 films prior to solar cell operation (i.e. illumination), Raman spectroscopy experiments were performed to test the silver modified devices for surface enhanced Raman scattering (SERS). The signal intensities were consistent with the increased optical density of the films, but did not show the expected high enhancement factors typical for surface plasmon resonance. The increase of the extinction coefficient by the resonance Raman effect can therefore be excluded as explanation for the performance improvement in presence of silver ions.

The effect of the silver cations might also be of electrostatic nature. Upon adsorption of the dye via the carboxylate group the TiO_2 becomes negatively charged. Therefore the absolute dye uptake is controlled by the electrostatic repulsion between the dye molecules. The intercalation of cations, in particular the lithium cation showed a significant increase in dye uptake, which has been assigned to the screening of the negative charged correlated with the dye uptake.[*] Charge Screening effects as caused by lithium cations are also expected for the silver ions.

---

[*] R. Humphrey-Baker, unpublished results

In order to detect additional effects on the SSD related to the silver ions different, dye structures and a different hole-transporting medium were used in combination with the silver modification. Further spectroscopic studies were performed to elucidate whether similar effects can be observed with other metal cations. Experiments which employ different dye structures and hole conducting systems offer furthermore information regarding the applicability of this dye modification technique in other devices.

6.5.1   Variation of Dye Structure

Two dye series have been studied in terms of the dye uptake in presence of silver ions in the dye solution: The first series is based on dyes without the thiocyanate ligand. A second series includes hydrophobic dyes, containing bpy ligands with aliphatic chains of different length, which have been discussed earlier (chapter 4). These series were complemented with the black dye which is known to show lower dye uptake than the standard N3 dye.

Ruthenium Complexes Without Thiocyanate Ligand

The application of dyes without thiocyanate ligand (Figure 6.13) is a control experiment to verify the silver coordination to the dye molecule via the thiocyanate ligands, since no spectral change is expected without a thiocyanate ligand. Figure 6.13 compares the dye structures used for this experiment.
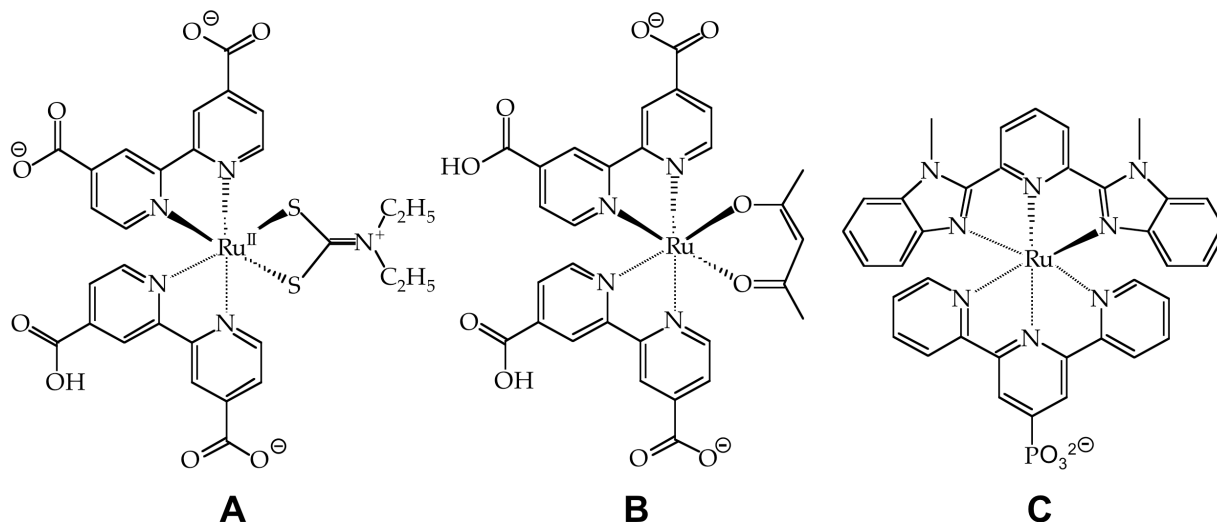

A   **B**   **C**

Figure 6.13: Dye molecules to study the effect of silver ions on the dye uptake:

A: TBA$_2$[Ru(dcbpyH$_2$)$_2$L], with L=diethylthiocarbimide

B: [Ru(dcbpyH$_2$)(dcbpyH)L], with L=acetylacetonate

C: [Ru(terpyH$_2$PO$_3$)(dmpip)]

Dye A has double negative charges while dye B and C are inner salts and are overall neutral. Table 6.2 summarises the effect of silver ions on the dye uptake of the three dye molecules presented as change of absorbance at the maximum wavelength. No or nearly no spectral shifts were observed for the dyes B and C. A blue shift of 6 nm was determined for the dye A, which contains the diethylthiocarbimide ligand. This spectral shift might be attributed to the association of silver ions with the sulphur of the thiocarbimide ligand. However, the increase in optical absorbance is smaller than for dye B and C. The higher dye uptake for B and C might be a result of charge screening due to silver ions. In the case of dye A charge screening by the silver might be less efficient because of the affinity of the silver to the sulphur. The experiment shows that there might be an additional effect due to charge screening. However, this effect is not strong enough to explain the experimental observations discussed in section 6.4.

Dye	λ_0 [nm]	λ_{Ag} [nm]	ΔA [%]
A	544	538	5.7
B	527	527	11.6
C	484	482	10.4

Table 6.2: Effect of silver ions on the dye uptake of dyes without thiocyanate ligand.

λ_0 [maximum absorption without silver ions

λ_{Ag} [maximum absorption in the presence of silver

$\Delta A = [A(\lambda_{Ag}) - A(\lambda_0)/A(\lambda_0)]*100$ %: difference in absorptions of the sample without and with silver.

Neutral Metal Organic Dyes

Electrostatic effects should be detectable using dye molecules, which provoke less surface charging upon adsorption on the surface. In this respect the silver modification has been applied to the hydrophobic dye series [Ru(dcbpyH$_2$)(dcbpyR$_2$)(NCS)$_2$], with R=aliphatic chains of differing lengths, which was introduced in chapter 4. Table 6.3 summarises the performance at 10 % Sun and at 100 % Sun for the devices sensitised with the different dyes. The trend which has been found earlier (see chapter 4.2.4), i.e. the improved short circuit current and open circuit potential for longer aliphatic chains, is preserved upon treatment with silver. As for the SSD based on the N719 dye the photovoltaic performance improved for all hydrophobic dyes when adsorbed onto the TiO$_2$ in presence of silver ions. In contrast to the N719 based SSD the increase in U$_{OC}$ for the hydrophobic dye sensitised SSDs is rather small. The fact that the influence of silver co-adsorption on the device performance is different for neutral and charged molecules indicates that also electrostatic effects have to be considered for the explanation of the silver effect. Due to their chemical

nature (for example HSAB concept) silver ions are expected to be located on the dye rather than at the TiO_2 surface, while for lithium ions the contrary is true. In this respect, silver ions might be more efficient than lithium ions for the screening of the dye charge. Because of their size, the concentration of TBA^+ ions at the TiO_2 surface or inside the dye layer is low and thus also the screening of the negative dye charge. Accordingly the silver ions are expected to be more important for the reduction of the recombination current in the case of the negatively charged sensitizer complex than for the neutral dyes.

Dye	10 % Sun			
	J_{SC} [mA/cm^2]	U_{OC} [mV]	FF [%]	η [%]
N3_C$_1$	0.454±0.849	662±31	0.58±0.10	1.8±0.3
N3_C$_9$	0.468±0.090	711±15	0.75±0.14	2.5±0.1
N3_C$_{12}$	0.525±0.016	744±7	0.75±0.03	3.0±0.2

Dye	100 % Sun			
	J_{SC} [mA/cm^2]	U_{OC} [mV]	FF [%]	η [%]
N3_C$_1$	4.6±0.6	747±25	0.50±0.08	1.8±0.4
N3_C$_9$	5.0±0.5	792±10	0.54±0.04	2.2±0.3
N3_C$_{12}$	5.1±0.7	839±5	0.66±0.08	3.0±0.5

Table 6.3: Summary of the photovoltaic performance at an illumination intensity of at 10% Sun and 100 % Sun (corresponding to global AM 1.5 100 mW/cm^2) for a series of SSD based on the hydrophobic dyes discussed in chapter 4. For the composition of the hole conductor film compare Figure 6.2.

"Black Dye"

TBA$_2$[Ru(H$_2$tcterpy)(NCS)$_3$] (N749), also called black dye because of its broad absorption spectrum, covering the whole visible spectrum,[47] is particularly of interest in context with the beneficial effect of the silver ions on the dye uptake. Although its spectral properties would make it the ideal sensitiser, the "black dye" has not yet replaced the N3 dye due to its less favourable adsorption properties. The surface coverage of the TiO_2 with the black dye is lower than for the N3 dye and does not reach a monolayer.[48] This was rationalised in terms of the larger footprint of the black dye compared with the red dye. Furthermore the extinction coefficient of this dye is only around 7500 M^{-1}cm^{-1}, depending on the solvent and the degree of protonation, which is only about half the extinction coefficient of N3. The black dye has already been used earlier as sensitiser in the spiro-MeOTAD solid-state cell. However, devices based on the black dye could not at all compete with the devices prepared with the

red dye. Coordination of the dye molecules via silver ions is expected to considerably improve the adsorption of the black dye on the mesoporous TiO_2.

For the N749.2, similar spectral shift in the UV/VIS and in the FTIR spectra were observed as for the N3 upon silver ion modification. Figure 6.14 shows the titration of N749.2 with $AgNO_3$ followed by UV/VIS spectroscopy. The maximal spectral shift is obtained at 561 nm. For silver concentration over 1 dye equivalent of $AgNO_3$ precipitation upon formation of a colloidal suspension hinders further UV/VIS measurements.
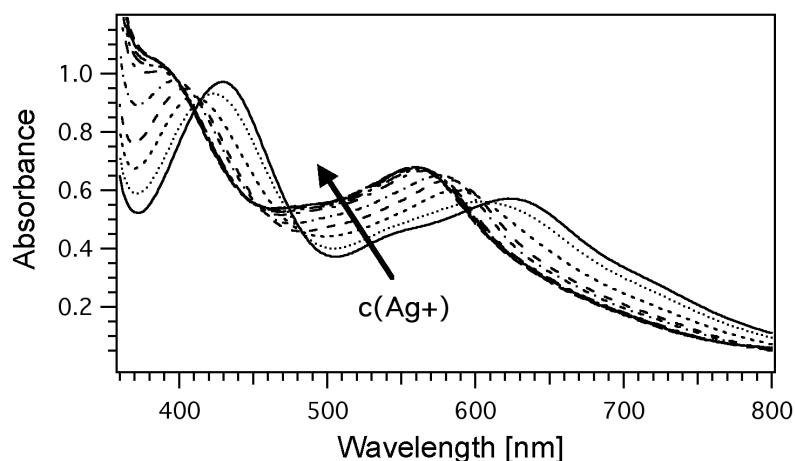
Figure 6.14: Titration of N749.2 with $AgNO_3$ solution under the same conditions as given for Figure 6.3 (in direction of arrow 0,0.1,0.25,0.5,0.75,1,1.25,1.5 dye mol equivalents of silver ions).

The vibrational $\nu(CN)$ band is shifted from 2106 cm^{-1} to 2143 cm^{-1} for N749 adsorbed onto TiO_2 in the presence of 0.5 dye equivalent $AgNO_3$. Again no evidence for the formation of silver carboxylate could be detected with UV/VIS and FTIR spectroscopy.

Devices that were dyed in presence of silver showed 50 % more current than the reference devices. Interestingly the increase in open circuit potential upon silver treatment is only 5 % compared to the reference sample and therefore much less pronounced than for $(Bu_4N)_2[Ru(dcbpyH)_2(NCS)_2]$ sensitised devices. Due to the bulky structure of the terpy ligand, the silver assisted dye assembling on the TiO_2 surface seams to be less efficient than for the N719 dye and to have less influence on the recombination current. However, further experiments are necessary to optimise the dye/silver concentration ratio in the case of the black dye.

Device	J_{SC} (mA/cm^2)	U_{OC} (mV)	FF (%)	η (%)
reference	2.6	662	0.69	1.24
silver modified sample	3.9	694	0.68	1.95

Table 6.4: Photovoltaic performance for device with and without silver.

6.5.2   <u>Variation of Cation</u>

For the replacement of the silver ion, other metal ions have to be found which are soft acids and which coordinate preferably to the sulphur. The corresponding metal salt needs to be soluble in the dye solution and must not interfere photochemically and electrochemically with the dye uptake process or with the photovoltaic process. A look at the periodic table of elements is useful for the selection of metal ions based on the HSAB concept: Generally speaking, regardless of oxidation state or geometry, all of the metals in the first transition series, and all of the lanthanides and actinides exhibit only N-coordination. The first half of the second and third transition series also tend to be N-coordinated whereas at Rh(III) Ir(I), there is a switch to S-coordination. Since many systems are intermediate, and behaviour can be influenced by other coordinated ligands or even non-coordinating ions, the expected bonding in a given case is not always predictable. The two other members of the group 11 metal(I) ions react in principle readily with sulphur ligands. However, copper(I) is easily oxidised to the +2 oxidation state, and gold(I) is known for its tendency to disproportionate into Au(III) and Au(0). Based on these considerations, salts of Hg^+, Pd^{2+}, Cd^{2+}, Pt^{2+} and Hg^{2+}were selected with respect to their potential coordination to the N_3 dye by means of UV/VIS and FTIR spectroscopy. The application of $Cd(NO_3)_2$, $PdCl_2$ and $HgCl_2$ provoked a spectral blue shift, varying from 8 nm for the cadmium salt to 20 nm for the Hg salt. Spectral shifts similar to the application of silver ions were observed for the palladium salt. As expected from the HSAB concept, no spectral shift in UV/VIS or IR could be observed for $Pb(NO_3)_2$ and $Zn(NO_3)_2$ salts, which contain metal cations of intermediate character.

Considering only the HSAB criteria regarding possible coordination to the dye is however not conclusive. For example, Pt^{2+} which should easily coordinate to the SCN ligand did not provoke any spectral change. Similarly Pd^{2+} only leads to a relatively small spectral shift in the FTIR spectrum, compared to the silver complex. Steric and electronic factors may hinder the complex formation or may be responsible that the complex formation requires special reaction conditions rather than combining dye and metal in solution at room temperature. In this respect silver ions are of advantage due to their relative large ionic radius radius[*] and their tendency to form complexes of larg binding angles. AgSCN is for example suggested to have a chain structure with a binding angle N-Ag-S close to 180°.[50] Recently staircase-like thiocyanate chains have been shown to form two-dimensional networks.[51] In terms of a simple co-adsorption experiment it is therefore difficult to replace the silver ions by other metal cations. With an adapted synthesis routine it should however be possible to produce an interconnection of dye molecules based on the discussed soft metal centres.

---

[*] ionic radius of Ag^+:113 pm, compared to 86 pm for Pd^{2+} and 85 pm for Pt^{2+}[49]

6.5.3   <u>Variation of Redox Mediator</u>

Based on previous experiments, the beneficial effect of the silver ions can be assigned to a modification of the dye. However, the silver ions might also alter the dye regeneration process. The coordination of the silver ions is stabilizing the t2g orbital of the regeneration and might at the same time also increase the driving force for the dye regeneration. A doping of the spiro-MeOTAD due to contact with the silver modified dye is very unlikely, as spiro-MeOTAD solution containing 5 mol% $AgNO_3$ did not show any spectral change characteristic for the hole conductor radical cation. The effect of silver was further studied by replacing the spiro-MeOTAD by an electrolyte system, containing the one-electron redox mediator cobalt(II)-bis[2,6-bis(1'-butylbenzimidazol-2'-yl)pyridine].[52] The cobalt complex is typically used in combination with hydrophobic dyes, rather than with N3 or N719. In the present case $N3\_C_9$ was used. Photovoltaic characterisation of this type of DSSC at AM1.5 shows a photon-to-electron conversion efficiency of 3 % for the reference device, whereas the silver sample performs with an efficiency of 4 %. The efficiency improvement is again mainly the result of increased short circuit current, which is up to 60 % higher for the silver device than for the reference device. The open circuit potential is only increased by 5 % for the silver device, which might be due to the application of neutral dye molecule (see chapter 6.5.1). The study of silver ions in devices based on the cobalt redox mediator is only at an initial state and is the subject of ongoing research.[*]

Due to the interaction of the silver cations with the iodide, the silver modification of the dye is not directly applicable in classical electrolyte solar cells based on the I_3^-/I^- redox mediator. The interaction of the iodide with the silver is expected to passivate the redox mediator. However, an improvement in I_{SC} of about 10 % for the classical DSSC were measured, when rinsing the TiO_2, dyed in presence of silver ions, with iodide solution prior to the application of the electrolyte. No effect of this treatment on the U_{OC} of the corresponding DSSCs was observed. The influence of the silver ions on the current output was much more depending on the composition of the hole transporting medium in the DSSC than in the SSD. The experiments with the electrolyte cells were derived in order to clarify to what extent the silver modification is related to the spiro-MeOTAD. As the preparation of DSSC is beyond the scope of the present work, no systematic studies were performed to adapt the silver modification to the conditions in the electrolyte cell.

---

[*] PhD Thesis Hervé Nusbaumer, for structure of complex compare appendix A.1

6.6 Conclusions

• Silver ions introduced into a dye solution of the N3 type were incorporated into the dye surface layer during the dye uptake. By means of ATR-FTIR spectroscopy and UV/VIS it could be shown that the silver ions coordinate to the ambidentate thiocyanate ligand. The shift of the $\nu(CN)$ mode to higher energies for the silver modified dye was attributed to the increased probability of the mesomeric structure containing a triple bond. The spectral blue shift of the electronic spectra of the silver-dye complex was interpreted in terms of a lowering of the dye HOMO orbital, which is shared by the Ru metal and the NCS ligands. These spectral changes upon silver modification were obtained for a variety of ruthenium metal organic dye molecules containing thiocyanate ligands.

• The silver modification of the dye was found to increase the dye uptake by 38 % and offers therefore a simple method to increase light harvesting while maintaining the TiO_2 layer thickness. The overall device efficiency of the SSD was significantly enhanced to 3.2 % at AM1.5, as a result of simultaneous increase in short circuit current and open circuit voltage. From spectroscopic and photovoltaic experiments the optimum silver concentration was found to be 0.5 dye mole equivalents.

• The increased short circuit currents upon silver modification were attributed to the increased dye uptake. Silver ions were found to function as bridging element between two thiocyanate ligands. The dye interaction via the silver ions is expected to assist the dye assembling on the TiO_2 surface. Accordingly the smaller footprint of the dye molecule allows more dye molecules to be adsorbed. The significantly increased U_{OC} in the presence of silver ions was assigned to a decreased interfacial charge recombination. The high density of the dye molecule layer bearing the silver cations is expected to block the electron back transfer from the TiO_2 to the spiro-MeOTAD cation. Silver ions were furthermore found to screen the electric field emerging from the adsorption of a negative dye such as N719.

• The silver coordination of the dye on the surface was completely reversible by washing the dye-sensitised TiO_2 film with an iodide solution in acetonitrile. This was evident from the UV/VIS and FTIR spectra of the dye after the iodide treatment.

• The beneficial influence of the silver co-adsorption on the photovoltaic performance is not limited to the spiro-MeOTAD. A similar improvement of the I_{SC} was also observed using the electrolyte redox mediator cobalt(II)-bis[2,6-bis(1'-butylbenzimidazol-2'-yl)pyridine].

6.7 References

[1] G. Smestad, S. Spiekermann, J. Kowalikc, et al. *Sol Energ Mat Sol C* **2003**, *76*, 85–105.

[2] U. Bach. Ph.D. Thesis, EPFL, 2000.

[3] B. ORegan, F. Lenzmann, R. Muis, et al. *Chem Mater* **2002**, *14*, 5023-5029.

[4] A. Kay, R. anHumphry-Baker and M. Grätzel. *J Phys Chem* **1994**, *98*, 952-959.

[5] G. P. Smestad and M. Grätzel. *J Chem Educ* **1998**, *75*, 752-756.

[6] F. Nüesch, J. E. Moser, V. Shklover, et al. *J Am Chem Soc* **1996**, *118*, 5420-5431.

[7] F. A. Nüesch. Ph.D. Thesis, EPFL, 1995.

[8] D. Kuciauskas, M. S. Freund, H.B. Gray, et al. *J Phys Chem B* **2001**, *105*, 392-403.

[9] G. Sauve´, M. E. Cass, S. J. Doig, et al. *J Phys Chem B* **2000**, *104*, 488-3491.

[10] O. Kohle. Ph.D. Thesis, EPFL, 1996.

[11] M. K. Nazeeruddin, P. Liska, J. Moser, et al. *Helv Chim Acta* **1990**, *73*, 1788-1803.

[12] M. Fleischmann, P. J. Hendra and A. J. McQuillan. *Chem Phys Lett* **1974**, *26*, 153.

[13] M. Ihara, K. Tanaka, K. Sakaki, et al. *J Phys Chem B* **1997**, *101*, 5153-5157.

[14] X. Wang, H. Wen, T. J. He, et al. *Spectrochim Acta A* **1997**, *53*, 2495-2504.

[15] M. Campbell, S. Lecomte and W. Smith. *J Raman spectrosc* **1999**, *30*, 37-44.

[16] M. J. Edmiston and R. D. Peacock. *Spectrochim Acta A* **1996**, *52*, 191-198.

[17] M. J. Edmiston and R. D. Peacock. *Spectrochim Acta A* **1993**, *49*, 1481-1486.

[18] J. A. Creighton, C. G. Blatchford and M. G. Albrecht. *J Chem Soc, Faraday T* **1979**, *2*, 790.

[19] G. Compagnini, B. Pignataro and B. Pelligra. *Chem Phys Lett* **1997**, *272*, 453.

[20] N. Shirtcliffe, U. Nickel and S. Schneider. *J Colloid Interface Sci* **1999**, *211*, 122-129.

[21] R. G. Pearson. *J Am Chem Soc* **1963**, *85*, 3533.

[22] R. G. Pearson. survey of progress in chemistry; A. Scott, Ed.; Academic Press: New York, 1969.

[23] T. H. James. The Theory of the photographic process; 4 ed.; Macmillan Publishing Co., Inc.: New York, 1977.

[24] J. Demas and J. Addington. *J Amer Chem Soc* **1974**, *96*, 3553.

[25] S. Peterson and J. Demas. *J Am Chem Soc* **1979**, *101*, 6571.

[26] S. Peterson and J. Demas. *J Am Chem Soc* **1976**, *98*, 24.

[27] H. Rensmo, S. Lunell and H. Siegbahn. *J Photochem Photobio A* **1998**, *114*, 117-124.

[28] A. Hagfeldt and M. Grätzel. *Acc Chem Res* **2000**, *33*, 269-277.

[29] V. Palaniappan, S. Sathaiah, H. D. Bist, et al. *J Am Chem Soc* **1988**, *110*, 6403-6410.

[30] O. Kohle, M. Grätzel, A. F. Meyer, et al. *Adv Mater* **1997**, *9*, 904.

[31] S. Das and P. V. Kamat. *J Phys Chem B* **1998**, *102*, 8954-8957.

[32] H. Greijer, J. Lindgren and A. Hagfeldt. *J Phys Chem B* **2001**, *105*, 6314-6320.

[33] M. K. Nazeeruddin, A. Kay, I. Rodicio, et al. *J Am Chem Soc* **1993**, *115*, 6382-6390.

[34] T. J. Meyer. *Pure Appl Chem* **1986**, *58*, 1193.

[35] N. S. Hush. *Trans Farad Soc* **1961**, *8*, 391.

[36] C. Creutz. *Prog Inorg Chem* **1983**, *30*, 1.

[37] M. K. Nazeeruddin, S. M. Zakeeruddin, R. Humphry-Baker, et al. *Inorg Chem* **1999**, *38*, 6298-6305.

[38] M. K. Nazeeruddin, M. Amirnasr, P. Comte, et al. *Langmuir* **2000**, *16*, 8525-8528.

[39] K. S. Finnie, J. R. Bartlett and J. L. Woolfrey. *Langmuir* **1998**, *14*, 2744-2749.

[40] K. Murakoshi, G. Kano, Y. Wada, et al. *J Electronanal Chem* **1995**, *396*, 27.

[41] G. Deacon and R. Philips. *Coord Chem Rev* **1980**, *33*, 227.

[42] T. Meyer, G. J. Meyer, B. W. Pfennig, et al. *Inorg Chem* **1994**, *33*, 3952.

[43] J. F. Moulder, W. F. Stickle, P. E. Sobol, et al. Handbook of X-ray Photoelectron Spectroscopy. *Perkin-Elmer Corporation*; E. Prairie, Ed. Minnesota, 1992.

[44] M. G. Kinnaird and D. G. Whitten. *Chem Phys Lett* **1982**, *88*, 275.

[45] C. Wen, K. Ishikawa, M. Kishima, et al. *Sol Energ Mat Sol C* **2000**, *61*, 339-351.

[46] M. Westphalen, U. Kreibig, J. Rostalski, et al. *Sol Energ Mat Sol C* **2000**, *61*, 97-105.

[47] M. K. Nazeeruddin, P. Péchy and M. Grätzel. *Chem Communn* **1997**, *18*, 1705-1706.

[48] M. K. Nazeeruddin, P. Pechy, T. Renouard, et al. *J Am Chem Soc* **2001**, *123*, 1613-1624.

[49] www.uniterra.de/rutherford/ng8.htm.

[50] F. A. Cotton and G. Wilkinson. Advance Inorganic Chemistry; 5 ed.; Wiley-Interscience, Ed. Singapore, 1988.

[51] C.-X. Ren, H.-L. Zhu, G. Yang, et al. *J Chem Soc, Dalton T* **2001**, 85-90.

[52] H. Nusbaumer, J.-E. Moser, S. M. Zakeeruddin, et al. *J Phys Chem B* **2001**, *105*, 10461-10464.

7 CHARACTERISATION OF SSD

BY FREQUENCY RESOLVED TECHNIQUES

Photoelectrochemical impedance spectroscopy (PEIS) at short circuit and open circuit potential were performed. The measurements under short circuit conditions were established in order to derive information about the electronic boundaries of the cell. The data obtained at open circuit potential provides information about the interfaces and charge transport in the SSD. The charge transport in the dye sensitised TiO_2 and at the heterojunction was further characterised employing Intensity modulated photocurrent spectroscopy (IMPS) and intensity modulated photovoltage spectroscopy (IMVS). The IMPS and the IMVS response of the SSD as function of the incident light intensity was determined and compared with electrolyte cell. IMPS data are fitted to a macroscopic diffusion model in order to derive values for the diffusion coefficient of photoinjected electrons.

7.1 Introduction

Although many features of photoprocesses can be studied with steady-state techniques, the information on dynamic processes such as of charge transport is limited. In this context it is useful to complement the study of the SSD with frequency resolved perturbation techniques. A comprehensive study of the dye-sensitised solar cell by PEIS has been established by Shaw[1] who measured PEIS spectra for a wide range of potentials and light intensities. Kern used PEIS in combination with IMVS to study the long-term stability of dye-sensitised solar cells.[2] Instead of simple equivalent circuits he developed a model based on RC elements for the cell boundaries and the electrolyte and differential equations for the electron transport and the recombination in the nanocrystalline TiO_2. Impedance spectroscopy for the study of solid-state dye-sensitised only recently found application: Longo et al. presented the PEIS study of a dye-sensitised device based on a polymer

electroyte.[3] Employing PEIS at open circuit potential and in the dark Kron et al.[4] have established a comparative study of DSSC and SSD based on spiro-MeOTAD. Both Longo and Kron made use of mathematical modified circuit elements, such as constant phase elements to analyse their data.

In particularly optical impedance spectroscopy has been proven a useful technique to study photoelectrochemical kinetics of semiconductor-electrolyte contacts, such as majority carrier injection into the semiconductor, charge separation at interfaces and transport and recombination processes.[5-10] A lot of pioneer work in the field of IMPS was established by Ponomarev.[11,12] The first extensive studies of dye-sensitised solar cells using IMPS and IMVS have been performed by Peter[13-18] and by Schlichthörl.[19,20] A variety of models based on charge transport by diffusion were developed which differ i.a. in the treatment of charge trapping.[17,21-25]

To date only a few PEIS or optical impedance spectroscopy studies on solid-state or quasi solid-state dye-sensitised solar cell have been published. The solid state however can cause some technical problems: a three-electrode setup, with a defined reference electrode to control the potential in the device is much more complicated to set up than in the electrolyte system. The investigation of a single interface in a symmetric device might be impossible due to technical problems, such as bad wettability of a gold layer by the hole conductor solution. Furthermore the junction obtained by spin-coating a solution of spiro-MeOTAD onto a substrate is mechanically different from the junction resulting from the deposition of a electrode material on top of a already dried spiro-MeOTAD film. Experiments presented here were therefore restricted to short circuit and open circuit potential.

7.2 PEIS Measurements at Open Circuit Potential

In the dark undoped TiO_2 is an isolator. Upon illumination, photodoping is occurring and a reasonable conductivity can be measured.[*] Under short circuit, the excess electron concentration at the TCO is zero, while in the TiO_2 an electron concentration gradient exists, which makes electron transport highly dependent on the location of the electron generation in the mesoporous network. Due to the high resistance, PEIS measurements under short circuit conditions just show the characteristics of the electrode boundaries, unless the illumination intensity is very high. The application of a forward bias to the working electrode, however, produces a gradient in the Fermi level across the TiO_2 film. This gradient provides a driving force for the diffusion of photoinjected electrons towards the TiO_2/HC interface,

---

[*] The electron concentration is about $10^5\,cm^{-3}$ in the dark[26] and 10^{17}-$10^{18}\,cm^{-3}$ under illumination with 100 W/m^2.

resulting in an equilibration between electron generation and recombination of photogenerated electrons with hole conductor radical cations. For constant light intensity and at open circuit potential, the Fermi level at the TCO/TiO_2 interface and across the TiO_2 film is constant for homogeneously absorbed light.

Equivalent Electronic Circuit for the SSD

For the analysis of the measured PEIS spectra an equivalent circuit was defined, which simulates physical processes resulting in measurable impedance with linear electronic elements. This is a simplified approach, as internal processes of charge recombination and charge transfer across the continuous TiO_2/HC interface can only approximately be represented by discrete electronic elements, such as a resistor and capacitor pair. Due to the interpenetrating network of the nanocrystalline TiO_2 and the hole conductor it is not straightforward to determine distinct interfaces that can be described independently. For the porous TiO_2/electrolyte interface so called interface transmission line models[27-29] have been developed to address the complexity of the medium at a microscopic level and to enable the characterisation of relaxation processes. Depressed semicircles in the complex plane, indicative for multiple time constants are often encountered as capacitive dispersion and are described with constant phase elements instead of capacitors. In the present analysis details of the porous structure are omitted and the dye-sensitised TiO_2 with the spiro-MeOTAD inside the pores is treated as a pseudo homogeneous system, which is embedded between the TCO and the metallic contact. The variety of interfaces on the microscopic level is represented as a combined macroscopic interface between the TiO_2 and the organic hole conductor. The charge transfer across the TiO_2/hole conductor interface at open circuit potential corresponds to recombination of photogenerated electrons with hole conductor radical cations. This heterojunction can be modeled as a pn-junction, i.e. a diode, which can be simulated by a parallel combination of a space charge layer capacitance C_{SC} and a charge transfer resistance R_{CT}. Charge can furthermore be stored in surface trap states (C_{ss}), which are of great important due to the porous character of the TiO_2. Recombination of electrons was shown to occur predominantly via trap states rather than via the conduction band.[19] For the modelling C_{SC} has therefore been replaced by $C_{CT}= (C_{SC}^{-1}+ C_{ss}^{-1})^{-1}$. In the present case the C_{SC} and C_{ss} cannot be distinguished experimentally although C_{ss} is expected to dominate the frequency response.

Characteristic for amorphous and disordered semiconductors such as spiro-MeOTAD is the high density of trap states which correlate with the doping level of the material. The property of the hole conductor to transport charge and to store charge is represented in the parallel connection of the charge transport resistance R_{HC} and a trap state capacitance C_{HC}.

Figure 7.1 illustrates schematically the arrangement of discrete elements of the equivalent circuit. From the SEM picture in Figure 7.1 it is evident that the composite of TiO_2 and hole conductor is not in direct contact with the gold counter electrode. The device profile is therefore geometrically symmetric: towards the TCO the TiO_2/hole conductor composite forms an interface with the compact TiO_2 layer and against the gold counter electrode it is isolated by a layer of hole conductor. Therefore a TCO/hole conductor interface does not exist and does not need to be considered. The interface between the gold counter electrode and the pure hole conductor yields another parallel combination of a charge transfer resistance R_{CE} and a space charge layer capacitance C_{CE}, taking into account that this interface is not perfectly ohmic. Measurements of the workfunction of TiO_2 and SnO_2:F showed that the TiO_2/TCO interface is ohmic.[30] The same is assumed for the interface between the compact TiO_2 and the composite as well as for the interface between the composite and the spiro-MeOTAD. To simplify the discussion the faraday charge transfer processes are summarised in a lumped resistance $R_B = R_{TiO2} + R_{TiO2/composite} + R_{composite/spiro-MeOTAD}$.
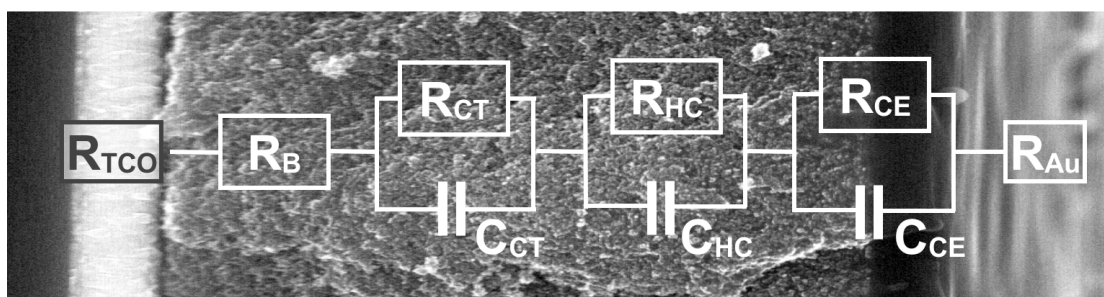
Figure 7.1: Equivalent circuit for the SSD at open circuit potential and under illumination. C_{CT}: charge transfer capacitance of heterojunction, C_{HC}: hole conductor trap state capacitance, C_{CE}: space charge layer capacitance of interface between the gold counter electrode and HC, R_{CTO}: resistance of TCO, R_B: lumped resistance (compare text), R_{CT}: charge transfer resistance of heterojunction, R_{HC}: resistance of hole conductor, R_{CE}: charge transfer resistance of interface between the gold counter electrode and HC, R_{Au}: resistance of gold electrode.

Based on this macroscopic model an impedance spectrum is expected to contain up to three semicircles in the Nyquist Plot. The high frequency arc is supposed to be shifted from the origin of the complex plane by $R = R_B + R_{CTO} + R_{Au}$.

Figure 7.2 shows a typical PEIS spectrum for the SSD device. Only two arcs, a large flattened one at intermediate frequencies, and a smaller at high frequencies can be observed in the Nyquist Plot. The two time constants are better resolved in the Bode Plots.

All measurements were done under comparable illumination conditions as for the optical impedance studies in order to allow a comparison of the different experiments.
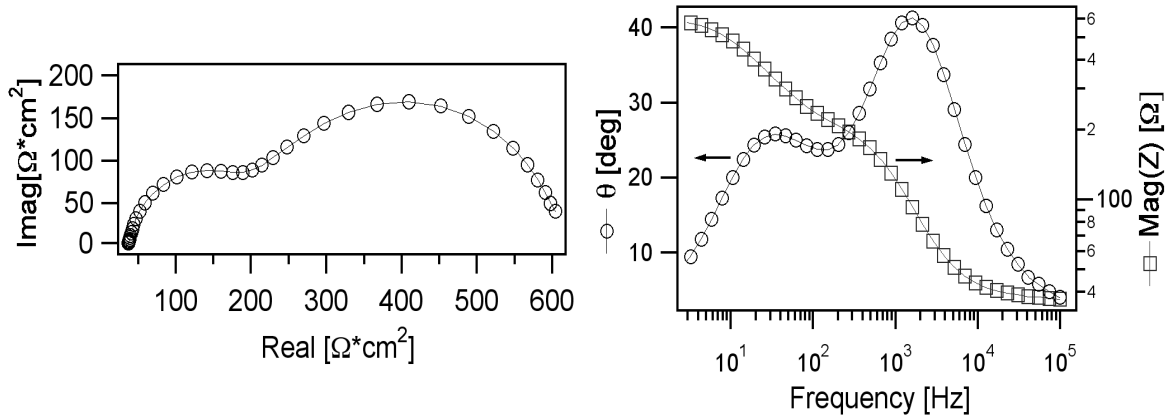

Figure 7.2: Typical Nyquist and Bode Plots at open circuit potential ($I_0 = 2 \cdot 10^{15}$ cm^{-2}s^{-1})

In order to identify the response related to the interface of the dye-sensitised TiO$_2$ with the hole conductor, PEIS and IMVS data were compared. Figure 7.3 shows the imaginary component of the IMVS and PEIS response at open circuit for the same cell and light intensity. Both spectra coincide for the frequency region around 10 Hz, which implies that the response in this frequency range is determined by the charge transport via the heterojunction. Accordingly the high frequency signal can be assigned to the charge transport in the hole conductor. The high frequency intercept with the real axis in the Nyquist plot shows a value of about 35 Ω which corresponds to the cell resistance value obtained from DC current-voltage characteristics.
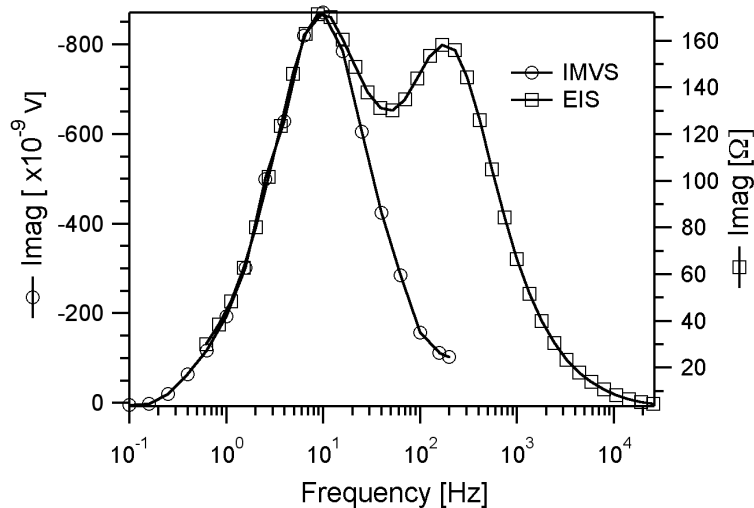
Figure 7.3: Imaginary part of the PEIS measured at open circuit potential and the IMVS measurement for the same cell and under the same illumination conditions as in Figure 7.2.

Comparison of Different Hole Conductor Matrix Compositions

PEIS measurements at open circuit potential have been employed to study the impact of different additives in the hole-conducting medium on the electronic properties of the device. The presence of the three additives [N(p-C$_6$H$_4$Br)][SbCl$_6$] ("doping"), Li(CF$_3$SO$_2$)$_2$N ("Li$^+$") and tBP in the spiro-MeOTAD matrix has been altered, while keeping the concentration of each component in the spin-coating solution constant for all samples. The variation of the hole conductor composition and the possible device comparisons are summarised in Figure 7.4. The influence of the different additives on the PEIS spectrum is evident from Figure 7.5:
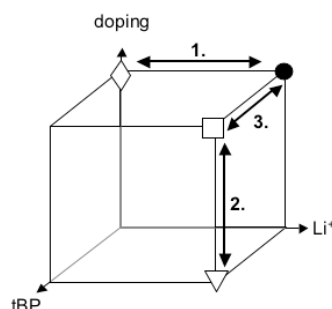
Figure 7.4: Scheme to summarise the variation of composition of the hole conductor film. The missing compositions for a complete measuring matrix (3 parameters, 8 combinations) resulted either in very low current devices or in bad hole conductor films (for example Li(CF$_3$SO$_2$)$_2$N as only additive leads to very bad hole conductor films).
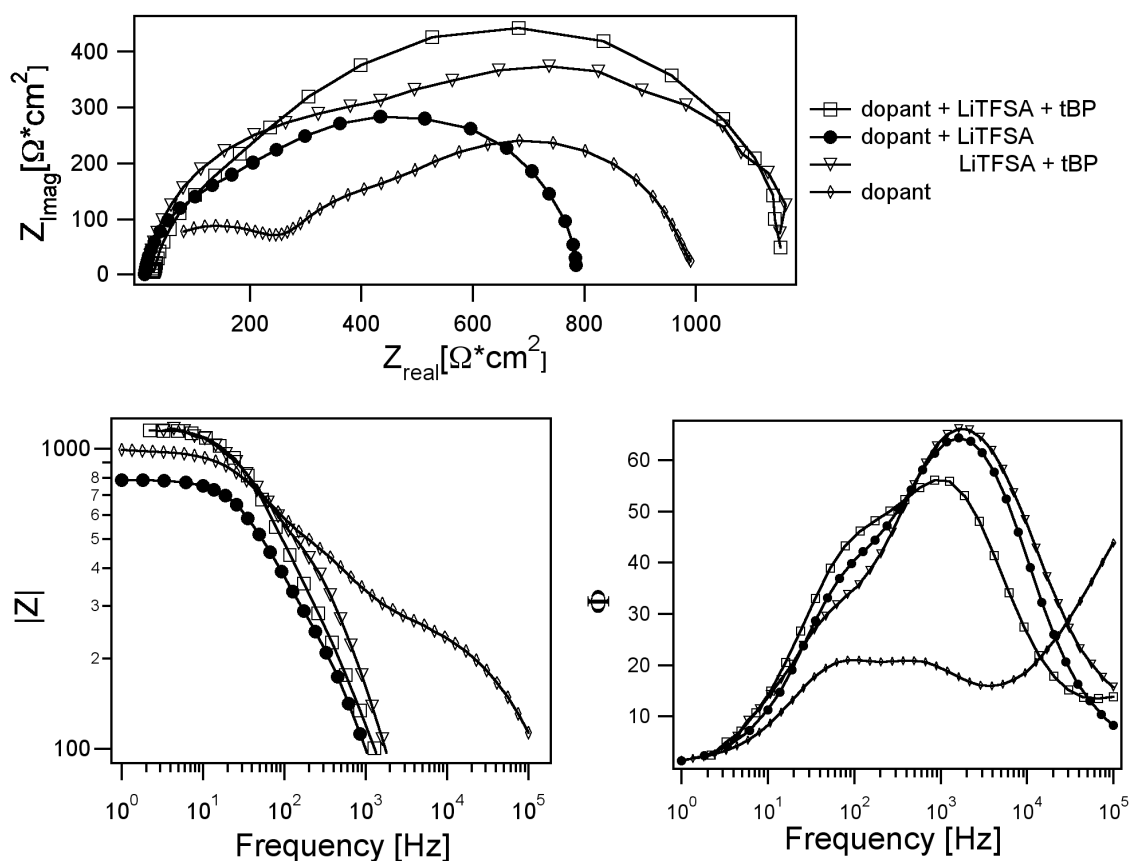
Figure 7.5 Nyquist and Bode PEIS plots for SSD of different hole conductor composition at open circuit potential and under illumination ($I_o=10^{16}$ cm^{-2}s^{-1}). The concentration of the different additives in the spin-coating solution was 0.1 M *spiro*-MeOTAD, 14 mM LiTFSA, 0.4 mM dopant and 0.16 M tBP.

1. *Effect of LiTFSA in presence of dopant:*

The PEIS spectrum of the SSD containing only dopant shows three semicircles, with frequency maxima at around 41 kHz, 493 Hz and 46 Hz. In the presence of LiTFSA in the spiro-MeOTAD the high frequency semicircle is not detectable anymore. Similarly no high frequency signal could be resolved for the other lithium ion containing SSDs.

Without lithium in the hole conductor matrix the arcs are much better defined and the impedance is higher for all frequencies, in particular for the high frequency region. Fitting the spectra to the equivalent circuit discussed above, a very small capacitance of 1.43*10-8 F and a high resistance value of 270 ohm are obtained for the high frequency arc. The small value of the capacity makes it likely to assign the high frequency arc to the charge transport via the Au/HC interface. The fact that all samples were measured under the same conditions, but only the sample without lithium ions shows the signal at high frequencies, justifies the conclusion that the low capacitance is caused by a real interface and not by a stray capacitance. The lithium ions are therefore not only affecting the TiO$_2$/HC interface but also the interface of the hole conductor with the gold counter electrode.

PEIS measurements of a cell consisting of two gold electrodes with the spiro-MeOTAD in between were impossible due to technical problems: the spin-coating of spiro-MeOTAD solution on top of a gold film is impossible because of a poor wettability of the gold by the solution. A deposition of spiro-MeOTAD by thermal evaporation leads to the degradation of the hole conductor.[*] The preparation of a freestanding organic film and the mechanical contact formation with gold electrodes was also not successful. Therefore the assignment of the high frequency arc to the spiro-MeOTAD/Au interface cannot be proven directly.

2. *Effect of dopant in presence of tBP and LiTFSA*

In the presence of tBP and lithium ions, the dopant causes a decrease of the phase shift and the impedance value for the high frequency signal. Simultaneously, upon doping the low frequency arc has a maximum at a slightly higher frequency than for the SSD without doping (36 Hz compared to 26 Hz). The oxidative doping of the spiro-MeOTAD film provokes an overlaying of the semicircles in the Niquist plot and makes the interpretation of the influence of the doping on an individual element in the equivalent circuit difficult. The Bode Plot implies a stronger influence of the doping on the high frequency peak which agrees with its assignment to the charge transport in the hole conductor film.

---

[*] Personnel communication Dr. H. Spreitzer and K. Cloedt

3.   *Effect of tBP in presence of LiTFSA and dopant*

tBP causes the impedance to increase over the whole frequency range. As described previously, tBP is expected to hinder the recombination via the TiO_2/HC interface, which correlates to a higher impedance for the corresponding frequency region. Low and high frequency peaks are shifted from 49 to 36 Hz, respectively from 452 to 386 Hz upon introduction of tBP into the hole conductor matrix. The measured effect is rather small compared to the overall improvement in device performance, confirming the assumption that tBP affects the SSD not only by the blocking of surface states.

Comparison with the DSSC

Up to three time constants, resulting in three semicircles in the complex plane were reported by different authors for the DSSC employing PEIS under illumination and at open circuit potential.[1,2,21,31,32] Depending on the composition of the studied cell and the measuring conditions the three time constants are more or less distinguished, although in some cases two time constants are very similar, leading to an overlapping of arcs in the Nyquist plot. In particular the low–frequency signal is often disguised by the middle frequency response of the cell. The frequency peak in the low-frequency range (mHz) was correlated with the Nernst diffusion within the electrolyte.[2,21] The time constant in the range from 10-100 Hz was identified with the electrochemical processes at the TiO_2/electrolyte interface and the signal at high frequencies in the kHz region to the charge-transfer at the platinum counter electrode.

The direct comparison of the present impedance data with the literature values is difficult because of the different measuring conditions. However, the influence of a specific parameter on the impedance spectrum for the two types of devices can be compared qualitatively. Similar effects as described above for the lithium salt containing hole conductor film have been found by Zaban,[33] who has investigated the electrical potential distribution in the nanocrystalline TiO_2 electrode. In this work the enhanced conductivity of the TiO_2 in the presence of lithium ions in the electrolyte has been assigned to a positive shift of the flat band potential and/or lithium intercalation. The change of the charge carrier concentration in the hole-transporting medium has an influence on the charge recombination at the surface of the TiO_2 and the charge transport in the electrolyte. This manifests itself in a shift of the corresponding frequency responses and can provoke their superposition. For the DSSC this effect has been studied by simulations of PEIS spectra for varying tri-iode concentrations.[34] The impedance and phase shift of the low frequency peak ("electrolyte") have been found to increase for decreasing tri-iodide concentration while the middle frequency peak ("TiO_2/Electrolyte") is shifted to lower frequencies (i.e. longer electron lifetimes). Similarly the

low and the medium frequency peak (i.e. "TiO_2/spiro-MeOTAD" and "spiro-MeOTAD") were found to overlay for doped film while separate arcs were observed for an undoped spiro-MeOTAD film. The application of tBP to the electrolyte in the DSSC provokes a shift of the mid-frequency peak to lower frequencies, which has been correlated to an increase of the lifetime by a factor of five.[2] The phase shift for the tBP sample is enhanced compared with the sample without tBP. While the tBP is also affecting the charge transport in the hole conductor, the low-frequency signal of the DSSC, which is representing the charge transport in the electrolyte, is only little altered.[2]

It is striking that the PEIS spectra for the SSD show rather high phase shifts, except for the sample without lithium ions, where phase shifts of only 20° were observed. This leads to the conclusion that the lithium ions provoke a shift of one time constant to higher values (lower frequencies), leading to the overlap of two frequency signals. On the other hand impedance studies on the electrolyte cell[1] have shown that the absolute value of the impedance and phase shift for the middle frequency signal ("TiO_2") decrease with increasing light intensity. PEIS spectra of the SSD at one Sun illumination showed indeed much lower phase shifts for all frequency regions. Similarly impedance and phase shift have been found to increase for decreasing layer thickness of the TiO_2.[34] Enhanced light intensity as well as thicker TiO_2 layers will increase the number of electrons injected (photodoping) and therefore the conductivity.

Effect of Silver Modification on the Impedance Spectra

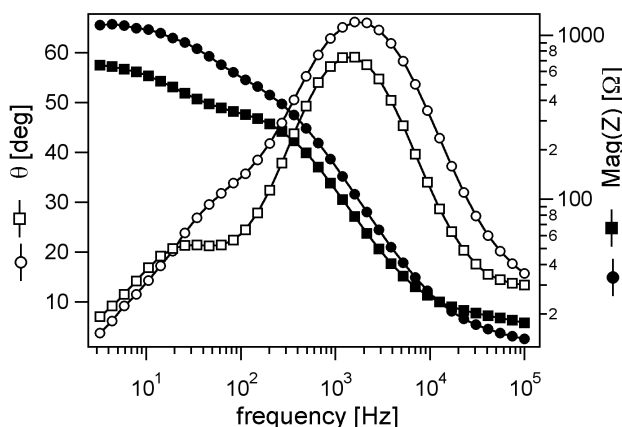Figure 7.6 compares the Bode spectra for SSDs with and without silver treatment (see also chapter 6).

Figure 7.6: PEIS spectrum measured under open circuit conditions and illumination for samples with (■, □) and without silver (●, ○).

The impedance of the silver treated sample is lower for the whole frequency range except for high frequencies over 10 kHz. The silver ions seem to affect in particular the TiO_2/HC interface, leading to a decreased phase shift and a shift of the frequency maximum from 35 Hz to 6 Hz. The decreased impedance in the presence of the silver ions is expected to result from the enhanced light harvesting which provokes a higher electron density in the TiO_2 (higher quasi Fermi level) compared to the reference device. Similarly the change of the high frequency signal upon silver modification is similar to the one discussed in Figure 7.5 upon device doping, indicating also a photodoping of the hole conductor due to increased hole injection from the dye in the presence of silver.

7.3 Optical Impedance

Although technically similar, the probing of external and internal parameters is different for optical and electronic impedance spectroscopy. The IMVS signal reflects the ratio of the voltage response to the modulated incident light intensity, while the PEIS response corresponds to the ratio of the modulated potential to the current density response. Correspondingly the modulation source is different: For the PEIS the position of the Fermi level is modulated by an external voltage source, whereas for the IMVS the Fermi level follows the modulation of the incident illumination. Accordingly, the IMVS spectrum is mainly determined by the response of the dye-sensitized TiO_2. The determination of lifetimes is therefore easier with IMVS than with PEIS, where overlapping of frequency features might complicate the analysis. IMPS and IMVS have been applied previously to study electrolyte-based dye-sensitised cells, where diffusive 'hole transport' by tri-iodide ions is facile, whereas electron transport in the TiO_2 appears to be slow and trap-controlled. One of the most striking features of the DSSC is the fact that their dynamic response becomes slower as the light intensity is reduced. This can be seen in the photocurrent and photovoltage responses to stepped illumination. The present study sets out to discover if the SSD exhibits a similar intensity dependence of the response time to the DSSC and whether electron (or hole) transport limits the device performance.

7.3.1   IMPS

IMPS measures the periodic photocurrent response to the superposition of a small sinusoidal perturbation of the light intensity on a larger steady background level and provides information about the dynamics of charge transport and back reaction under short circuit conditions. IMPS measurements were carried out over a range of illumination intensities of four orders of magnitude. Figure 7.7 illustrates a typical complex plane plot for the IMPS response at the highest light intensity used. The photocurrent lags behind the illumination, leading to a semicircle response in the fourth quadrant (positive real, negative imaginary) of the complex plane. In the absence of electron-hole recombination, the phase shift of the IMPS semicircle is a result of the time delay between the generation and collection of charge carriers. At low frequencies, the IMPS plots converge to a point on the real axis that corresponds to the steady state photocurrent. At high frequencies the modulated photocurrent approaches zero, indicating that the modulation frequency is faster than the relaxation of the charge carrier density by transport to the contacts and back reaction.
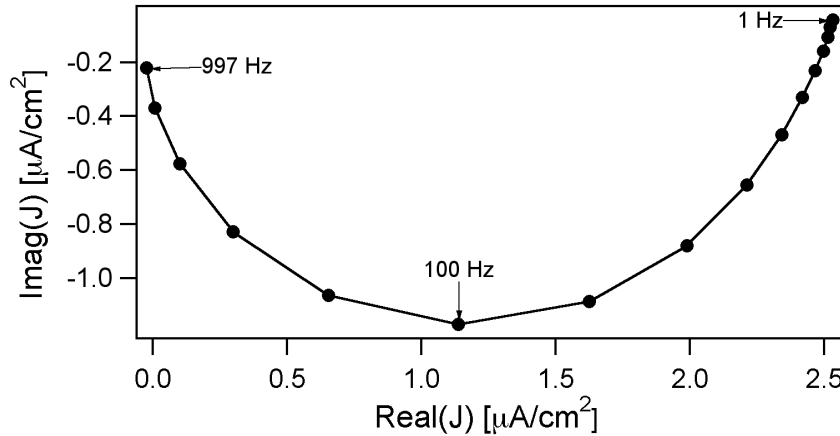
Figure 7.7: Typical IMPS response for a solid-state solar cell ($I_o = 1.9 \times 10^{15}$ cm^{-2} s^{-1})

The change in intensity of the incident illumination does not influence the shape of the IMPS curve. However, the frequency of the minima was observed to decrease with reduced light intensity. This decrease of the minimum frequency as function of the incident photon flux is depicted in Figure 7.8 in double logarithmic representation. A linear correlation is observed with a slope of 0.62. An order of magnitude estimate of the mean transit time for photogenerated electrons can be obtained from the frequency minimum in the IMPS complex plane plot: $\tau_d = (2 \pi f_{min}(IMPS))^{-1}$. At short circuit and for homogeneously absorbed light, the electron diffusion coefficient can be estimated from the relation $D_n = d^2/4 \, \tau_{IMPS}$, where d is the layer thickness of the nanocrystalline TiO_2.
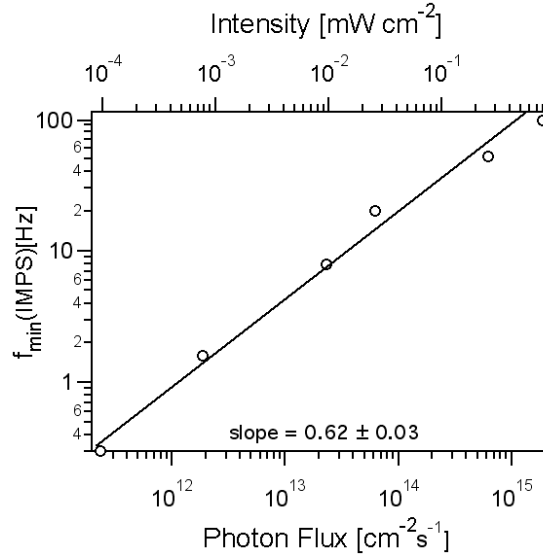
Figure 7.8: f_{min}(IMPS) as a function of the incident photon flux.

A more satisfactory approach to determine the diffusion coefficient is the fit of the IMPS data based on the model discussed in chapter 3 (Experimental Methods). Figure 7.9 compares examples of theoretical and experimental IMPS plots for a photon flux of $I_0=1.9 \times 10^{15}$ cm^{-2} s^{-1}.
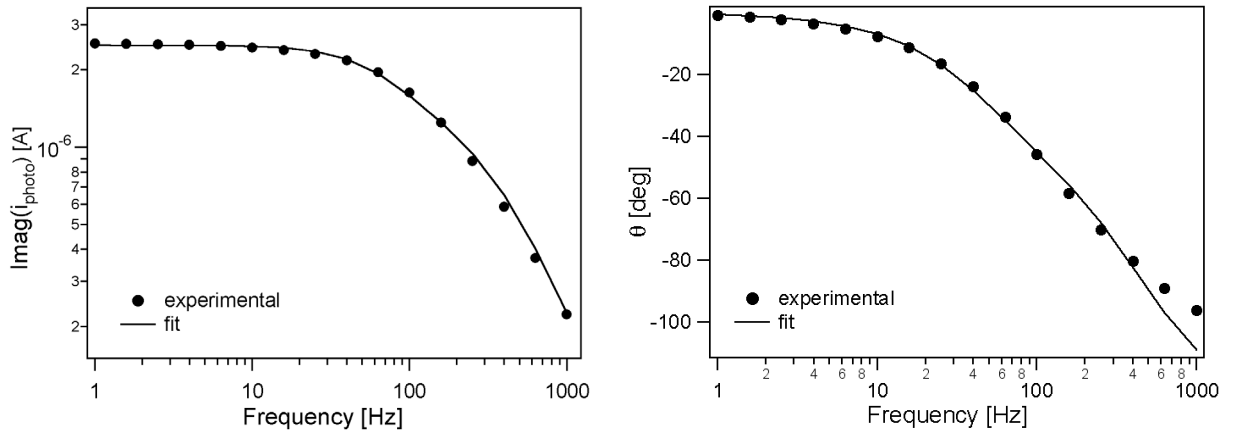

Figure 7.9: Short circuit IMPS response ($I_0=1.9*10^{15}$ cm^{-2} s^{-1}) represented in the form of Bode Plots ($\bullet$). The IMPS fit (Fit parameters: D_n = 3.6e-6 cm^{2}s^{-1}, τ_n = 4.5 ms, k_{ex} = 10^5, α = 2200 cm^{-1}, R=23 Ω, C=1.6 10^{-5} F) is shown as line (-).

The diffusion coefficients obtained from the fitted IMPS responses at different light intensities are summarised in Figure 7.10. The trend of the diffusion coefficient with light intensity is similar to the one reported for the DSSC where electron diffusion becomes faster with increasing light intensity.
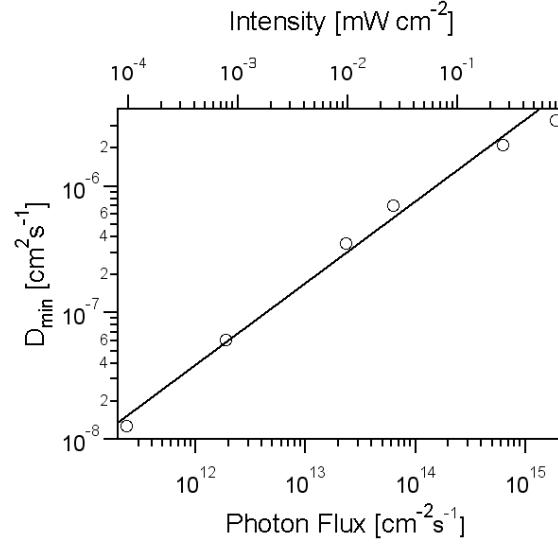
Figure 7.10: D_n as a function of the incident photon flux. D_n has been obtained fitting the IMPS responses for the different light intensities to a diffusion model developed by Dloczik et al.[17]

7.3.2   <u>IMVS</u>

The IMVS experiment corresponds to the modulation of the photovoltage (i.e. the difference in Fermi level in the dark E_F and the quasi Fermi level upon illumination $_nE_F$) in response to the modulation of incident light intensity. The IMVS response is related to the electron lifetime under open circuit conditions.

IMVS measurements were carried out over the same range of illumination intensities as the IMPS. Similarly to the behaviour of the photocurrent the photovoltage lags behind the illumination. Figure 7.11 illustrates a typical IMVS response in the fourth quadrant of the complex plane. The phase lag for the response is associated with the relaxation of electrons by back reaction with cations in the hole conductor matrix, which one may assume are in excess.
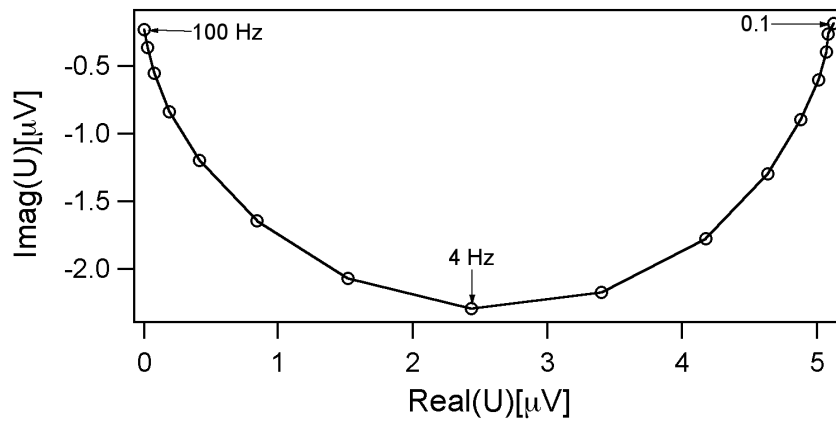

Figure 7.11: Typical IMVS response for a solid-state solar cell (I_o=1.9 $\times10^{15}$ cm^{-2} s^{-1})

The decrease of the minimum frequency as function of the incident photon flux is depicted in Figure 7.12 in double logarithmic representation, with a slope of 0.65. The electron lifetime can be obtained from the IMVS plot by setting $\tau_n = (2\,\pi\,f_{min}(IMVS))^{-1}$. Therefore the dependence of τ_n on the light intensity has the same slope as the $\log(f_{min}(IMVS))=f(\log(I_0))$ but with inverse sign. Comparison of the IMPS and IMVS responses shows that τ_n and τ_d differ at least by one order of magnitude, because of the transition from mixed diffusion/recombination control under short circuit to pure recombination control under open circuit conditions. Again the trend of the electron lifetime with light intensity (Figure 7.12) corresponds to that determined for the electrolyte cell, for which a decrease of the electron lifetime was found with increasing light intensity.
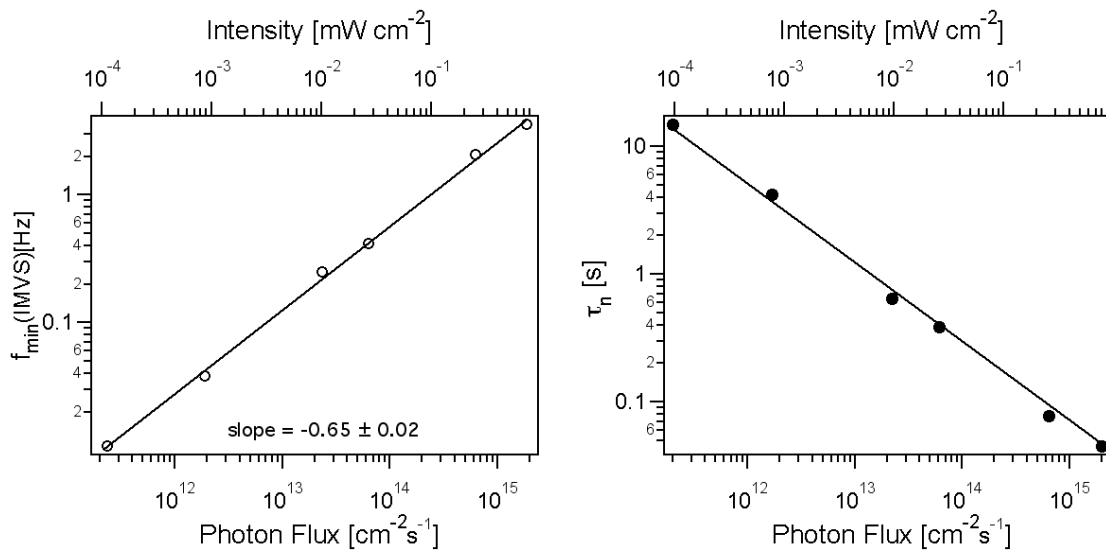

Figure 7.12: $f_{min}(IMVS)$ and $\tau_n(IMVS)$ as a function of the incident photon flux.

7.3.3   <u>Electron Diffusion Length</u>

A measure for back reaction of the injected electrons with the hole transporting material is the electron diffusion length $L_n=(D_n\tau_n)^{0.5}$. L_n has been determined using the diffusion coefficients obtained from the curve fit for the IMPS response at different light intensities and the electron lifetimes from the IMVS response for the same light intensity.[13,15,17] A value of about 4.4 μm has been obtained, which does not alter more than $\pm$ 0.09 μm over the whole range of measured intensities.

The diffusion length does not change with light intensity which arises from the fact that the electron lifetime and diffusion coefficient have nearly the same dependence on light intensity but with opposite sign. This suggests strongly that the rate-limiting steps in electron transport and in the back reaction are the same, namely trap limited hopping. In the case of

electrolyte cells, by contrast, the power laws describing the intensity dependences of the electron diffusion coefficient and lifetime do compensate each other exactly, so that the IPCE is only weakly intensity dependent. In this case, it seems likely that the back reaction of electrons with tri-iodide ions takes place under mixed kinetic/transport control. The electron diffusion length for electrolyte cells in the same light intensity range as that used in the present work has been reported to vary between 10 and 20 μm.[13] The smaller electron diffusion length in the present cells reflects the shorter electron lifetime in the solid-state cell compared with the electrolyte cell.

In the case of electrolyte cells, the variation of the diffusion coefficient with incident photon flux has been assigned to trap limited electron transport in the porous TiO_2.[17,35,36] In the dark under U_{OC} conditions the Fermi level and hence trap occupancy in TiO_2 particles is determined by electron exchange with the mediator. Under illumination the trap occupancy changes with the position of the quasi Fermi level for electrons. As the quasi Fermi level moves towards the conduction band with increasing light intensity, deep traps will be filled so that they no longer retard electron transport. Exchange with shallow traps is much faster, so that the effective diffusion rate becomes higher. The results obtained for the solid-state cell indicate that the mechanism of electron transport in the TiO_2 is the same as in the electrolyte cells for the range of light intensities investigated.

The electron lifetime for the I^-/I_3^- electrolyte cell has been found to vary with the inverse square root of the light intensity. This behaviour has been rationalised in terms of a two-step recombination reaction between electrons and tri-iodide, which is second order in electron concentration.[25] By contrast, spiro-MeOTAD is expected to behave as a one-electron redox system, so that the rate constant for the back reaction of electrons with holes should be first order and independent of light intensity. In fact, as discussed above, the results show a clear dependence of the recombination rate constant on the light intensity. Similar behaviour has been observed for other one-electron redox mediators, such as CuI and polyaniline.[37] This indicates that electron trapping may exert a significant effect on the rate constant for electron transfer. Nelson et al.[38] have suggested that trapping alone could lead to the recombination behaviour at low intensities observed in electrolyte cells. In the case of the solid-state cells, the back reaction certainly appears to be controlled by the rate of electron transport in the TiO_2 film rather than the transport properties of the hole transporting medium.

7.4 Conclusions

• PEIS measurements on SSD were performed under open circuit potential conditions and low light intensity. For the analysis of the measured spectra an equivalent circuit was defined that presents the physical processes in the form of discrete electronic elements. For the standard device with tBP and lithium ions in the spiro-MeOTAD, the Niquist plot contains two arcs at frequencies around 10 and 1000 Hz. By comparison with IMVS experiments the low frequency response could be assigned to the electron recombination processes at the TiO_2 surface. The high frequency semicircle represents the charge transport in the hole conducting material.

• Different hole conductor compositions were compared regarding the response in the PEIS experiment. Without lithium ions in the organic semiconductor, a third arc at high frequencies was detected, which was related to the interface of spiro-MeOTAD with the counter electrode. The variation of the additives in the hole-transporting medium confirmed the assignment of the impedance arcs to the interfaces of the device model.

• The present results were compared with published impedance data on DSSCs. The frequency responses corresponding to the charge transfer processes at the TiO_2/spiro-MeOTAD interface and the TiO_2/electrolyte interface were observed at similar frequencies. Depending on measurement conditions and device preparation the corresponding signals were found in a frequency region from 5-100 Hz. Similar trends for DSSC and SSD were also observed for the device modification with lithium ions or tBP.

• Values of the electron diffusion coefficient and electron lifetime in the SSD were derived from IMPS and IMVS measurements. The light intensity dependence of these parameters indicates that the transient response of the cell for less than 1 mW cm^{-2} appears to be dominated by electron transport in the TiO_2 rather than hole transport in the organic material. The rate constant for electron hole recombination is also intensity dependent, and the results show that recombination is controlled by electron transport in the TiO_2. An intensity independent electron diffusion length of 4.4 μm has been determined, which is by a factor of four lower than in the electrolyte cell but two times higher than the TiO_2 layer thickness. This indicates that electron collection in the cell is very efficient at low light intensities.

7.5 References

[1] N. Shaw. Ph.D. Thesis, University of Bath, 1999.

[2] R. Kern, N. Van Der Burg, G. Chmiel, et al. *Opto Electron Rev* **2000**, *8*, 284-288.

[3] C. Longo, A. F. Nogueira, M.-A. D. Paoli, et al. *J Phys Chem B* **2002**, *106*, 5925-5930.

[4] G. Kron, T. Egerter, G. Nelles, et al. *Thin Solid Films* **2002**, *403-404*, 242-246.

[5] D. J. Fermin, E. A. Ponomarev and L. M. Peter. *J Electroanal Chem* **1999**, *473*, 192-203.

[6] D. Vanmaekelbergh, A. R. Dewit and F. Cardon. *J Appl Phys* **1993**, *73*, 5049-5057.

[7] D. Vanmaekelbergh and F. Cardon. *Semicond Sci Technol* **1988**, *3*, 124-133.

[8] D. Vanmaekelbergh and F. Cardon. *Electrochim Acta* **1992**, *37*, 837-846.

[9] W. P. Gomes, D. Vanmaekelbergh and F. Cardon. *J Electrochem Soc* **1986**, *133*, C334-C334.

[10] D. Vanmaekelbergh and F. Cardon. *J Phys D Appl Phys* **1986**, *19*, 643-656.

[11] E. A. Ponomarev and L. M. Peter. *J Electroanal Chem* **1995**, *397*, 45-52.

[12] E. A. Ponomarev and L. M. Peter. *J Electroanal Chem* **1995**, *396*, 219-226.

[13] L. M. Peter and K. G. U. Wijayantha. *Electrochim Acta* **2000**, *45*, 4543–4551.

[14] A. C. Fisher, L. M. Peter, E. A. Ponomarev, et al. *J Phys Chem B* **2000**, *104*, 949-958.

[15] L. M. Peter and K. G. U. Wijayantha. *Electrochem Comm* **1999**, *1*, 576-580.

[16] G. Franco, L. M. Peter and E. A. Ponomarev. *Electroch Comm* **1999**, *1*, 61-64.

[17] L. Dloczik, O. Ileperuma, I. Lauermann, et al. *J Phys Chem B* **1997**, *101*, 10281-10289.

[18] L. M. Peter. *Philos T Roy Soc A* **1996**, *354*, 1613-1625.

[19] G. Schlichthörl, S. Y. Huang, J. Sprague, et al. *J Phys Chem B* **1997**, *101*, 8141-8155.

[20] G. Schlichthörl, N. G. Park and A. J. Frank. *J Phys Chem B* **1999**, *103*, 782-791.

[21] R. Kern, R. Sastrawan, J. Ferber, et al. *Electrochim Acta* **2002**, *47*, 4213- 4225.

[22] J. v. d. Lagemaat, N. Park and A. Frank. *J Phys Chem B* **2000**, *104*, 2044-2052.

[23] N. Kopidakis, E. A. Schiff, N. G. Park, et al. *J Phys Chem B* **2000**, *104*, 3930-3936.

[24] J. v. d. Lagemaat and A. J. Frank. *J Phys Chem B* **2001**, *105*, 11194-11205.

[25] S. Y. Huang, G. Schlichthörl, A. J. Nozik, et al. *J Phys Chem B* **1997**, *101*, 2576-2582.

[26] J. Ferber, R. Stangl and J. Luther. *Sol Energ Mat Sol C* **1998**, *53*, 29-54.

[27] J. Bisquert, G. Garcia-Belmonte, F. Fabregat-Santiago, et al. *J Phys Chem B* **2000**, *104*, 2287-2298.

[28] J. Bisquert, G. Garcia-Belmonte, F. Fabregat-Santiago, et al. *Electrochem Commun* **1999**, *1*, 429-435.

[29] J. Bisquert, G. Garcia-Belmonte, P. Bueno, et al. *J Electroanal Chem* **1998**, *452*, 229-234.

[30] D. Cahen, G. Hodes, M. Gratzel, et al. *J Phys Chem B* **2000**, *104*, 2053-2059.

[31] T. Hoshikawa, R. Kikuchi, K. Sasaki, et al. *Electrochemistry* **2002**, *70*, 675-680.

[32] T.-S. Kang, K.-H. Chun, J. S. Hong, et al. *J Electrochem Soc* **2000**, *147*, 3049-3053.

[33] A. Zaban, A. Meier and B. A. Gregg. *J Phys Chem B* **1997**, *101*, 7985-7990.

[34] R. Kern, Ph.D. Thesis Albert-Ludwigs-Universität Freiburg i. Brsg., 2001.

[35] P. E. d. Jongh and D. Vanmaekelbergh. *Phys Rev Lett* **1996**, *77*, 3427.

[36] P. E. d. Jongh and D. Vanmaekelbergh. *J Phys Chem B* **1997**, *101*, 2716.

[37] K. G. U. Wijayantha. Ph. D. Thesis, University of Bath, 2001.

[38] J. Nelson, S. A. Haque, D. R. Klug, et al. *Phys Rev B* **2001**, *6320*, 205321.

8 GENERAL CONCLUSIONS

The objective of the present work was to study performance limitations emerging from the replacement of the liquid hole-transporting medium with the amorphous organic semiconductor spiro-MeOTAD. The most important limitation in the SSD compared to the DSSC is the less efficient charge transport in the solid hole-transporting medium, resulting in resistive losses and increased interfacial charge recombination. From this, practical consequences emerge for the all device components:

Nanocrystalline TiO_2

• The layer thickness of TiO_2, which is an important parameter in order to increase the light harvesting of a device, cannot be increased at will due to mechanical and electronic limitations. Mechanical limitations include the film stability upon drying of the spiro-MeOTAD material in the pores and the decreasing pore filling of the TiO_2 network for increasing layer thickness. The electronic limitations are given by the increasing importance of resistive losses for increasing layer thickness. Moreover, for efficient electron collection, the TiO_2 film thickness needs to be smaller than the electron diffusion length, which is a function of the electron diffusion coefficient in the TiO_2 and the electron lifetime. Values of the electron diffusion coefficient and electron lifetime in the spiro-MeOTAD solid-state dye-sensitized solar cell have been derived from IMPS and IMVS measurements. An intensity independent electron diffusion length of 4.4 μm was determined for low light intensities, which is by a factor of four lower than in the electrolyte cell. Combining the experimental results regarding electronic and mechanical limitations an optimal layer thickness of 2.5 μm was found for a film of 69.3 % porosity and a specific surface area of 104 m^2/g, which contained particles of 15 nm.

Sensitiser

• The dye structure was found to play an important role in the formation of the heterojunction. In a dye hydrophobic series containing bpy ring with aliphatic chains of differing length, a correlation of the photovoltaic performances with the chain length of the aliphatic chain was observed. The effect was rationalised in terms of an improved wettability of the long-chain dye sensitised TiO_2 by the organic hole conductor.

• The modification of ruthenium sensitisers containing thiocyanate ligand with silver ions enabled to profit from the advantages of thin TiO_2 layers without loosing in light harvesting. By means of different spectroscopic techniques the reversible coordination of the silver ions

to the dye molecule via the thiocyanate ligand could be proven. The silver modification of the dye was found to increase the dye uptake by 38 % and to enhance the overall device efficiency of the SSD to 3.2 % at AM1.5. The beneficial effect of the silver coordination was rationalised in terms of a dye interaction via the silver ions, which assists the dye assembling on the TiO_2 surface and increases the density of the dye monolayer on the surface. The dye modification with silver ions is thus a step towards a tightly packed insulating monolayer of large optical cross section, blocking the dark current. Considerably enhanced open circuit potentials for SSD based on silver modified charged dye complexes, such as N719 indicates furthermore efficient charge screening of electric field emerging from the adsorption of a negative dye such as N719 by the incorporated silver ions. The beneficial influence of the silver co-adsorption on the photovoltaic performance is not limited to the spiro-MeOTAD. A similar improvement of the I_{SC} was also observed using the electrolyte redox mediator cobalt(II)-bis[2,6-bis(1'-butylbenzimidazol-2'-yl)pyridine].

spiro-MeOTAD film

• From a selection of different approaches to minimise interfacial charge recombination in SSD, the blending of the hole conductor matrix with tBP and lithium salt was found to be the most promising strategy, resulting in a drastic enhancement in U_{OC} and an overall device performance of 2.5 %. Different optical and electrochemical techniques, such as electrical impedance and transient laser spectroscopy were employed to study the influence of the two additives on the spiro-MeOTAD in more detail. Contrary to previous experiments on DSSCs the effect of the two additives is not only the result of the flat band potential determining properties of these components. The charge screening effect of lithium ions at the interfaces seems to be more important than the effect of these ions on the band energetics of the TiO_2. In addition to its effect on the recombination, tBP assists the dissolution of the lithium salt in the spiro-MeOTAD and enables higher amounts of lithium to be dissolved. From optical impedance experiments it was inferred that electron collection in the cell is very efficient at low light intensities.

• The low hole mobility in the amorphous state of the spiro-MeOTAD is typically compensated by doping. The doping concentration of the hole conductor, however, was found to be the most important factor for the increase of the recombination kinetics. This implies a trade-off for the SSD: At low doping levels the cell works with a high efficiency at low light intensity, but is non-linear for increasing light intensities. Best device performance is typically obtained for 20 % Sun. For higher doping levels the cell works with a comparable efficiency at all light levels. This efficiency is however rather low compared to the efficiency at low doping level and low light intensity. The maximum efficiency resulting from the combined effect of the doping on charge recombination and charge transport can be shifted

towards higher efficiencies for all light levels using high lithium concentrations and adjusting the layer thickness of the TiO_2 and the HC film.
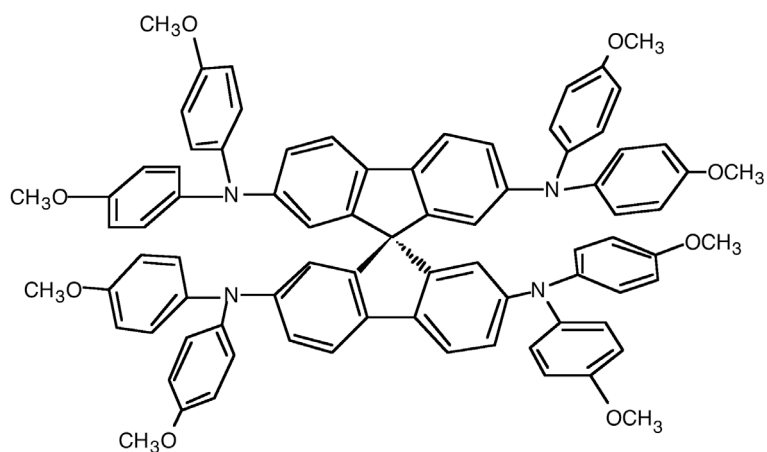
• The irreversible photodoping of the spiro-MeOTAD in presence of lithium ions was identified as an important side reaction, which manifests itself in a significant drop of the IPCE. Application of an UV-filter intercepted the photo doping of the spiro-MeOTAD in solution and rendered also the device more stable against the doping process.

APPENDIX

A.1 Molecular Structures

A.1.1 spiro-MeOTAD

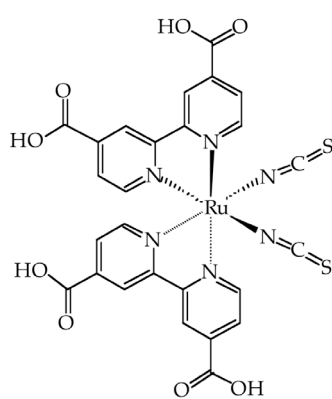2,2',7,7'-tetrakis(N,N-di-p-methoxyphenyl-amine)-9,9'-spirobifluorene
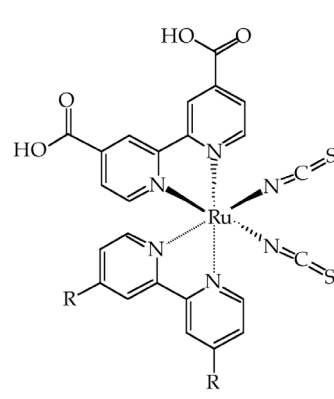
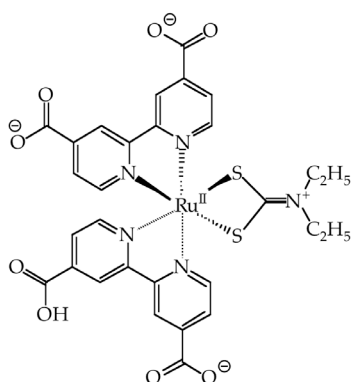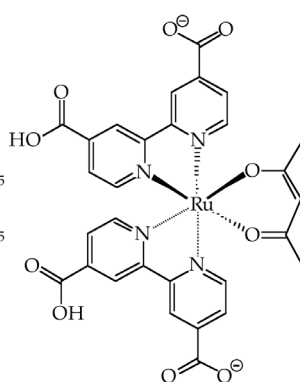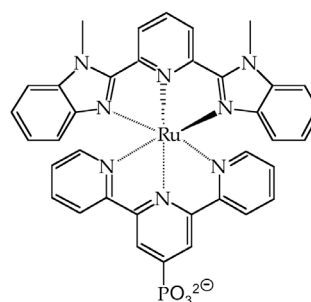***Spectrum of spiro-MeOTAD and its Oxidised Form***
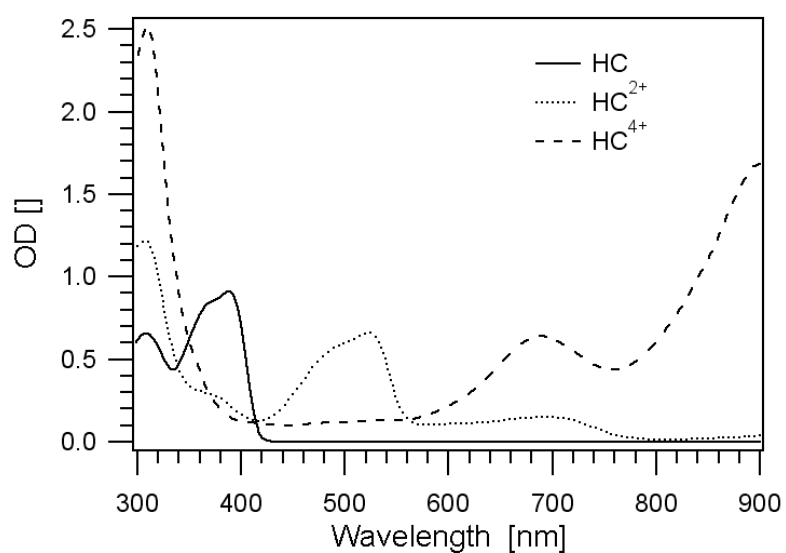
A.1.2   Dye Structures
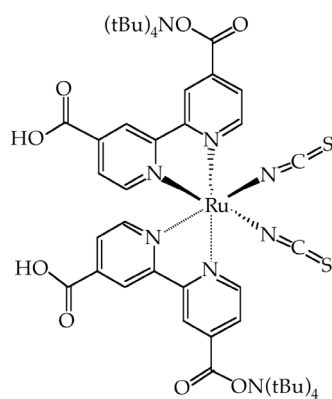
N719   **"Red Dye":N3**   **hydrophobic dye series**

TBA₂[Ru(dcbpyH₂)₂L]   **TBA[Ru(dcbpyH₂)(dcbpyH)L]**   **[Ru(terpyH₂PO₃)(dmpip)]**

"Black Dye": N749

A.1.3

Phthalazine   tBP   Dabco   Piperazine   DBU   Proton sponge
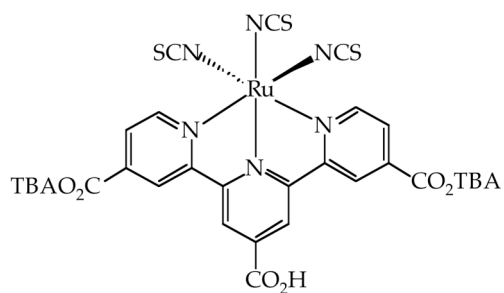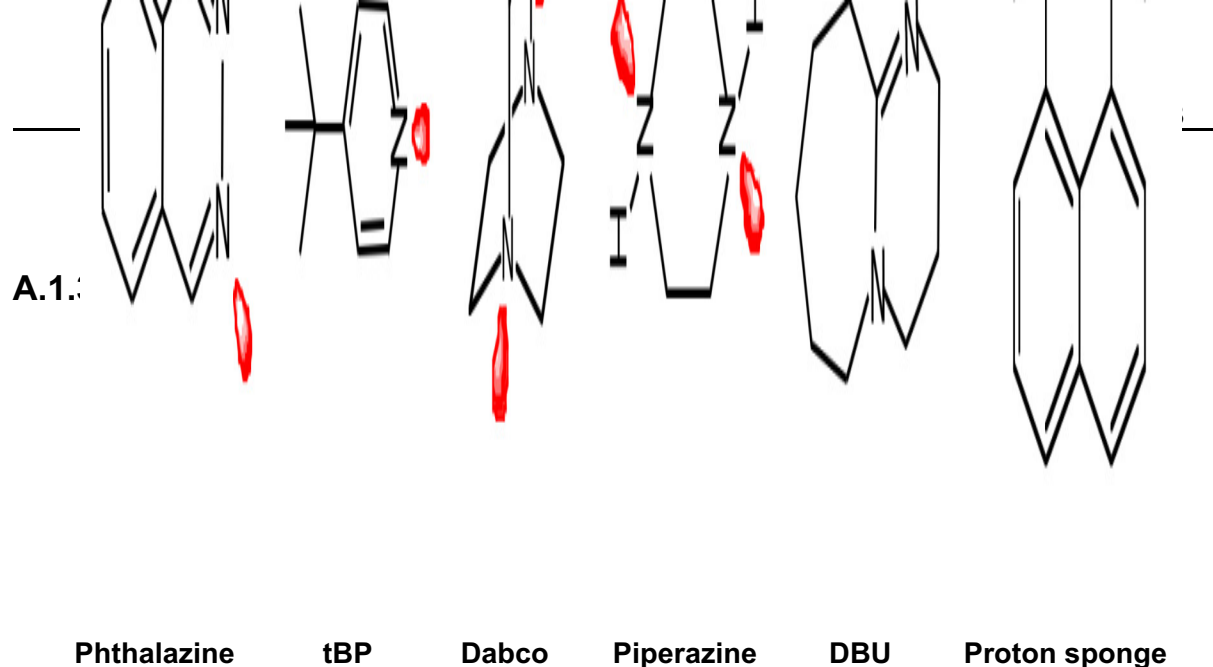
A.1.4   Alternative Redox Mediator for the Verification of the Silver Effect

$Co^{II}(dbbip)_2{}^{2+}$
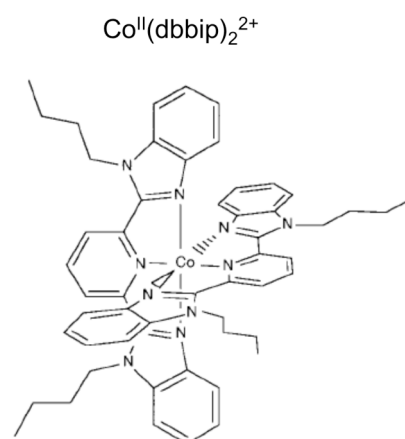
The picture is taken from: H. Nusbaumer, et al. *J. Phys. Chem. B* **2001**, *105*, 10461-10464. The charge-transporting medium consists of the cobalt complex in an electrolyte solution. Correspondingly, solar cells based on this redox mediator are DSSC.

A.2 Calculation of the Mismatch Factor

The spectral mismatch factor for the correction of the white light measurements, as discussed in chapter 2:
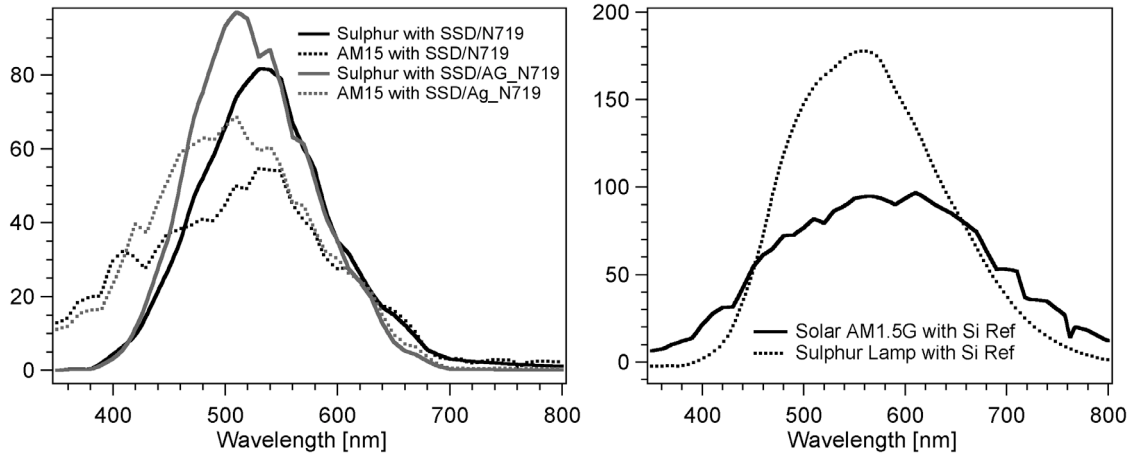
$$M = \frac{M_{RC}}{M_{TC}} = \frac{\int E_{AM1.5}(\lambda) \cdot S^{RC}(\lambda) \cdot d\lambda}{\int E_{sim}(\lambda) \cdot S^{RC}(\lambda) \cdot d\lambda} \cdot \frac{\int E_{sim}(\lambda) \cdot S^{TC}(\lambda) \cdot d\lambda}{\int E_{AM1.5}(\lambda) \cdot S^{TC}(\lambda) \cdot d\lambda}$$

was determined in the wavelength region from 350 to 800 nm for the SSD containing N719 or silver modified N719 based on the following spectral data:
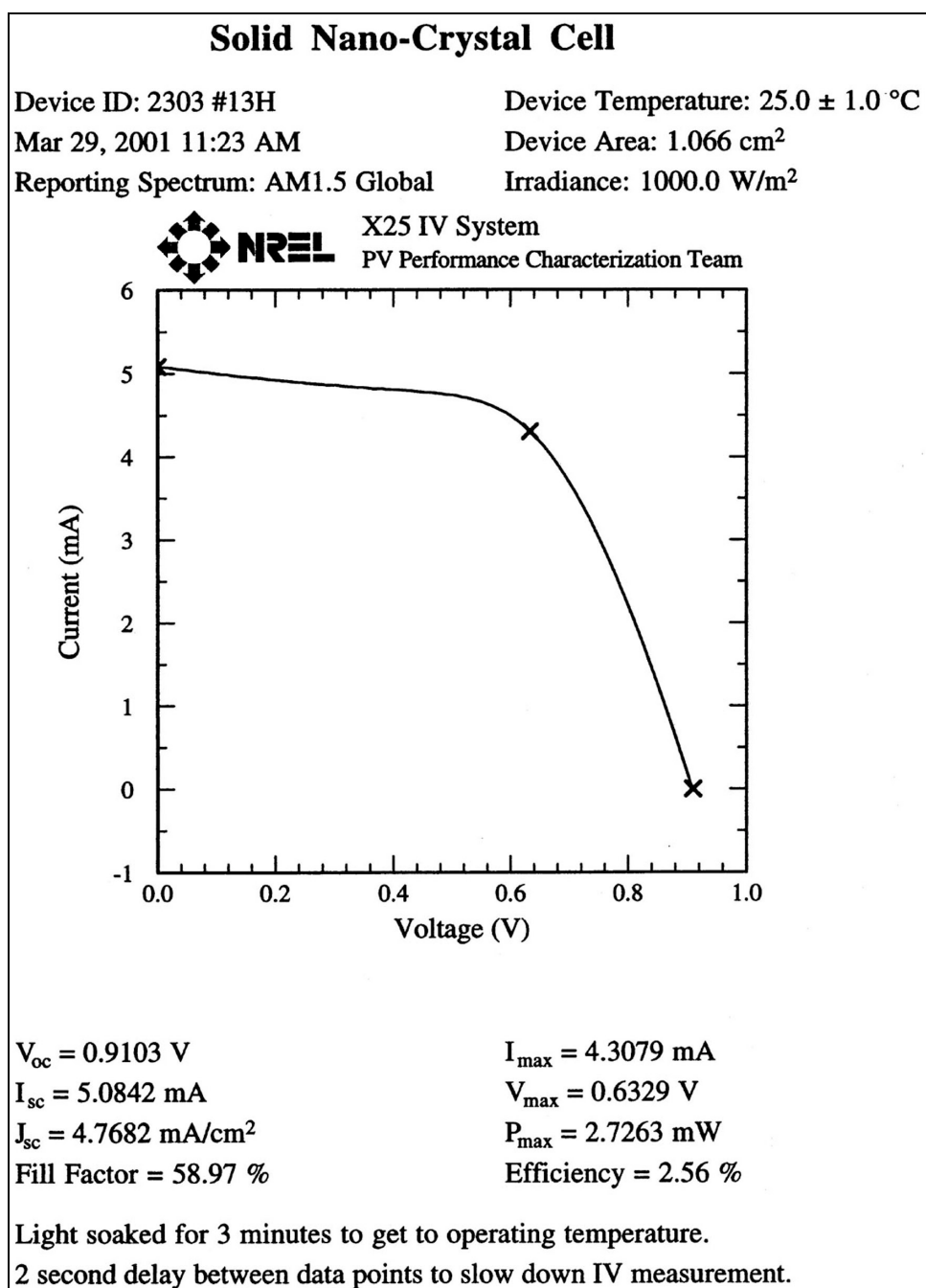
1. Spectral response of the test cell (S^{TC}) and reference cell (S^{RC})
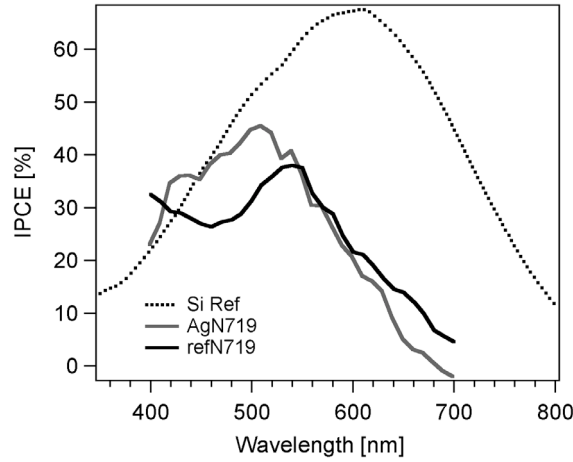
2. The spectral irradiation intensities at AM1.5 ($E_{AM1.5}$) and for the sulphur lamp (E_{sim}) used relative to the test cell respectively relative to the silicon reference cell.

A.3 Device Characterisation at NREL

Solid Nano-Crystal Cell

Device ID: 2303 #13H   Device Temperature: 25.0 ± 1.0 °C
Mar 29, 2001 11:23 AM   Device Area: 1.066 cm^2
Reporting Spectrum: AM1.5 Global   Irradiance: 1000.0 W/m^2

NREL X25 IV System
PV Performance Characterization Team

V_{oc} = 0.9103 V I_{max} = 4.3079 mA
I_{sc} = 5.0842 mA V_{max} = 0.6329 V
J_{sc} = 4.7682 mA/cm^2 P_{max} = 2.7263 mW
Fill Factor = 58.97 %   Efficiency = 2.56 %

Light soaked for 3 minutes to get to operating temperature.
2 second delay between data points to slow down IV measurement.

Original result sheet of current-voltage characteristics for a SSD with an active surface area of 1.07 cm^2, measured at NREL two weeks after device preparation. The hole conductor matrix was 0.26 mM in Li(CF$_3$SO$_2$)$_2$N, 0.18 M in tBP and 0.76 mM in N(p-C$_6$H$_4$Br)$_3$SbCl$_6$. The device was equipped with silver collecting strips to optimise current collection, an anti-reflecting film and a black mask. IPCE has been determined to 40 % in Lausanne.

A.4 IMPS Model[*]

The continuity equation:

$$\frac{\partial n(x,t)}{\partial t} = \eta \cdot \alpha \cdot \exp(-\alpha \cdot x) + D_{eff} \frac{\partial^2 n(x,t)}{\partial x^2} - \frac{n(x,t) - n_0}{\tau_n} \qquad (1)$$

has been solved using the following boundary condition:

$$D \cdot \left.\frac{\delta n(x,t)}{\delta x}\right|_{x=0} = k_{ext} \cdot n(0,t) \qquad (2)$$

where k_{ext} equals the potential-dependent exchange rate constant at the back contact. Taking in account that the gradient of the electron density at the surface is zero:

$$\left.\frac{\delta n(x,t)}{\delta x}\right|_{x=d} = 0 \qquad (3)$$

the following relation has been formulated:

$$\frac{\delta j}{\delta I_0} = C \cdot \left(\frac{A}{N} + \frac{B}{N} - \alpha\right) \qquad (4)$$

with the coefficients:

$$A = \alpha \cdot \exp(-\alpha \cdot d)(k_{ext} + \gamma \cdot D_{eff}) - \gamma \cdot \exp(-\gamma \cdot d)(k_{ext} + \alpha \cdot D_{eff}) \qquad (5)$$

$$B = \alpha \cdot \exp(-\alpha \cdot d)(k_{ext} + \gamma \cdot D_{eff}) + \gamma \cdot \exp(\gamma \cdot d)(k_{ext} + \alpha \cdot D_{eff}) \qquad (6)$$

$$C = \frac{\alpha \cdot I_0}{\gamma^2 - \alpha^2} \qquad (7)$$

$$\gamma = \sqrt{\frac{1}{D_{eff} \cdot \tau} + i \cdot \frac{\omega}{D_{eff}}} \qquad (8)$$

---

[*] L. Dloczik, et al. *J. Phys. Chem. B* **1997**, *101*, 10281-10289.

Name: Jessica Charlotte Krüger
Date of Birth: Mai 15, 1974
Place of Birth: Hamburg, Germany
Nationality: German

UNIVERSITY

2000 - 2003   **EPFL, Laboratory of Photonics and Interfaces**
PhD Thesis: Interface engineering in solid-state dye-sensitized solar cell*s*

1998   **EPFL, Laboratory of Photonics and Interfaces**
Diploma Work: Control of the electronic properties of titanium dioxide by chemical surface modification

1998   Diploma Degree in Chemistry

1995 – 1997   **University of Heidelberg, Germany**
Studies in Chemistry

1993 – 1995   **University Hamburg, Germany**
Undergraduate Studies in Chemistry

INTERNSHIPS & OTHER WORK EXPERIENCE

1999   **EPF Lausanne, Laboratory of Photonics and Interfaces**
Realisation of Kelvin Probe Setup for electronic characterization of semiconductor materials

1995   **University Heidelberg, Germany. Institute of Environmental Chemistry**
Synthesis of chemical standards for the analysis of tin organic and chloro organic compounds

1993   **German Yeast Factory Hamburg, Germany,**
Institute of Analytic and Microbiology
Quality control of different yeast products employing diverse chemical and biological techniques

Assistant Work

1999-2003   Assistant for laboratory courses in physical chemistry (EPFL)
Supervision of master theses

1993 –1995   Assistant for laboratory courses in organic chemistry
(University of Hamburg)

EDUCATION

1993   High School in Hamburg, Germany (Charlotte-Paulsen-Gymnasium)
Abitur, Major in Natural Sciences

PUBLICATIONS

- J. Krüger, R. Plass, P. Cameron, et al. to be published in *J Phys Chem. B*
Charge transport and back reaction in solid-state dye- sensitized solar cells: A study using intensity-modulated photovoltage and photocurrent spectroscopy

- J. Krüger, R. Plass, M. Grätzel, et al. *Appl Phys Lett* **2002**, *81*, 367.
Improvement of the photovoltaic performance of solid-state dye-sensitized device by silver complexation of the sensitizer cis-bis(4,4'-dicarboxy-2,2'bipyridine)-bis(isothiocyanato) ruthenium(II)

- J. Krüger, R. Plass, L. Cevey, et al. *Appl Phys Lett* **2001**, *79*, 2085-2087.
High efficiency solid-state photovoltaic device due to inhibition of interface charge recombination

- F. Lenzmann, J. Krüger, S. Burnside, et al. *J Phys Chem B* **2001**, *105*, 6347-6352.
Surface photovoltage spectroscopy of dye-sensitized solar cells with TiO_2, Nb_2O_5, and $SrTiO_3$ nanocrystalline photoanodes: Indication for electron injection from higher excited dye states

- J. Krüger, U. Bach and M. Grätzel. *Adv Mat* **2000**, *12*, 447-451.
Modification TiO_2 heterojunctions with benzoic acid derivatives in hybrid molecular solid-state devices

CONFERENCES & WORKSHOPS

- TopNano21 3th Annual Meeting, 2002, Bern (Switzerland); poster presentation
Recent Improvements of solid-state dye-sensitized heterojunction solar cells

- SPIE, Organic Photovoltaics III, 2002, Seattle (USA); paper presentation
Recent developments in solid-state dye-sensitized photovoltaic devices based on spiro-MeOTAD

- RSC Conference, Electrochem 02, 2002, Loughborough (UK)

- Material Research Society, Fall Meeting 2001, Boston (USA); paper presentation
Recent developments in sensitized mesoporous heterojunction solar cells.

- EPFL-ETHZ-UCSB-WIS Meeting on Advanced Materials, Crét-Bérard (Switzerland), 2001; poster presentation.
High efficiency solid-state solar cell due to inhibition of interfacial charge recombination.

- 10th International Conference on Unconventional Photoactive Systems (UPS'01), 2001, Les Diablerets (Switzerland); poster presentation
High efficiency solid-state solar cell due to inhibition of interfacial charge recombination.

- EPA, Joint Meeting of the Italian, French, and Swiss Photochemistry Groups, 2001, Lausanne

- Seminar on Thermodynamics in biochemical engineering, November 2000, Monte-Verita (Switzerland).

Dipole Surface Modification of TiO$_2$ in hybrid molecular solid-state devices.

- European Science Foundation, December 1999, Annual Meeting Duisburg (Germany); Posterpresentation

Modification of TiO$_2$ heterojunctions with benzoic acid derivatives in hybrid molecular solid-state devices

ORAL PRESENTATIONS:

- Energy research Centre of the Netherlands (ECN), Petten (Netherlands), 2002

Silver complexation of the sensitizer cis-bis(4,4'-dicarboxy-2,2'bipyridine)-bis(isothiocyanato) ruthenium(II) in solid-state dye-sensitized solar cells.

- University of Bayreuth, Bayreuth (Germany), 2002

Interface charge recombination in solid-state dye-sensitized solar cells based on spiro-MeOTAD.

- University of Bath, Bath (UK), 2001

Frequency resolved characterisation of solid-state dye-sensitized solar cells based on spiro-MeOTAD

- Philips Research Laboratories, Aachen (Germany), 2000

Oxide semiconductor film formation and interface engineering by means of an adsorbed dipole molecule with benzoic acid derivatives.

- Weizmann Institute, Rehovot (Israel), 1999

Modification of TiO$_2$ heterojunctions with benzoic acid derivatives in hybrid molecular solid-state devices

- University of Bochum, Bochum (Germany), 1998

Modification of TiO$_2$ heterojunctions with benzoic acid derivatives in hybrid molecular solid-state devices